Astronomy Reports, Vol. 45, No. 4, 2001, pp. 249–254. Translated from Astronomicheskiĭ Zhurnal, Vol. 78, No. 4, 2001, pp. 291–297.

BL Lac: A New Ultrahigh-Energy Gamma-Ray Source

Yu. I. Neshpor, N. N. Chalenko, A. A. Stepanian, O. R. Kalekin, N. A. Jogolev, V. P. Fomin, and V. G. Shitov

Crimean Astrophysical Observatory, p/o Nauchnyĭ, Crimea

Received May 3, 2000

Abstract—The active galactic nucleus BL Lac was observed with the GT-48 atmospheric Cherenkov detector of the Crimean Astrophysical Observatory from July 23–September 1, 1998, in order to search for ultrahigh-energy gamma-ray (>1 TeV) emission. The object was in the field of view of the detector for more than 24 hours. The source was detected with a high level of confidence (7.2 σ), with a flux equal to $(2.1 \pm 0.4) \times 10^{-11}$ photons cm^{-2} s^{-1}. © *2001 MAIK "Nauka/Interperiodica".*

1. INTRODUCTION

Interest in active galactic nuclei (AGN) among cosmic-ray specialists rose sharply after the Compton Gamma-Ray Observatory (CGRO) demonstrated that a large fraction of sources of high-energy gamma-rays (>100 MeV) were identified with AGN [1]. These galaxies were subsequently observed with ground-based instruments designed to detect gamma-rays with energies of 10^{11}–10^{12} eV. Two AGN were found to be sources of ultrahigh-energy gamma-rays using the 10-m ground Cherenkov detector of the Whipple Observatory in the United States: the Makarian galaxies Mrk 421 and Mrk 501 [2]. At the Crimean Astrophysical Observatory (CrAO), high-energy gamma-rays were also detected from the blazar 3C 66A [3], and classified, like Mrk 421 and Mrk 501, as a BL Lac object; BL Lac is the prototype of this relatively small group of AGN.

One of the main properties of BL Lac objects is variability in their brightness, which can reach 4^m–5^m in the optical (corresponding to luminosity variations by factors of 100). These objects all have appreciable radio emission, which is also, as a rule, variable. BL Lac objects are also characterized by featureless or nearly featureless optical continua, without strong emission lines. The power-law nature of their spectra and the strong polarization of their radiation, which reaches 30–40%, testify that we are observing synchrotron radiation. The characteristic variability timescales—weeks to months—indicate that the dimensions of the radiating volumes in BL Lac objects are typically of the order of 10^{16} cm. The nature of the processes taking place in these galactic nuclei suggest that acceleration of highly energetic particles should occur there, which could be accompanied by the radiation of ultrahigh-energy (UHE; $E > 10^{11}$ eV) gamma-rays. The redshift of BL Lac itself is 0.07, corresponding to a distance of 280 Mpc.

The galaxy BL Lac has been observed using the ground-based UHE gamma-ray detectors of the Whipple Observatory in the 1970s [4] and at the CrAO [5]. Stepanian *et al.* [5] obtained an upper limit for the flux $F < 1.1 \times 10^{-10}$ photons cm^{-2} s^{-1} for an energy threshold 2.2×10^{12} eV. The 1971 observations of the American group [4] yielded an upper limit of $F < 1.2 \times 10^{-10}$ photons cm^{-2} s^{-1} for energies $E > 2.5 \times 10^{11}$ eV. BL Lac was again observed by the Whipple Observatory in October–November 1994, for a total time of 162 min. These observations yielded an upper limit on the flux of 1.4×10^{-11} photons cm^{-2} s^{-1} [6].

During this time, BL Lac was observed by the CGRO. Observations before January 1995 indicated a flux of 1.4×10^{-7} photons cm^{-2} s^{-1} [7], corresponding to a 2.4 σ detection. However, in January–February 1995, the flux rose to $(4.0 \pm 1.2) \times 10^{-7}$ photons cm^{-2} s^{-1}, providing evidence for variability in the gamma-ray emission from BL Lac. Studies of BL Lac at the CrAO were renewed in 1998 using the second-generation GT-48 gamma-ray telescope [3, 8].

2. BRIEF DESCRIPTION OF THE GT-48 GAMMA-RAY TELESCOPE

Gamma rays with ultrahigh energies (~10^{11} eV) cannot reach the surface of the Earth. They interact with the nuclei of atoms in the atmosphere, forming so-called broad air showers (BASs) consisting of high-energy electrons and positrons. The charged particles of BASs emit Cherenkov radiation at optical wavelengths at small angles (0.5°–1°) to the direction of motion of the original gamma ray, making it possible to not only detect the presence of the gamma ray but also determine the direction toward its source. However, charged cosmic-ray particles also give rise to Cherenkov flares in the Earth's atmosphere. These are very similar to flares due to gamma-ray sources, leading to the main difficulty in detecting and studying these sources. Nevertheless, differences between these two types of flares do exist, and multielement light-collecting chambers that reconstruct images of Cherenkov

1063-7729/01/4504-0249$21.00

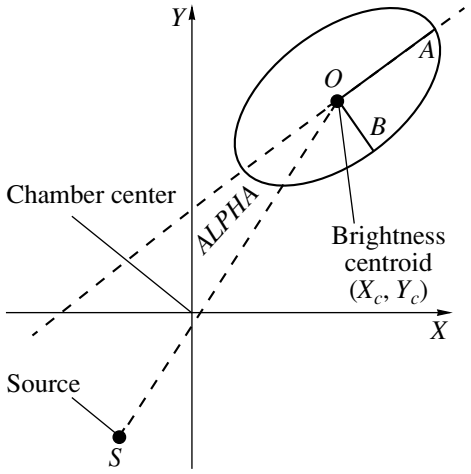

Fig. 1. Graphical depiction of flare parameters. The segment *OS* corresponds to the parameter *DIST*.

flares can be used to eliminate the overwhelming majority of events resulting from charged cosmic-ray particles.

The GT-48 telescope equipped with multichannel imaging chambers began to operate at the CrAO in 1989. The instrument consists of two altitude–azimuth mounts (sections)—northern and southern—separated by 20 m and located at a height of 600 m above sea level. Six parallel telescopes are mounted on each section. The optics for each telescope include four 1.2-m mirrors with a common focus. The mirrors of the four telescopes have a focal length of 5 m. Chambers with 37 photomultipliers are placed at each focus. These are used to reconstruct the images of Cherenkov flares at visible wavelengths (300–600 nm). There is a conical light guide at the entrance to each photomultiplier. The mean diameter of the light guide entry window is 0.4°. The field of view of the entire light-collecting apparatus is 2.6°. The signals from the cells of the four light receivers are linearly summed, and arrive at a amplitude-code converter via the 37 channels. In this way, a discrete image of the Cherenkov flare is obtained, which can be stored on a computer. Flares are recorded only if the amplitudes of signals coincident in time exceed a specified threshold in any two of the 37 cells. The time resolution for evaluating coincidence is 15 ns.

Two other telescopes with a focal length of 3.2 m are intended for observations at ultraviolet wavelengths, from 200 to 300 nm. Although the fluxes from BASs are weak in this part of the spectrum, detecting this radiation can aid in distinguishing showers due to cosmic gamma-ray sources against the background of showers due to charged cosmic-ray particles. In this sense, the GT-48 telescope is unique. We will discuss the use of ultraviolet emission to distinguish showers due to gamma-ray sources in more detail below. The total area of both mirrors is 54 m^2. The effective detection threshold energy of gamma rays is 1.0 TeV. More detailed descriptions of the GT-48 telescope can be found, for example, in [3, 8].

3. OBSERVATIONS AND DATA ANALYSIS

Observations of the object BL Lac ($\alpha = 22^h02^m43^s$, $\delta = 42°16'40''$) were carried out in July–August 1998 using the two parallel sections in a coincidence regime with a time resolution of 100 ns; i.e., we recorded only events that were observed simultaneously on both sections to within this time resolution. Each section tracked the source and also made observations of the background, with the time between these observations equal to 40 min. The background recordings were performed at the same azimuths and zenith angles as those for the source, and preceded the source observations. In all, there were 63 sessions, with the duration of the source observations in each being 35 min. The zenith angle did not exceed 30°. We did not include sessions carried out under poor weather conditions in the reduction. As criteria for the selection of sessions, we used the dispersion of the count rate per minute during the session and the mean count rate. We excluded sessions in which the dispersion of the count rate differed from the theoretical value by more than two σ or the count rate was lower than half the maximum value for a given zenith angle. After this selection, 42 sessions remained, corresponding to 24 hours and 30 minutes of observations of BL Lac. Further, we excluded events for which a maximum of the amplitude-code transformation was reached in at least one of the channels, and also events for which the maximum amplitude was detected in one of the outer channels of the light receiver. After this preliminary selection, 30340 source events and 29489 background events remained for further analysis. The difference in the numbers of flares recorded for source and background observations is $N_\gamma = 851 \pm 245$, where 245 is the statistical error $\sigma = \sqrt{N_s + N_b}$, and N_γ is the number of Cherenkov flares from gamma rays.

The resulting data were subject to further reduction, to analyze the digitized flare images using formal mathematical methods. We computed the first and second moments of the brightness distributions, from which we derived the parameters of the Cherenkov flares: the coordinates of the center of the brightness distribution X_c and Y_c, the effective length A, the effective width B, and angle φ characterizing the direction of maximum extension of the flare image, i.e., its orientation (Fig. 1). These moments were computed for cells with signals greater than some threshold value [9]. The parameters of a flare (event) recorded simultaneously on each section were determined independently using the data acquired for each section, so that each event has two values for each parameter, which we denote "1" and "2" for the northern and southern sections, respectively.

It is known that electrons from proton and nuclear showers (*p* showers, BASs) of a given energy, on average, penetrate to appreciably larger depths in the Earth's atmosphere than do electrons from gamma-ray showers of the same energy. This means that Cherenkov flares from *p* showers contain a relatively larger fraction of ultraviolet

Table 1. Number of recorded and selected events

Selection method	Number of events in the source direction	Number of events in the background direction	Difference	Signal-to-noise, standard deviations
Without selection	30340	29489	851	3.5
Selection in coordinate-independent parameters	1166	881	285	6.3
Selection in coordinate-dependent parameters	259	119	140	7.2

radiation compared to flares formed by gamma rays. As a parameter characterizing the relative content of ultraviolet radiation, we use the logarithm of the ratio of the flare amplitude in the ultraviolet and the total flare amplitude in the visible: UV.

Flares from charged particles have larger angular sizes. In addition, they are distributed isotropically, while images of flares formed by gamma rays are extended in the direction toward the source. The angle between the direction toward the source from the flare center and the major axis of the image ellipse—the parameter *ALPHA*—can also be used to distinguish gamma-ray events. Using these differences between images of Cherenkov flares associated with cosmic-ray particles and gamma rays, it is possible to eliminate 99% of background events while leaving an appreciable fraction of gamma-ray events.

Events whose parameter values did not fall in a specified range were excluded from consideration. We selected those parameter values for which the effect in terms of standard deviations—that is, $N_s - N_b/\sqrt{N_s + N_b}$ (the signal-to-noise ratio)—was maximum. Here, N_s and N_b are the number of selected events for the source and the background, respectively. In the selection, first and foremost, we considered the total amplitude of flare *V*. Flares with small amplitudes were excluded from further consideration, since their parameters had large errors. It is also known that images of flares associated with proton showers have complex shapes, and can have several maxima or be fragmented, while flares from gamma-ray showers are compact. The parameter used to characterize the shapes of the flares is denoted IPR, and it is assigned the value 0 for compact images. We used the effective length *A* and width *B* of the flare images as parameters to distinguish gamma-ray showers against the background of charged-particle showers.

In this way, we excluded events from further consideration if at least one of the following conditions was satisfied: $V(1) < 100$, $V(2) < 100$, $\mathrm{IPR}(1) \neq 0$, $\mathrm{IPR}(2) \neq 0$, $A(1) > 0.^\circ 30$, $A(2) > 0.^\circ 30$; $B(1) > 0.^\circ 175$, $B(2) > 0.^\circ 175$, $\mathrm{UV}(1) > 1.1$, $\mathrm{UV}(2) > 0.8$. The parameters *V*, IPR, *A*, *B*, and UV do not depend on the position of the source relative to the flare; i.e., they are coordinate-independent. The application of these parameters made it possible to increase the signal-to-noise ratio to 6.3 σ. Our results are presented in Table 1.

It is possible to refine or even accurately determine the direction of a gamma-ray source using coordinate-dependent parameters, such as *ALPHA*—the orientation of the flare image relative to the direction of a proposed (trial) gamma-ray source—and *DIST*, which is numerically equal to the angular distance between the center of the flare brightness distribution and the direction toward the trial source (see Fig. 1). In this case, among Cherenkov flares selected based on coordinate-independent parameters, we identified gamma-ray-like events for which $ALPHA(1) < 30^\circ$, $ALPHA(2) < 30^\circ$, $0.^\circ 25 < DIST(1) < 0.^\circ 95$, and $0.^\circ 25 < DIST(2) < 0.^\circ 95$. The last column of Table 1 presents the results of this selection (selection based on coordinate-dependent parameters).

4. RESULTS

Thus, as a result of the selection procedure described above, we have been able to separate out reliable detections of gamma-ray fluxes. The count rate for the recorded gamma rays was 0.095 ± 0.013 photons/min. In order to determine the corresponding flux, we must take into account the effective area of the detector and determine what fraction of the gamma rays remained after the selection procedure. This can be done via theoretical Monte-Carlo studies of the gamma-ray showers. This method was used to numerically model the development of broad atmospheric showers and their detection by the GT-48 telescope [10].

This task was carried out in two stages. We first obtained all of the parameters needed to model the detection of gamma rays by the GT-48 telescope by comparing the results of our simulations of the recording of the cosmic-ray background with the observational data. Further, we simulated the recording of gamma rays and computed the corresponding fluxes. The simulations were carried out using code written by A.V. Plyasheshnikov (see [11]). Given a type of initial particle and the angle for its entry into the atmosphere, the code computes the number of Cherenkov photons from a BAS at the height of the detector.

To model recording of the background, we used the results of computations of showers due to protons and helium nuclei. These form the vast majority of cosmic rays at ultrahigh energies. The differential energy spectral indices for protons and helium are 2.75 and 2.62, respectively [12]. In all, we modeled 133 610 proton and

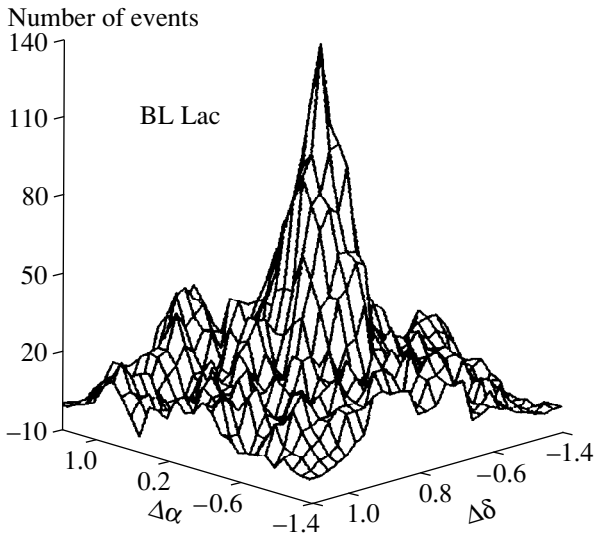

Fig. 2. Stereoimage of a "map" of the distribution of arrival directions of gamma rays. The center of the "map" coincides with the coordinates of BL Lac; Δδ is the deviation from the source in declination and Δα the deviation in right ascension (in degrees).

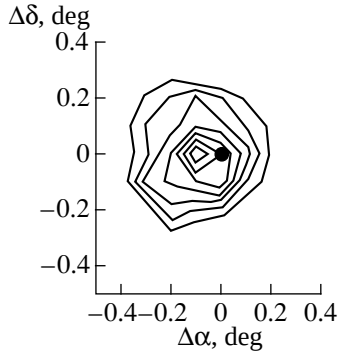

Fig. 3. Isophotes of the distribution of gamma-ray arrival directions. The notation is the same as in Fig. 2. The isophote step is ten events. The first value is 70 events. The black circle at the center shows the optical position of BL Lac.

56 670 helium events at energies from 0.4–70 TeV. The energy distribution of the events was chosen to minimize the statistical error in all energy ranges. Therefore, for each event, we computed a weight taking into account the differential flux and spectral index [12]. Further, we modeled the recording of background events by the gamma-ray telescope. The radio-technological threshold in the model was chosen to provide a count rate for background events equal to 72 min^{-1}; i.e., the value obtained in the observations.

The last required model parameter is the coefficient for the conversion of photo-electrons into a discrete digital shape. We derived this coefficient by requiring that the number of events for which at least one of the channels was saturated (a maximum in the analog-code transformation) be ~10% of the number of recorded events. This ratio was likewise obtained from the observational data. Thus, using model parameters derived by comparing modeling results with observations of background cosmic rays, we were able to model the process of recording gamma-ray events. In all, we modeled 5519 gamma events at energies 0.4–20 TeV with a differential energy spectral index of 2.4. The effective energy threshold for recording the gamma rays was 1.0 TeV. All events were parametrized in the same way as the observations. We selected model gamma events using the same criteria as in our analysis of the data for BL Lac. After this selection, 21.6% of the gamma events remained. This indicates that, since the count rate for the selected observed gamma events was 0.095 min^{-1}, the initial rate should be 0.44 min^{-1}. This count rate corresponds to a flux of gamma rays with energies >1.0 TeV equal to $(2.1 \pm 0.4) \times 10^{-11}$ photons $cm^{-2}\ s^{-1}$.

We applied a trial-source method to determine the direction of the gamma-ray flux [13–15]. This method is based on the fact that the images of Cherenkov flares from gamma rays are oriented toward the source in the focal plane of the telescope, while the major axes of the image ellipses for *p* showers are, to first approximation, oriented uniformly in all directions. Therefore, if we select flares, adopting as the direction toward the source an arbitrary point in the focal plane with coordinates (X_iY_j), and then make a selection according to coordinate-dependent parameters, the number of selected *p* showers will not depend on the position of the trial source, while the number of selected gamma events will have a maximum when the trial source coincides with the actual source. If we now subtract from the number of flares obtained toward a trial source the number of background flares obtained for those same coordinates, we obtain the distribution of gamma rays over the field of view of the light receiver as a function of the position of the trial source $N(X_iY_j)$; i.e., a "map" (two-dimensional histogram) of gamma-like events N_γ. In this way, we can find the position of the true source of gamma rays. Figure 2 presents a two-dimensional histogram obtained using the coordinate-dependent criteria *ALPHA* and *DIST*.

Figure 3 shows isophotes of N_γ. The first isophote corresponds to 50% of the maximum value of N_γ, which is equal to (140 ± 19.4) events (7.2 σ) and corresponds to the point with coordinates $X = -0.1$, $Y = 0.0$. During the observations, the center of the chambers were pointed at BL Lac. It is clear from Fig. 3 that the coordinates of the UHE gamma-ray source coincide well with the optical coordinates for BL Lac.

5. TEMPORAL VARIATIONS

Optical observations of BL Lac have been conducted for many years. BL Lac was first discovered as a stellar object in 1929. Observations over long timescales demonstrated that variations in its brightness

Table 2. Powers of several BL Lac objects

Object	Distance, Mpc	log$L$, [erg/s]/reference		
		optical	high energy	ultrahigh energy
BL Lac (1998)	280	44.8 [17]	(1995) 44.9 [20]	44.5 [this paper]
Mrk 501	160	44.4 [19]	–	44.5 [22]
3C 66A	1800	46.4 [19]	46.2 [20]	46.3 [23]
Crab	0.002	36.5 [24]	35.3 [20]	34.0 [21]

reach 5^m (corresponding to luminosity variations of a factor of 100) [16]. Quasi-periodic fluctuations with periods of 0.8 and 0.6 yrs have been detected, as well as more rapid brightness variations.

During the period for our observations (July–August 1998), the visual brightness of BL Lac varied from 14.6^m to 13.5^m [17]. Rapid variations with amplitude 0.5^m were noted. Unfortunately, the detailed temporal variations in the visual luminosity of BL Lac presented in [17] do not coincide in time with our observations.

Figure 4 presents the mean gamma-ray count rate per minute over an observing night. We conclude from this figure that the UHE gamma-ray flux is time variable. During the optical observations (July–August 1998), the total optical energy flux varied from 3.8×10^{44} to 1.0×10^{45} erg/s. During this time, the mean total energy flux in UHE gamma rays was 3.2×10^{44} erg/s.

It is interesting to compare the power emitted by BL Lac objects in various energy ranges. We composed Table 2 from data available in the literature, assuming that the radiation at all energies is isotropic. For comparison, we also present in Table 2 the power of the Crab Nebula. We can see that, for the gamma-ray source BL Lac, as well as the objects Mrk 501 and 3C 66A, the total powers in the optical, at high energies, and at ultrahigh energies are quite comparable. Unfortunately, EGRET did not conduct any observations of BL Lac during the period under consideration, and we therefore present measurements for 1995 in the table. Note that the flux of gamma rays with energies >100 MeV greatly increased during the optical flare of July 19, 1997 [18]. At maximum light, the brightness of BL Lac reached almost 12^m (a luminosity of $5 \cdot 10^{45}$ erg s^{-1}), while the gamma-ray flux at energies >100 MeV reached $5 \cdot 10^{-6}$ phot. cm^{-2} s^{-1} ($5 \cdot 10^{46}$ erg s^{-1}). The energy spectrum of the photons in July 1997 was appreciably harder than in more quiescent periods: the spectral index was 1.7 ± 0.1, as opposed to 2.3 ± 0.3. If we suppose that the spectral slope during the July 1997 flare was preserved to 10^{12} eV, the power in UHE gamma rays should have been no lower than 5×10^{46} erg/s, and should have exceeded the power in the optical (Table 2) by a order of magnitude.

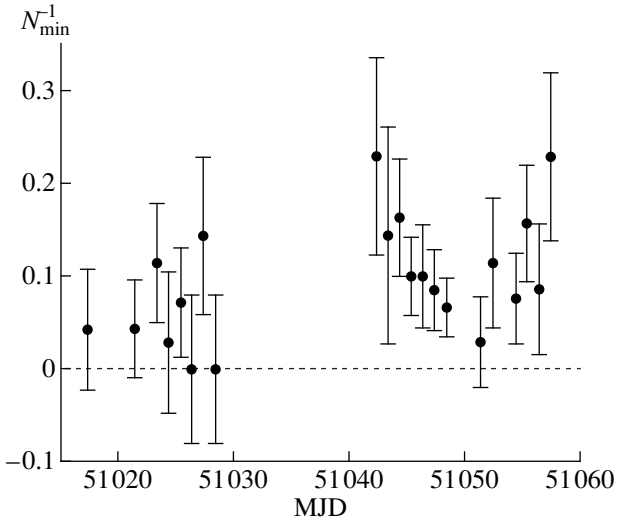

Fig. 4. Time behavior of the gamma-ray flux (mean for an observing night). The errors shown are statistical.

6. CONCLUSION

Thus, we conclude that BL Lac is a source of UHE gamma rays. It is likely that the flux of ultrahigh-energy gamma rays is variable. We expect that this flux rises sharply in periods of enhanced optical brightness. The spectra of BL Lac, Mrk 501, and 3C 66A are similar. It would be very desirable to observe BL Lac simultaneously in a number of different wavebands across the electromagnetic spectrum: from radio to UHE gamma energies.

ACKNOWLEDGMENTS

The authors thank S.G. Kochetkov and Z.N. Skiruta for help in reducing the data and preparing the article.

REFERENCES

1. D. J. Thompson, D. L. Bertsch, B. L. Dingus, *et al.*, Astrophys. J., Suppl. Ser. **101**, 259 (1995).
2. J. Quinn, C. W. Akerlof, S. Biller, *et al.*, Astrophys. J. Lett. **456**, L83 (1996).
3. Yu. I. Neshpor, A. A. Stepanyan, O. R. Kalekin, *et al.*, Pis'ma Astron. Zh. **24**, 167 (1998) [Astron. Lett. **24**, 134 (1998)].

4. G. G. Fazio, H. F. Helmken, E. O. O'Mongain, and T. C. Weekes, Astrophys. J. Lett. **175**, L117 (1972).
5. A. A. Stepanyan, B. M. Vladimirskiĭ, Yu. I. Neshpor, and V. P. Fomin, Izv. Krym. Astrofiz. Obs. **53**, 29 (1975).
6. J. Quinn, C. W. Akerlof, S. Biller, *et al.*, in *Proceedings of the 24th International Conference on Cosmic Rays, Roma, 1998*, Vol. 2, p. 366.
7. M. Catanese, C. W. Akerlof, S. D. Biller, *et al.*, Astrophys. J. **480**, 562 (1997).
8. B. M. Vladimirskiĭ, Yu. L. Zyskin, A. P. Kornienko, *et al.*, Izv. Krym. Astrofiz. Obs. **91**, 74 (1995).
9. A. P. Kornienko, A. A. Stepanian, and Yu. L. Zyskin, Astropart. Phys. **1**, 245 (1993).
10. O. R. Kalekin, Izv. Krym. Astrofiz. Obs. **95**, 167 (1999).
11. A. K. Konopelko and A. V. Plyasheshnikov, Nucl. Instrum. Methods Phys. Res. (2000).
12. B. Wiebel, Fachbereich Physik Bergische Universitet, April 1994, WUB 94-08.
13. C. W. Akerlof, M. F. Cawley, M. Chantell, *et al.*, Astrophys. J. Lett. **377**, L97 (1991).
14. Yu. J. Neshpor, A. P. Kornienko, A. A. Stepanian, and Yu. L. Zyskin, Exp. Astron. **5**, 405 (1994).
15. V. P. Fomin, S. Fennell, R. C. Lamb, *et al.*, Astropart. Phys. **2**, 151 (1994).
16. J. H. Fan, G. Z. Xie, E. Pecontal, *et al.*, Astrophys. J. **507**, 173 (1998).
17. M. G. Nikolashvili, O. M. Kurtanidze, and G. M. Richter, in *Proceedings of the OJ-94 Annual Meeting 1999, Torino, 1999*, Ed. by C. M. Raiteri, M. Villata, and L. O. Takalo, p. 33.
18. S. D. Bloom, D. L. Bertsch, R. C. Hartman, *et al.*, Astrophys. J. Lett. **490**, L145 (1997).
19. E. S. Perlman, J. T. Stocke, J. F. Schachter, *et al.*, Astrophys. J., Suppl. Ser. **104**, 251 (1996).
20. R. C. Hartman, D. L. Bertsch, S. D. Bloom, *et al.*, Astrophys. J., Suppl. Ser. **123**, 79 (1999).
21. O. R. Kalekin, Yu. I. Neshpor, A. A. Stepanyan, *et al.*, Pis'ma Astron. Zh. **21** (3), 184 (1995) [Astron. Lett. **21**, 163 (1995)].
22. N. A. Andreeva, Yu. L. Zyskin, O. R. Kalekin, *et al.*, Pis'ma Astron. Zh. **26** (3), 243 (2000) [Astron. Lett. **26**, 199 (2000)].
23. Yu. I. Neshpor, A. A. Stepanyan, O. R. Kalekin, *et al.*, Astron. Zh. **77**, 723 (2000) [Astron. Rep. **44**, 641 (2000)].
24. *Physics of Space* [in Russian], Ed. by R. A. Sunyaev (Moscow, 1986), p. 327.

Translated by D. Gabuzda

Astronomy Reports, Vol. 45, No. 4, 2001, pp. 255–268. Translated from Astronomicheskiĭ Zhurnal, Vol. 78, No. 4, 2001, pp. 298–312.

Light-Curve Synthesis for Close Binaries: An Extended Shock as an Analog of a Hot Spot in Cataclysmic Variables

T. S. Khruzina

Sternberg Astronomical Institute, Universitetskiĭ pr. 13, Moscow, 119899 Russia

Received May 3, 1999

Abstract—An algorithm is presented for the synthesis of the light curve of a close binary system consisting of a red dwarf that fills its Roche lobe and a spherical white dwarf. The spherical component is surrounded by an elliptical, geometrically thick accretion disk. The code models an extended shock located along the edge of the stream near the outer boundary of the disk. The observational manifestations of the shock show that it can be considered as an analog of a hot spot at the edge of the disk. Synthetic light curves for the SU UMa system OY Car at various phases of its activity indicate that the model can describe both typical and peculiar light curves for this cataclysmic variable reasonably well. *© 2001 MAIK "Nauka/Interperiodica".*

1. INTRODUCTION

Studies of the light curves of close binary systems (CBSs) at late stages of their evolution provide rich information about the structure of gas streams, flows, disks, and other formations associated with the flow of matter onto the relativistic object. Simple intuitive concepts about the matter-flow pattern in CBSs are often unable to fully explain the observed light curves, which sometimes display very complicated shapes. This is true both of cataclysmic binary systems (eruptive variables), with a red dwarf that fills its Roche lobe and overflows onto its companion through the inner Lagrangian point, and of white dwarfs surrounded by optically bright and geometrically thick accretion disks. The orbital light curves of cataclysmic variables often display "humps"—recurrent increases of the brightness by up to $\sim 1^m$, usually at orbital phases ~0.7–0.9 (phase 0.0 corresponds to upper conjunction of the white dwarf). In addition to such humps in their light curves, some eclipsing cataclysmic variables (Z Cha, OY Car, V2051 Oph, HT Cas, IP Peg) display eclipses of the central white dwarf by the red star's body and of a hot area adjacent to the disk. A detailed description of cataclysmic variables and their basic parameters can be found, for example, in [1].

To describe various features of their light curves, the widely accepted classical model of cataclysmic variables hypothesizes the presence of a "hot spot," formed as a result of shock interaction of the gas stream with matter at the outer boundary of the accretion disk. This model provides an adequate qualitative description of the typical light curves of eruptive variables in their inactive phase, in particular for small orbital inclinations, and yields reasonable values for model parameters, including those for the hot spot (size, luminosity, position angle). However, as we accumulate observational data for more and more cataclysmic variables, difficulties emerge when synthesizing their light curves in the framework of the classical model.

For example, light curves for several variables occasionally show a second hump in addition to their regular maxima (OY Car). Other stars (RX Tri, UX UMa) display an eclipse on the ascending rather than the descending (as is required in the classical model) branch of the hump. As a consequence, the hot spot must be located at position angles that contradict physical laws, since the position of the spot is determined by the deflection (due to the Coriolis force) of the gas stream from the line connecting the component centers. For the same reasons, the position of the hump in the light curve should be constant, while in reality it is time-dependent in some systems.

Numerical simulations of the flow of matter in semi-detached CBSs without magnetic fields have indicated [2–5] that, in a steady-state flow regime, the presence of an inter-component envelope results in the absence of a shock interaction between the stream flowing from the inner Lagrangian point L_1 and the gas of the forming disk. The jet is deflected under the action of the gas from the inter-component envelope, approaches the disk tangentially, and does not give rise to any shock perturbation (hot spot) at the edge of the disk. Even if a newly formed stream collides with a previously formed disk at the initial time, the gas-flow morphology will be rearranged after several orbital periods, so that the interaction between the stream and disk will become shockless. At the same time, an extended shock wave, whose observational manifestations are equivalent to those of a hot spot on the disk, will be formed along the edge of the stream. This concept was favored in 1999 by Matsuda *et al.* [6, 7], who introduced the term "hot line" to contrast with "hot spot."

Over the last decade, we have developed more and more detailed methods to synthesize model light curves

1063-7729/01/4504-0255$21.00

for both massive and low-mass X-ray binary systems [8, 9], as well as for cataclysmic variables [10, 11]. In [10], we considered light-curve synthesis for cataclysmic variables in a classical model with a hot spot at the lateral surface of a circular disk and in a model with a bulge (prominence) at the edge of the disk. The bulge was treated as a region of energy release shaped like an outgrowth on the lateral part of the disk, oriented along the radius vector from the center of the circular disk to its edge. For several cataclysmic variables [5], even this rough model made it possible to substantially improve upon the description of the light curves provided by the classical model—in particular, for variables with anomalous light curves and those with "double eclipses" (systems with orbital inclination 80°–90°). For such systems, the presence of a radiating structure beyond the accretion disk appreciably distorts the light curve, so that it cannot be described adequately by classical hot-spot models. The bulge model was also able to describe well the observed light curves for SS Cyg—a well known system without eclipses of the white dwarf [12].

Here, we synthesize the light curves of CBSs taking into account the presence of a shock wave along the gas stream extended in the direction of the inner Lagrangian point. The model was made to resemble as much as possible the gas-dynamical pattern for matter flows in close binary systems described in [2–5]. In Sections 2–4, we describe the CBS model used for the light-curve synthesis and techniques for calculating the radiation flux from the shock area and the mutual eclipsing of the system components. We consider the influence of the hot line in the system on the light curve in Section 5. Section 6 presents the results of applying our synthesis code to derive parameters for the cataclysmic variable OY Car via analyzing light curves obtained both during a super-flare and in quiescence.

2. THE MODEL OF THE SYSTEM

We will use the standard model to describe the shape of the stellar surfaces in a close binary system. We assume a CBS consists of a star of late spectral type (secondary) that fills its Roche lobe and a spherical star of modest size (for example, a white dwarf with radius R_w) surrounded by a geometrically thick, elliptical accretion disk [11]. The spherical star is traditionally considered the primary, and is located at one focus of the elliptical disk. The disk is represented by the figure that results when an ellipsoid with semi-axes a, b, and c intersects two paraboloids determined by the parameter A_p. This parameter depends on the angle ψ of rotation of the radius vector R_ψ about an axis perpendicular to the orbital plane. The ellipsoid determines the shape of the disk on its outer (lateral) surface. The paraboloids determine the shape of the inner (upper and lower) surfaces of the elliptical accretion disk. All lengths are given in units of the component separation a_0; in this case, $a_0 = 1$.

Under certain conditions, mass transfer from the secondary to the primary can result in periodic variations of the elliptical disk's orientation relative to the line connecting the centers of mass of the components (the horizontal axis of the system). We will describe the disk orientation using the angle α_e between the radius vector connecting the center of the white dwarf and the disk periastron P, and the horizontal axis of the system [11]. In a non-steady-state regime, α_e can vary from 0 to 2π. Conventionally, we will take the angle α_e to increase in the direction of orbital motion of the components.

In the steady-state regime, the interaction between the stream and inter-component envelope forms an extended shock wave along the edge of the stream [2–4]. We will assume that the shock can radiate energy at the surface of the stream, both from the side of the inflowing matter and from the opposite side, depending on the physical parameters of the interacting flows (velocity, density, etc.). To model the shape of this optically thick region of energy release (the hot line), we assume that it can be represented as a part of an ellipsoid extended toward the inner Lagrangian point L_1. The ellipsoid center is located at point $\hat{O}$, which is in the orbital plane, inside the elliptical disk at some distance from its edge. For definiteness, we will call this ellipsoid the "spindle," to distinguish it from the ellipsoid describing the lateral surface of the disk. To construct the figures of the spindle, disk, and CBS components, we introduce the following coordinate frames (Fig. 1).

(1) $\hat{O}\hat{X}\hat{Y}\hat{Z}$, fixed to the center of the spindle. The point $\hat{O}$ is the spindle center. The axes $\hat{O}\hat{X}$ and $\hat{O}\hat{Y}$ lie in the orbital plane, with $\hat{O}\hat{Y}$ directed toward the inner Lagrangian point, $\hat{O}\hat{X}$ perpendicular to it, and motion from $\hat{O}\hat{Y}$ to $\hat{O}\hat{X}$ being counterclockwise. The $\hat{O}\hat{Z}$ axis is perpendicular to the orbital plane.

(2) $\overline{O}\overline{X}\overline{Y}\overline{Z}$, fixed to the paraboloidal part of the disk. Point $\overline{O}$ coincides with the center of mass of the spherical star. The $\overline{O}\overline{X}$ and $\overline{O}\overline{Y}$ axes lie in the orbital plane, with $\overline{O}\overline{X}$ passing through the disk periastron P and making an angle α_e with the horizontal axis of the binary system $O\overline{O}$. The $\overline{O}\overline{Y}$ axis is perpendicular to $O\overline{O}$, and the direction of motion from $\overline{O}\overline{Y}$ to $\overline{O}\overline{X}$ is counterclockwise. The $\overline{O}\overline{Z}$ axis is perpendicular to the orbital plane.

(3) $\tilde{O}\tilde{X}\tilde{Y}\tilde{Z}$, fixed to the lateral surface of the elliptical disk. Point $\tilde{O}$ is located at the center of the ellipsoid describing the lateral surface of the disk; the directions of $\tilde{O}\tilde{X}$ and $\tilde{O}\tilde{Y}$ coincide with those for the $\overline{O}\overline{X}\overline{Y}\overline{Z}$ sys-

tem. The transformation from $\bar{O}\bar{X}\bar{Y}\bar{Z}$ to $\tilde{O}\tilde{X}\tilde{Y}\tilde{Z}$ is given by the formulas (see formulas (4) in [11]):

$$\begin{aligned} \tilde{x} &= \bar{x} + ea, \\ \tilde{y} &= \bar{y}, \\ \tilde{z} &= \bar{z}, \end{aligned} \tag{1}$$

where e is the eccentricity of the elliptical disk and a its semi-major axis. The semi-axis b can be determined from the relation $b = a\sqrt{1-e^2}$.

(4) The basic coordinate frame $OXYZ$ is fixed to the center of mass of the secondary. The OX and OY axes lie in the orbital plane, OX is directed toward the center of mass of the spherical component, OY is perpendicular to it, and the motion from OY to OX is counterclockwise. In this frame, the coordinates of the center of the spherical star are

$$\begin{aligned} x_w &= 1, \\ y_w &= 0, \\ z_w &= 0. \end{aligned} \tag{2}$$

The transformation from $\bar{O}\bar{X}\bar{Y}\bar{Z}$ to $OXYZ$ is given by the formulas [11]

$$\begin{aligned} x &= 1 - \bar{x}\cos\alpha_e - \bar{y}\sin\alpha_e, \\ y &= \bar{x}\sin\alpha_e - \bar{y}\cos\alpha_e, \\ z &= \bar{z}. \end{aligned} \tag{3}$$

3. MODELING THE HOT LINE

Let us construct the figure of the spindle. We will take the semi-axes of the ellipsoid describing the region of shock radiation to be a_v, b_v, c_v (Fig. 1). Let a ray drawn in the orbital plane from the inner Lagrangian point L_1 toward the elliptical disk be tangent to its lateral surface at a point M with coordinates $\tilde{O}\tilde{X}\tilde{Y}\tilde{Z}$ $(\tilde{x}_M, \tilde{y}_M)$ in the $\tilde{O}\tilde{X}\tilde{Y}\tilde{Z}$ system. The length of the radius vector R_ψ from the center of the spherical star $\bar{O}$ to point M can be determined from the two relations

$$R_\psi = a - e\tilde{x}_M, \tag{4}$$

and using the value of the angle ψ_M between the radius vector R_ψ and the $\bar{O}\bar{X}$ axis:

$$R_\psi = \frac{a(1-e^2)}{1 + e\cos\psi_M}. \tag{5}$$

Hence, it is straightforward to derive the coordinate $\tilde{x}_M$ of the point of tangency M:

$$\tilde{x}_M = \frac{a(\cos\psi_M + e)}{1 + e\cos\psi_M}. \tag{6}$$

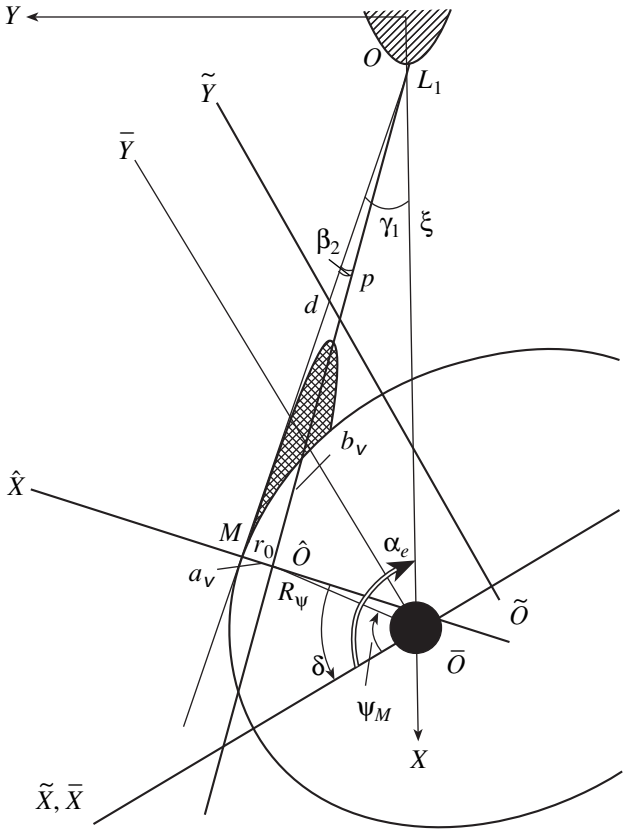

Fig. 1. Coordinate frames used for spindle figure construction.

The second coordinate $\tilde{y}_M$ is determined by substituting $\tilde{x}_M$ into the equation for the ellipse describing the lateral disk surface for $\tilde{z} = 0$, $\frac{\tilde{x}^2}{a^2} + \frac{\tilde{y}^2}{b^2} - 1 = 0$, whence

$$\tilde{y}_M = \frac{b\sin\psi_M\sqrt{1-e^2}}{1 + e\cos\psi_M}. \tag{7}$$

We now substitute the coordinates of M into the equation for the tangent to the disk in the orbital plane

$$\frac{\tilde{x}_M\tilde{x}_L}{a^2} + \frac{\tilde{y}_M\tilde{y}_L}{b^2} = 1, \tag{8}$$

where,

$$\begin{aligned} \tilde{x}_L &= \xi\cos\alpha_e + ea, \\ \tilde{y}_L &= \xi\sin\alpha_e \end{aligned} \tag{9}$$

are the coordinates of the inner Lagrangian point in the $\tilde{O}\tilde{X}\tilde{Y}\tilde{Z}$ frame, and ξ is the distance between the Lagrangian point and the center of the white dwarf. Given the ratio of the primary and secondary masses $q = M_w/M_2$, we can calculate ξ in accordance with [13]. We can now determine angle ψ_M made by the radius

vector R_ψ drawn to the point of tangency M and the $\bar{O}\bar{X}$ axis:

$$\cos(\alpha_e - \psi_M) = \frac{a}{\xi}(1 - e^2) - e\cos\alpha_e, \qquad (10)$$

and also the radius vector R_ψ itself, in accordance with (5). Note that, for some orientations of the disk ($\alpha_e \cong$ 270°–370°), relation (10) can be negative: $\cos(\alpha_e - \psi_M) <$ 0. Denoting $U = \sqrt{1 - \cos^2(\alpha_e - \psi_M)}$, we obtain $\psi_M = \alpha_e - \arcsin U$ for $\cos(\alpha_e - \psi_M) > 0$ and $\psi_M = \alpha_e - \arcsin U + \pi$ for $\cos(\alpha_e - \psi_M) < 0$.

Let us now move along the radius vector R_ψ from M toward the center of primary $\bar{O}$ a distance r_0 (Fig. 1). Let us suppose that the center of the spindle (and the center of the $\hat{O}\hat{X}\hat{Y}\hat{Z}$ frame) is located here. The semi-major axis b_v of the spindle ellipsoid is oriented along the line connecting point L_1 and center $\hat{O}$. The semi-minor axis a_v is perpendicular to b_v and lies in the orbital plane. In general, the orientation of a_v does not coincide with the direction of the radius vector R_ψ. The semi-axis c_v is perpendicular to the orbital plane.

The lengths of the spindle semi-axes a_v, b_v, and c_v are parameters of the problem. The semi-axis c_v is limited by the maximum height of the disk edge z_{cr} (see formula (26) in [11]). The value of a_v is determined below in terms of parameter r_0. From qualitative reasoning, r_0 cannot exceed ~$0.5R_p$, where R_p is the radius of the disk at its periastron and $R_p = a(1 - e)$. The semi-axis b_v is restricted by the distance p between the inner Lagrangian point and the center of the spindle. The distance p between L_1 and the spindle center $\hat{O}$ can easily be determined from the coordinates of the Lagrangian point ($\xi\cos\alpha_e$, $\xi\sin\alpha_e$) and the spindle center ($\bar{x}_0 = (R_\psi - r_0)\cos\psi_M$, $\bar{y}_0 = (R_\psi - r_0)\sin\psi_M$) in the $\bar{O}\bar{X}\bar{Y}\bar{Z}$ frame:

$$p = \sqrt{\xi^2 - 2\xi(R_\psi - r_0)\cos(\alpha_e - \psi) + (R_\psi - r_0)^2}. \qquad (11)$$

Similarly, the distance d between L_1 and the point of tangency M is

$$d = \sqrt{\xi^2 - 2\xi R_\psi\cos(\alpha_e - \psi) + R_\psi^2}. \qquad (12)$$

Parameters p and d are necessary to determine the semi-minor axis of the spindle ellipsoid a_v, since $a_v = p\tan\beta_2$, where β_2 is the angle between the semi-major axis of spindle b_v and the tangent ML_1 to the disk from point L_1. The angle δ between the corresponding axes of the $\hat{O}\hat{X}\hat{Y}\hat{Z}$ and $\bar{O}\bar{X}\bar{Y}\bar{Z}$ coordinate frames (Fig. 1) is calculated using the relation

$$\delta = 0.5\pi - \alpha_e - \gamma_1 + \beta_2, \qquad (13)$$

where β_2 and the angle γ_1 between tangent ML_1 and the horizontal axis of the system are determined from elementary trigonometric relations:

$$\sin\gamma_1 = \frac{R_\psi}{d}\sin(\alpha_e - \psi_M), \qquad (14)$$

$$\sin\beta_2 = \frac{r_0}{p}\sin(\gamma_1 - \psi_M + \alpha_e). \qquad (15)$$

Angle δ is measured from the $\hat{O}\hat{X}$ axis toward the $\bar{O}\bar{X}$ axis. Thus, the point on the spindle surface with coordinates ($\hat{x}$, $\hat{y}$, $\hat{z}$) in the spindle frame has the following coordinates in the disk frame $\bar{O}\bar{X}\bar{Y}\bar{Z}$:

$$\begin{aligned} \bar{x} &= \hat{x}\cos\delta + \hat{y}\sin\delta + (R_\psi - r_0)\cos\psi_M, \\ \bar{y} &= \hat{y}\cos\delta - \hat{x}\sin\delta + (R_\psi - r_0)\sin\psi_M, \\ \bar{z} &= \hat{z}. \end{aligned} \qquad (16)$$

The inverse transformation can be made using the formulas

$$\begin{aligned} \hat{x} &= \bar{x}\cos\delta - \bar{y}\sin\delta - (R_\psi - r_0)\cos(\psi_M + \delta), \\ \hat{y} &= \bar{y}\cos\delta + x\sin\delta - (R_\psi - r_0)\sin(\psi_M + \delta), \\ \hat{z} &= \bar{z}. \end{aligned} \qquad (17)$$

When constructing the figure of the spindle, we will conventionally assume that its surface is limited to the region of non-negative $\hat{y}$ coordinates. When the spindle surface is being formed, some of the points describing it will fall in the disk area. In this case, we will take these points to not belong to the spindle. To test whether this condition is met, we substitute the coordinates of a spindle surface element ($\bar{x}_v$, $\bar{y}_v$, $\bar{z}_v$) in the coordinate frame $\bar{O}\bar{X}\bar{Y}\bar{Z}$ into the equation of the ellipsoid describing the lateral disk surface in the same frame:

$$U = \frac{(\bar{x}_v + ea)^2}{a^2} + \frac{\bar{y}_v^2}{b^2} + \frac{\bar{z}_v^2}{c^2} - 1 = 0. \qquad (18)$$

If $U \le 0$, the spindle surface element belongs to the body of the disk. Similarly we can check whether some elements of the disk's lateral surface are inside the spindle. The coordinates ($\hat{x}_d$, $\hat{y}_d$, $\hat{z}_d$) of a point on the disk are substituted into the equation for the spindle ellipsoid in the $\hat{O}\hat{X}\hat{Y}\hat{Z}$ frame:

$$U' = \frac{\hat{x}^2}{a_v^2} + \frac{\hat{y}^2}{b_v^2} + \frac{\hat{z}^2}{c_v^2} - 1 = 0. \qquad (19)$$

When $U' \le 0$, the disk surface element is covered by the body of the spindle. The normals **n** to the surface of the

spindle ellipsoid in the $\hat{O}\hat{X}\hat{Y}\hat{Z}$ frame are

$$\hat{n} = \left\{\frac{\hat{x}}{a_v^2 H}, \frac{\hat{y}}{b_v^2 H}, \frac{\hat{z}}{c_v^2 H}\right\}, \quad (20)$$

where

$$H = \sqrt{\frac{\hat{x}^2}{a_v^4} + \frac{\hat{y}^2}{b_v^4} + \frac{\hat{z}^2}{c_v^4}}. \quad (21)$$

Accordingly, the components of the normal to the spindle surface in the $\bar{O}\bar{X}\bar{Y}\bar{Z}$ and $\tilde{O}\tilde{X}\tilde{Y}\tilde{Z}$ frames will be calculated using the formulas

$$\begin{aligned} \tilde{n}_x &= \bar{n}_x = \hat{n}_x\cos\delta + \hat{n}_y\sin\delta, \\ \tilde{n}_y &= \bar{n}_y = \hat{n}_y\cos\delta - \hat{n}_x\sin\delta, \\ \tilde{n}_z &= \tilde{n}_z = \hat{n}_z. \end{aligned} \quad (22)$$

It is more convenient to calculate the area of a spindle surface element in spherical coordinates. We denote $\hat{\phi}$ to be the angle between the projection of the radius vector from center $\hat{O}$ to a point $(\hat{x}, \hat{y}, \hat{z})$ in the $\hat{O}\hat{X}\hat{Z}$ plane and the $\hat{O}\hat{X}$ axis. This angle ranges from 0 to 2π. We denote $\hat{\eta}$ to be the angle between the $\hat{O}\hat{Y}$ axis and the radius vector drawn from $\hat{O}$ to the center of the considered surface element on the spindle; this angle ranges from 0 to 0.5π, i.e., over the positive $\hat{O}\hat{Y}$ axis. Due to the very elongated shape of the spindle ellipsoid, the grid in $\hat{\eta}$ must be inhomogeneous: finer at the spindle vertex and coarser near the $\hat{O}\hat{X}\hat{Z}$ plane. We can obtain this type of gridding for angle $\hat{\eta}$, for example, as follows. We will divide the semi-axis b_v of the spindle into n_b equal sections and calculate their $\hat{y}_i$ coordinates. For each point in the $\hat{O}\hat{Y}\hat{Z}$ plane with coordinate $\hat{y}_i$, there exists a corresponding $\hat{z}_i$ coordinate $\hat{z}_i = c_v\sqrt{1-\hat{y}_i^2/b_v^2}$, and angle $\hat{\eta}_i$ determined from the relation $\hat{\eta}_i = \arctan(\hat{z}_i/\hat{y}_i)$.

Substituting the components of the radius vector $(\hat{x}, \hat{y}, \hat{z})$

$$\begin{aligned} \hat{x} &= \hat{r}\sin\hat{\eta}\cos\hat{\phi}, \\ \hat{y} &= \hat{r}\cos\hat{\eta}, \\ \hat{z} &= \hat{r}\sin\hat{\eta}\sin\hat{\phi}, \end{aligned} \quad (23)$$

into (19), we obtain the radius vector $\hat{r}$ in spherical coordinates:

$$\hat{r} = \frac{1}{\sqrt{\dfrac{\sin^2\hat{\eta}\cos^2\hat{\phi}}{a_v^2} + \dfrac{\cos^2\hat{\eta}}{b_v^2} + \dfrac{\sin^2\hat{\eta}\sin^2\hat{\phi}}{c_v^2}}}. \quad (24)$$

The area of the spindle surface element is $dS = H\hat{r}^3\sin\hat{\eta}\,d\hat{\eta}\,d\hat{\phi}$ (for a detailed derivation of this formula, see [9, 10]).

When specifying the temperature of the spindle surface elements, we should bear in mind that the position of the region of shock energy release depends on numerous factors, in particular the velocity of the gas flow in the stream, the density, etc. Therefore, for the sake of simplicity, we will specify the maximum temperature of the spindle both on the side of the inflowing matter (i.e., for $\hat{x} < 0$) and on the opposite side ($\hat{x} \geq 0$). The distributions of the surface-element temperatures on both sides of the spindle will be matched to these $T_{\max}$ values. We can use the following relations to calculate the temperature of a surface element of the spindle ellipsoid. Let $T_{\max}$ be the maximum temperature of the spindle surface on the side of the inflowing matter, reached at distance $\hat{y}_{\max}$. The temperatures of surface elements along the $\hat{O}\hat{Y}$ axis can be one of the following:

(1) constant,

$$T_i = T_{\max} = \text{const};$$

(2) distributed normally,

$$T_i = T_{\max}\exp(-0.5\Delta\hat{y}_i^2), \text{ where } \Delta\hat{y}_i = \frac{\hat{y}_i - \hat{y}_{\max}}{\hat{y}_0 - \hat{y}_{\max}}; \quad (25)$$

(3) distributed as a cosine function,

$$T_i(\hat{y}) = T_{\min} + T_{\max}\cos(0.5\pi\Delta\hat{y}_i). \quad (26)$$

In this last case, the temperature increment reaches its maximum at the point with coordinate $\hat{y}_{\max}$, while the temperature increment equals zero at the point with coordinate $\hat{y}_0$, $T_i(\hat{y}) = T_{\min}$. The minimum temperature for a spindle surface element can be taken to be equal, for example, to the temperature that the disk matter would have due to reprocessing of the gravitational energy of the gas into heat during the motion of the gas toward the gravitating object [14]:

$$T_{\min} = T_w\left(\frac{R_w}{\bar{r}}\right)^{3/4}, \quad (27)$$

where R_w and T_w are the radius and surface temperature of the primary component and $\bar{r}$ is the distance from the spindle pole to the center of the primary in the disk coordinate frame. The temperatures of spindle surface elements on the side opposite to the inflowing matter are calculated analogously. Figure 2 presents three temperature distributions along the spindle corresponding to the three relations above, assuming that the minimum temperature is reached at the spindle pole. By varying the positions of the temperature maximum and minimum on the spindle surface, the temperature values themselves on both sides of the spindle, and the temperature distributions, we can describe the radiation

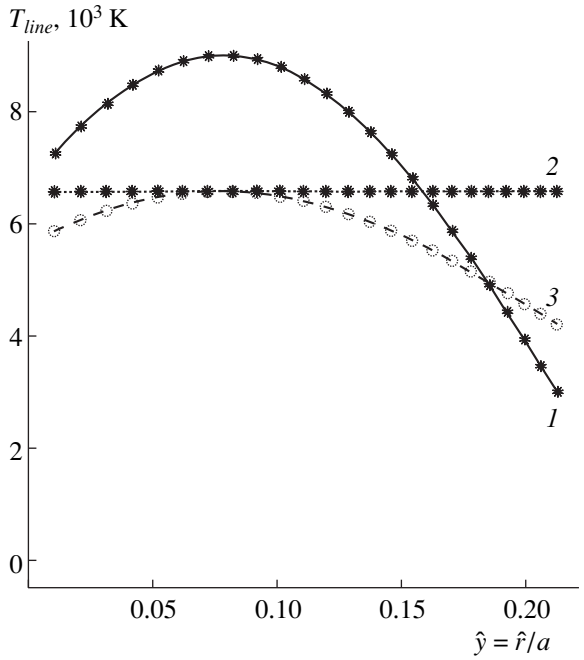

Fig. 2. Variation of the temperature along the "hot line" on the side of the inflowing matter as a function of distance to the center of the spindle ellipsoid $\hat{y} = \hat{r}/a_0$, for the following laws: $T_{line}(\hat{y}) = T_{\min} + T_{\max}\cos(0.5\pi\hat{y}_i^2)$ (*1*), $T_{line}(\hat{y}) = T_{\max} = \text{const}$ (*2*), $T_{line}(\hat{y}) = T_{\max}\exp(-0.5\Delta\hat{y}_i^2)$ (*3*), where $\Delta\hat{y}_i = \dfrac{\hat{y}_i - \hat{y}_{\max}}{\hat{y}_0 - \hat{y}_{\max}}$ (see text).

from a given structure with adequate accuracy. Unfortunately, this considerably increases the number of unknowns in the problem. Therefore, it is sensible to apply the procedure for determining the observed parameters of the shock region to CBSs whose basic parameters (q, i, T_2, T_w, R_w, R_d) have already been determined reliably from other data.

4. VERIFICATION OF ECLIPSE CONDITIONS

The verification of the visibility of surface elements for all components of the system is based on the following general principle. Knowing the coordinates for the center of a surface element in the *OXYZ* frame, (x_i, y_i, z_i), and the direction cosines for the line of sight,

$$\begin{aligned} o_x &= \cos\varphi_0 \sin i, \\ o_y &= \sin\varphi_0 \sin i, \\ 0_z &= \cos i, \end{aligned} \tag{28}$$

where i is the orbital inclination and φ_0 the observer's azimuth, we can determine the angle γ between the normal **n** to the surface element and the line of sight:

$$\cos\gamma = \frac{\mathbf{n}\cdot\mathbf{o}}{|\mathbf{n}||\mathbf{o}|} \tag{29}$$

(the relation between the orbital phase φ and the observer's azimuth φ_0 is specified by the expression $\varphi_0 = \varphi + \pi$; i.e., at the lower conjunction of the secondary, the orbital phase is $\varphi = 0$ and the observer's azimuth $\varphi_0 = \pi$). The condition for visibility of the surface element is $\cos\gamma > 0$. If this condition is fulfilled, we verify the possibility of eclipse of the surface element by other components of the system. For this purpose, we draw in parametric form a straight line through the center of the surface element parallel to the line of sight:

$$\begin{aligned} X &= x_i + to_x, \\ Y &= y_i + to_y, \\ Z &= z_i + to_z, \end{aligned} \tag{30}$$

and elucidate whether it intersects the surfaces of other components in the interval between the observer and the test surface element. For this, the system of equations (30) and the equation describing the shape of the considered component of the CBS in the *OXYZ* frame must be solved simultaneously in terms of the parameter t, taking into account any additional conditions. The absence of a solution indicates that the line of sight does not intersect the body of the component considered. If there is an intersection, but it is beyond the region satisfying some additional conditions (for example, it occurs in the area above the disk edge, $Z > z_{cr}$) or beyond the boundaries of the interval between the observer and the test surface element, the surface element is likewise not eclipsed, and its contribution to the total flux from the system must be taken into account in accordance with its calculated temperature, size, and viewing angle γ. The eclipse verification procedure for the primary and secondary components of the CBS and the elliptical disk is described in detail in [9–11].

A surface element on the spindle can be eclipsed by the body of the spindle itself, the body of the secondary component, the body of the spherical star, and the lateral surface of the elliptical disk. If $o_x n_{xv} + o_y n_{yv} + o_z n_{zv} \le 0$, where $\mathbf{n}_v$ is the normal to the spindle surface element in the *OXYZ* frame, the given surface element is not visible at that orbital phase φ.

The red dwarf can eclipse the spindle only at orbital phases $\varphi > 2.5\pi$ and $\varphi < 1.5\pi$, when the star is near its lower conjunction. Eclipse verification for a spindle surface element is similar to that for a disk surface element [10, 11].

Verification of eclipse of a spindle surface element $(\bar{x}_v, \bar{y}_v, \bar{z}_v)$ by the primary is similar to that for an eclipse of a disk surface element by the spherical star, presented in [11]. The white dwarf does not eclipse a test surface element if $D = (B/A)^2 - C/A < 0$, where

$$A = (o_x\cos\alpha_e - o_y\sin\alpha_e)^2$$

$$+ (o_x\sin\alpha_e + o_y\cos\alpha_e)^2 + o_z^2,$$

$$B = \bar{x}_v(o_x\cos\alpha_e - o_y\sin\alpha_e) \quad (31)$$
$$+ \bar{y}_v(o_x\sin\alpha_e + o_y\cos\alpha_e) - \bar{z}_v o_z,$$
$$C = \bar{x}_v^2 + \bar{y}_v^2 + \bar{z}_v^2 - R_w^2.$$

Finally, we verify the eclipse of the center of a spindle surface element by the lateral (ellipsoidal) surface of the elliptical disk. If $D = (B/A)^2 - C/A < 0$, where

$$A = (o_x\cos\alpha_e - o_y\sin\alpha_e)^2$$
$$+ \frac{(o_x\sin\alpha_e + o_y\cos\alpha_e)^2}{1-e^2} + \left(\frac{a}{c}\right)^2 o_z^2,$$
$$B = (o_x\cos\alpha_e - o_y\sin\alpha_e)(\bar{x}_v + ea) \quad (32)$$
$$+ \frac{(o_x\sin\alpha_e + o_y\cos\alpha_e)\bar{y}_v}{1-e^2} - \left(\frac{a}{c}\right)^2 o_z\bar{z}_v,$$
$$C = (\bar{x}_v + ea)^2 + \frac{\bar{y}_v^2}{1-e^2} + \left(\frac{a}{c}\right)^2 \bar{z}_v^2 - a^2,$$

a straight line parallel to the line of sight will never intersect the disk ellipsoid surface, and the spindle surface element will not be eclipsed. Otherwise there is an intersection. However, we will take the spindle surface element to be uneclipsed if the z coordinate of the lower point of intersection exceeds the z coordinate of the upper edge of the disk ($Z = \bar{z}_v + o_z(B/A - \sqrt{D}) < z_{cr}$).

The spindle itself can also eclipse other components: the secondary (within a small interval of orbital phases) and the lateral disk surface. Eclipse of the secondary by the spindle can occur at orbital phases $0.25 < \varphi < 0.75$. A surface element on the red dwarf with coordinates $(\bar{x}_r, \bar{y}_r, \bar{z}_r)$ in the $\bar{O}\bar{X}\bar{Y}\bar{Z}$ frame will be eclipsed by the spindle when $o_z[B/A + \sqrt{(B/A)^2 - C/A}] > 0$. Here,

$$C = \bar{x}_r^2 D_1 + \bar{y}_r^2 D_2 + \frac{a_v^2}{c_v^2}\bar{z}_r^2$$
$$- 2D_3\bar{x}_r\bar{y}_r - 2D_4\bar{x}_r + 2D_5\bar{y}_r + D_6,$$
$$B = FD_1\bar{x}_r + GD_2\bar{y}_r - o_z\frac{a_v^2}{c_v^2}\bar{z}_r \quad (33)$$
$$- D_3(F\bar{y}_r + G\bar{x}_r) - D_4F + D_5G,$$
$$A = F^2D_1 + G^2D_2 - 2D_3FG + \frac{a_v^2}{c_v^2}o_z^2,$$

where $F = o_x\cos\alpha_e - o_y\sin\alpha_e$, $G = o_x\sin\alpha_e + o_y\cos\alpha_e$, and coefficients D_i are calculated in accordance with the relations

$$D_1 = \cos^2\delta + \frac{a_v^2}{b_v^2}\sin^2\delta,$$
$$D_2 = \sin^2\delta + \frac{a_v^2}{b_v^2}\cos^2\delta,$$
$$D_3 = \cos\delta\sin\delta\left(1 - \frac{a_v^2}{b_v^2}\right),$$
$$D_4 = (R_\psi - r_0)$$
$$\times\left[\cos\delta\cos(\delta + \psi_M) + \frac{a_v^2}{b_v^2}\sin\delta\sin(\delta + \psi_M)\right], \quad (34)$$
$$D_5 = (R_\psi - r_0)$$
$$\times\left[\sin\delta\cos(\delta + \psi_M) - \frac{a_v^2}{b_v^2}\cos\delta\sin(\delta + \psi_M)\right],$$
$$D_6 = (R_\psi - r_0)^2$$
$$\times\left[\cos^2(\delta + \psi_M) + \frac{a_v^2}{b_v^2}\sin^2(\delta + \psi_M)\right] - a_v^2.$$

The verification of the eclipse of a lateral disk surface element with coordinates $(\bar{x}_d, \bar{y}_d, \bar{z}_d)$ by the spindle is similar to the procedure above for a red dwarf surface element; in the calculations for coefficients A, B, C (33), the coordinates $(\bar{x}_r, \bar{y}_r, \bar{z}_r)$ must be replaced by $(\bar{x}_d, \bar{y}_d, \bar{z}_d)$.

5. MODEL CALCULATIONS

Let us elucidate how variation of the parameters of a hot line oriented toward the inner Lagrangian point affects the light curve of a CBS. We chose a CBS with $q = 3.0°$ and $i = 80°$ (i.e., an eclipsing system) for test calculations. The disk eccentricity is $e = 0.3$ and its maximum radius (at apastron) is 0.5ξ (ξ is the distance between the center of mass of the spherical star and the inner Lagrangian point, and equals $\xi = 0.611a_0$ when $q = 3.0$, where a_0 is the distance between the centers of mass of the system components); thus, R_d (apastron) = $0.235a_0$. The height of the outer edge of the disk above the orbital plane, specified by the parameter $A_p = 4$, is $z_{cr} = 0.0145a_0$. The parameters of the primary are taken to be equal to those of the white dwarf: temperature $T_w = 25\,000$ K and radius $R_w = 0.011\xi = 0.0067a_0$. The effective temperature of the secondary in the absence of heating from the primary is $T_2 = 3500$ K. The parameters of the spindle, in particular, its semi-axis a_v, depend on the azimuth of the spindle center, since we specify a_v in

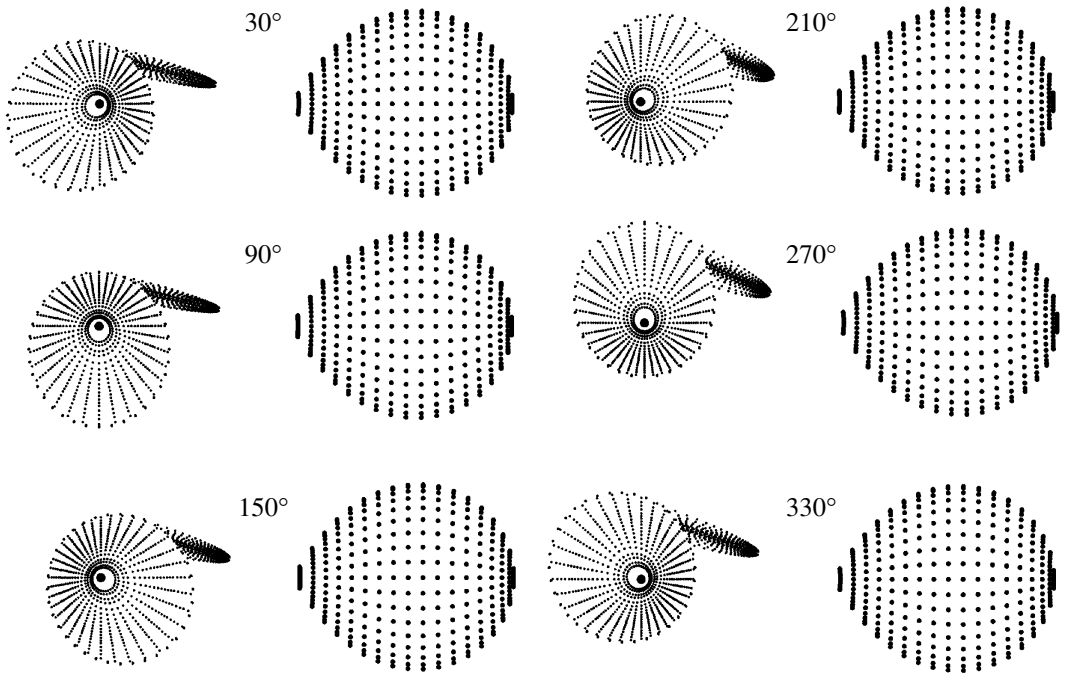

Fig. 3. Hot-line thickness as a function of the rotation angle α_e of the disk relative to the horizontal axis of the system, for fixed $r_0 = 0.2R_\psi$, $b_v = 0.6p$, and $c_v = z_{cr}$, where p is the distance from L_1 to the center of the spindle and z_{cr} is the height of the upper edge of the disk above the orbital plane. The values for the angle α_e are indicated. The system is depicted for $i = 5°$.

terms of the intermediate parameter r_0 in the light-curve synthesis code. Figure 3 shows how the hot line's thickness varies as a function of the rotation angle α_e of the disk periastron relative to the horizontal axis of the system for fixed $r_0 = 0.2R_\psi$ (we take the semi-axes of the spindle to be $b_v = 0.6p$, $c_v = z_{cr}$, where p—the distance from L_1 to the spindle center—also depends on α_e). When $\alpha_e = 30°$, $a_v = 0.036a_0$, and $b_v = 0.37a_0$; when $\alpha_e = 90°$, $a_v = 0.033a_0$ and $b_v = 0.35a_0$; when $\alpha_e = 150°$, $a_v = 0.043a_0$ and $b_v = 0.31a_0$; when $\alpha_e = 210°$, $a_v = 0.059a_0$ and $b_v = 0.30a_0$; when $\alpha_e = 270°$, $a_v = 0.059a_0$ and $b_v = 0.34a_0$; when $\alpha_e = 330°$, $a_v = 0.047a_0$ and $b_v = 0.38a_0$. The system is depicted for the angle $i = 5°$.

The test calculations also showed that, with fixed spindle semi-axes a_v and b_v, the contribution of the spindle's radiation to the total brightness of the system can decrease by up to ~40% of its maximum, depending on the orientation of the disk; however, the orbital phases at which the contribution of the spindle reaches its maximum or minimum remain constant.

Figure 4 displays the effect on the shape of the light curve of varying the spindle length from $0.25p$ to $0.9p$. We adopted the cosine law (26) for the temperature distribution along the spindle; the maximum temperature on the side of the inflowing matter was taken to be $T_{\rm inf}$ = 3000 K, and that on the opposite side to be $T_{\rm opp}$ = 9000 K. According to (27), the matter flow has its minimum temperature at the distance $\hat{y}_0 = b_v$. When $b_v = 0.25p$, when the spindle only slightly pushes out the outer surface boundary of the disk (Fig. 4c, left), the synthesized curve is identical to those obtained in classical hot-spot models (Fig. 4b, curve *4*-I). A longer spindle substantially increases its contribution to the total flux from the system, and also leads to certain variations of the light-curve shape. Figure 4b presents the contribution of the radiation of a spindle with $b_v = 0.9p$ in arbitrary units F_λ in the *V* filter as a function of orbital phase (curve *4*-IV, dashed curve). We can use the relation $f_\lambda = F_\lambda a_0^2 \times 10^{-12}$ erg/s cm^3 to translate the flux into commonly used units, where a_0 is the distance between the stars in cm and F_λ is the flux in the figure in arbitrary units. Apart from the main maximum of the radiation at phases $\varphi \sim 0.6$–0.9, there is an additional flux increase near phase $\varphi \sim 0.1$. Here, the line of sight intersects the part of the spindle located on the side of the inflowing matter.

Depending on the density of the matter, the velocity of its motion in the gas flow, and other conditions, the temperature of the hot line on the side of the inflowing matter can be rather high. This results in a supplementary anomalous hump in the light curve of the system near orbital phases $\varphi \sim 0.1$–0.3, which cannot be explained using classical hot-spot models. Figure 5a presents an example of such a light curve. The solid curve (I) shows the light curve calculated for the same parameters as those in Fig. 4a ($b_v = 0.6p$); the dotted curve (II) shows the light curve for the maximum spindle

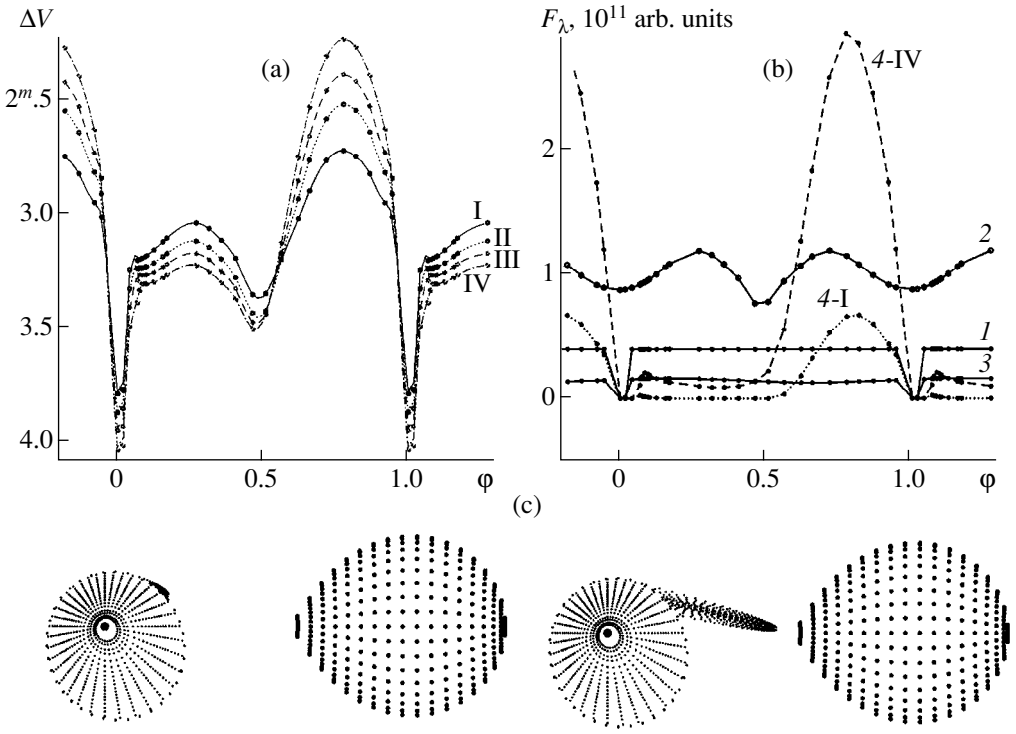

Fig. 4. (a) Relation between the shape of a CBS light curve (with $q = 0.3$, $i = 80°$, $T_2 = 3500$ K, $A_p = 4$, $a = 0.235a_0$, $e = 0.3$, $R_w = 0.0067a_0$, $T_w = 25000$ K, $c_V = 0.0145a_0$, $a_V = 0.036a_0$, $\hat{y}_{\max} = 0.4p$, and $\hat{y}_0 = p$) and spindle length for $b_V = 0.25p$ (I), $0.4p$ (II), $0.6p$ (III), and $0.9p$ (IV). (b) Contribution to the total radiation flux from the spindle for $b_V = 0.25p$ (*4*-I) and $0.9p$ (*4*-IV), the white dwarf (*1*), the red dwarf (*2*), and the elliptical disk (*3*). (c) View of the system from above ($i = 5°$) for spindle lengths $b_V = 0.25p$ (left) and $b_V = 0.9p$ (right).

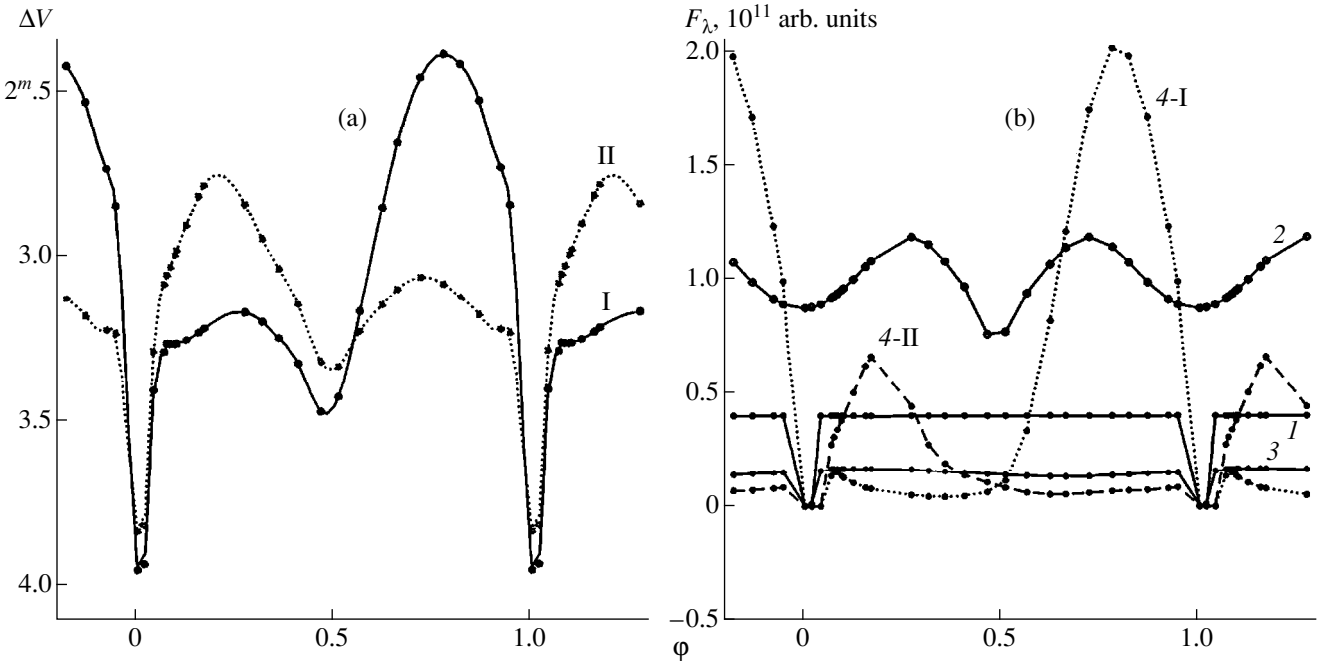

Fig. 5. (a) Light curve of a cataclysmic variable for various maximum temperatures on the spindle surface, $T_{\text{inf}} = 3000$ K and $T_{\text{opp}} = 9000$ K (I), and for the opposite relation, $T_{\text{inf}} = 9000$ K and $T_{\text{opp}} = 3000$ K (II). (b) Contribution to the total radiation flux from the spindle in cases I (curve *4*-I) and II (curve *4*-II), the white dwarf (*1*), the red dwarf (*2*) and the elliptical disk (*3*).

temperature T_{inf} = 9000 K, T_{opp} = 3000 K. Figure 5b shows the contributions of the system components in both cases. With this temperature distribution in the shock region, the peculiar light curves of cataclysmic variables in which the eclipses are located on the ascending branch of the hump (for example, RW Tri, UX UMa [15, 16]) can be explained in a natural way.

At larger orbital inclinations ($i > 75°$), the effect of the compactness of the region of shock energy radiation becomes very significant. The compactness of the "hot" area is specified by parameters $\hat{y}_0$ and $\hat{y}_{max}$. If these two values are close to each other, shock deexcitation occurs within a modest region similar to a classical hot spot, but located on the spindle body rather than on the disk, while the remainder of its surface is cool compared to the lateral disk surface (its temperature does not exceed 1500–2000 K). At orbital phases $\varphi \sim 0.8$–0.9, cool regions of the spindle can eclipse hotter portions of the disk, introducing additional distortions in the light curve. At modest orbital inclinations, the observational effect of the shock compactness is less appreciable. Evidence for compactness of the energy release area is provided by the calculations of [5], which indicate that one characteristic of the shock is variability of its radiation along its length; note that the bulk of the energy release occurs in the part of the shock located near the accretion disk.

6. APPLICATION OF THE HOT-LINE MODEL TO OY CAR

We applied the above procedure for CBS light-curve synthesis using a hot-line model to several well studied SU UMa stars. This is a subclass of cataclysmic variables displaying super-flares of up to 1.5–2^m. The best known characteristic of such super-flares is a superhump in the light curve, which recurs with a period that slightly exceeds the orbital period. According to the theoretical studies of Hirose and Osaki [17], during a super-flare, the accretion disk increases in size to a critical radius and becomes elliptical due to the development of tidal instability called forth by its gravitational interaction with the secondary. In the egress from a flare, the disk decreases in size and becomes circular. The observational verification of this theoretical model is rather complicated, since the details of the elliptical disk structure and its orientation relative to the horizontal axis of the system are time-dependent. Definite progress in the study of the structures of disks and circum-disk formations during flares can be made for systems in which eclipses of the accretion disk by the secondary are observed.

OY Car is one of several SU UMa dwarf novae in which the red dwarf eclipses the white dwarf, the accretion disk around it, and the region of energy release near the outer edge of the disk. Verification of theories for accretion-disk structure is based on precisely this type of system. During super-flares, a secondary hump of lower amplitude appears episodically near orbital phase $\varphi \sim 0.5$. In the hot-line model, this can be explained in a natural way as a consequence of variations in the contributions of the radiation from the spindle and the elliptical disk in the course of its precession.

To determine the parameters of OY Car, we used the *V*-band observations of Bruch *et al.* [18] obtained during a super-flare on April 19 and 20, 1992, and the *B*-band light curve for this system in its quiescent state obtained by Wood *et al.* [19]. By minimizing the fit-residual functional described in detail in [10–12], we derived parameters of the theoretical curves that matched the synthesized curves to the observations (see the table). During the minimization, we fixed the following system parameters, which have been reliably determined by Wood *et al.* [19] in their study of the eclipse shape: $q = M_w/M_2 = 10.0$, $i = 82°$, and the red-dwarf temperature without taking into account heating of its surface by the white dwarf's radiation $T_2 = 3030$ K. We restricted variations for the white-dwarf radius to the interval $R_w/a_0 = 0.018$–0.020. The average radius of the secondary is determined by the mass ratio of the components, and is $R_2/a_0 = 0.213$.

Figure 6 (upper) presents the light curve of OY Car synthesized using this model. The observations are given by the points with their corresponding errors, and the theoretical light curves (constructed using the parameters from the table) are shown by the solid curve. The lower panel of Fig. 6 presents the contributions of the components (the white and red dwarf, elliptical disk, and spindle) as functions of orbital phase for both the active and quiescent states of the system. The resulting parameters of the OY Car system lead to the following conclusions.

(1) The temperature of the white dwarf in the active stage reaches $T_w \sim 35000$–40000 K, and decreases to ~25000 K in the inactive stage. This temperature increase could be due to thermonuclear burning of matter near the surface of the star, thrown there due to instability of the disk.

(2) Due to heating of the secondary surface by the white-dwarf radiation, the average surface temperature of the red dwarf during the super-flare reaches $T_2 \sim 3600$–3700 K; it decreases to $T_2 \sim 3300$ K in the inactive stage. The contribution from the secondary to the total *V* flux in the active stage is 7–10%, and decreases to ≤6% in the inactive stage.

(3) During a super-flare, the disk assumes an elliptical shape, with its eccentricity reaching $e \sim 0.3$–0.7. The maximum eccentricity of the disk is acquired on the date of the maximum of the super-flare in the light curve (April 20, 1992). The disk eccentricity in the inactive state is nearly zero, and the disk shape differs little from circular ($e \sim 0.02$).

(4) The size of the disk is larger in the active than in the inactive stage; $a/a_0 \sim 0.4$–0.45 during the super-flare and ~0.3 in quiescence. The relative half-thick-

OY Car parameters in various phases of activity

Parameter	Commonly accepted values [1, 18, 19]	Classical hot-spot model (I)			"Hot-line" model (II)		
		A (Apr. 19, 1992)	A (Apr. 20, 1992)	Q [19]	A (Apr. 19, 1992)	A (Apr. 20, 1992)	Q [19]
$q = M_w/M_2$	9.1–10.1	9.8	9.8	9.8	10.0	10.0	10.0
i, deg	79–84	82.0	82.0	82.0	82.0	82.0	82.0
R_w/a_0	0.018–0.020	0.0187	0.0195	0.0182	0.0193	0.0193	0.0194
R_2/a_0	0.205–0.213	0.213	0.213	0.213	0.213	0.213	0.213
T_w, K (Q)	10000–15000			21789			25135
T_w, K (A)	~25000	40287	50531		40357	34942	
T_2, K (without heating)	~3000	3030	3030	3030	3030	3030	3030
T_2, K (with heating)		3736	3469	3169	3765	3660	3288
Disk							
a/a_0	0.313–0.355	0.466	0.538	0.277	0.424	0.386	0.315
e	–	–	–	–	0.321	0.699	0.026
z/a	0.020–0.036	0.022	0.059	0.014	0.037	0.033	0.026
α_e	–	–	–	–	219°	323°	251°
Model I							
Spot azimuth	34°–54°	$27\overset{\circ}{.}4$	$54\overset{\circ}{.}7$	$48\overset{\circ}{.}2$			
R_{sp}/a_0	0.027–0.104	0.070	0.156	0.100			
T_{sp}, K	8600–10000	7690	7174	9928			
Model II							
a_v/a_0					0.053	0.125	0.101
b_v/a_0					0.363	0.569	0.334
c_v/a_0					0.016	0.010	0.004
$\langle T_{inf}\rangle$, (T_{max}), K					9769 (16480)	10547 (18827)	3856 (4197)
$\langle T_{opp}\rangle$, (T_{max}), K					6585 (9739)	9514 (14740)	15130 (20073)
χ^2		230	1164	368	112	464	251

A—super-flare stage, Q—inactive stage. Observations during the super-flare were obtained in the *V* filter, and those during the quiescent stage in the *B* filter.

ness of the disk is $z_{cr}/a \sim 0.04$ in the active and ~0.025 in the inactive stage.

(5) The average azimuth of the disk periastron for the April 19, 1992 OY Car light curve, which combines three successive orbital curves, was $\alpha_e = 219°$. The average April 20, 1992 OY Car light curve also combines three successive orbital curves, and has $\alpha_e = 323°$. Consequently, our analysis for the OY Car light curve during this super-flare suggests precession of the disk. Due to the precession of the disk periastron over $0\overset{d}{.}95$ (the time interval between the averaged April 19 and 20 light curves), the disk rotated by 104°. The corresponding precessional period is $P_{prec} = 3\overset{d}{.}289$. According to [17], the period of the motion of super-humps in SU UMa systems is equal to the period of the beating between the orbital and precessional periods of the system; i.e., $1/P_{sh} = 1/P_{orb} - 1/P_{prec}$. In this case, the super-hump period turns out to be $P_{sh} = 0\overset{d}{.}06436$. This value for P_{sh} is consistent with the observed period of the super-hump in OY Car, $P_{sh} = 0\overset{d}{.}0644 \pm 0\overset{d}{.}0002$ [18].

(6) The parameters for the region of energy release obtained from the light-curve analysis correspond to those for an ellipsoid with $\tau > 1$ radiating in accordance with a Planck distribution. The surfaces of the spindle on the side of the inflowing matter and the opposite side radiate with different equilibrium temperatures (see Fig. 7, which presents the temperature distribution over the spindle surface). Only the part of the spindle adjacent to the disk is heated to high temperatures; the areas near the spindle pole have the same temperature that would be displayed by the lateral disk surface at the same distance. During a super-flare, both the average

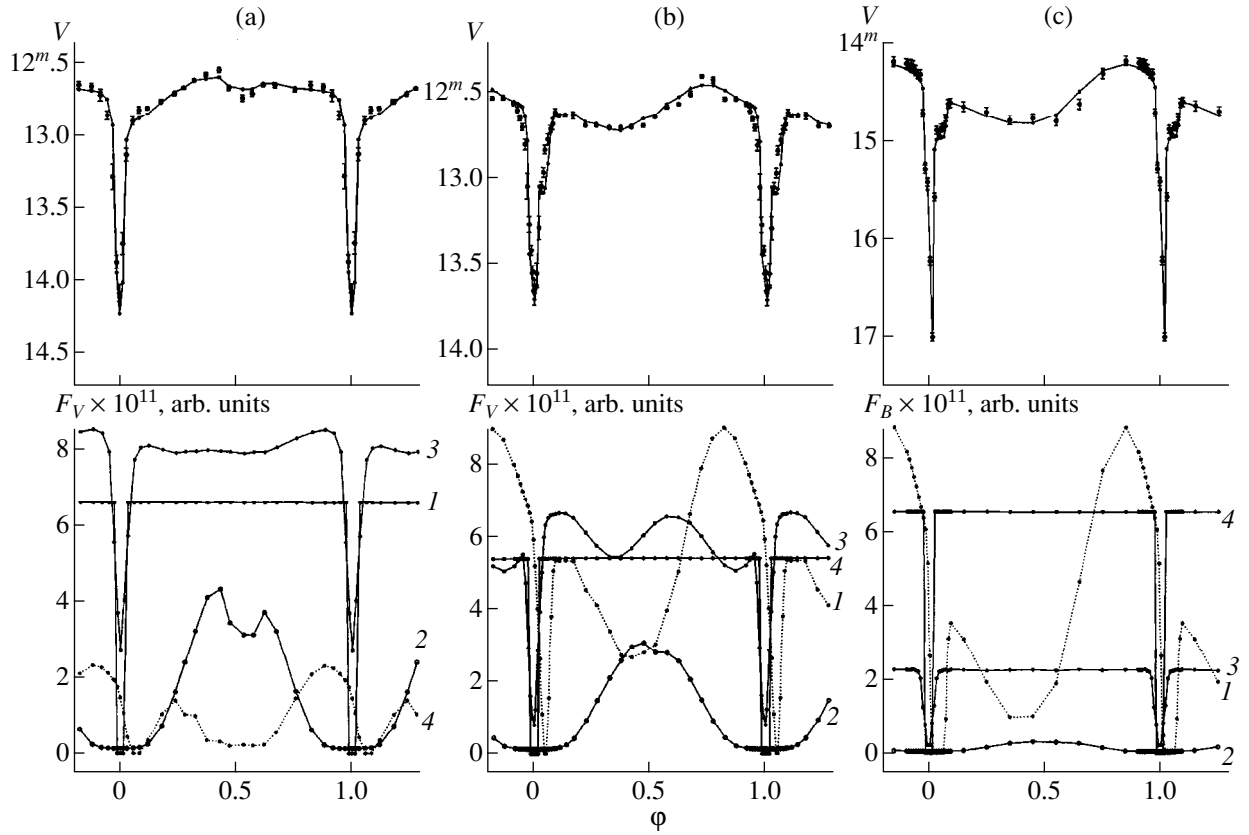

Fig. 6. Upper: observed OY Car light curves during the super-flare on April (a) 19 and (b) 20, 1992 from the *V*-band observations of Bruch *et al.* [18], and (c) in the inactive state according to the *B*-band observations of [19] (points with corresponding errors). Solid curves: synthesized light curves with parameters presented in the table. Lower: contribution to the total radiation flux from the white dwarf (*1*), the red dwarf (*2*), the elliptical disk (*3*), and the spindle (*4*) as a function of orbital phase, used to derive theoretical light curves describing the observations of OY Car during the super-flare on April (a) 19 and (b) 20, 1992, and (c) in the inactive state.

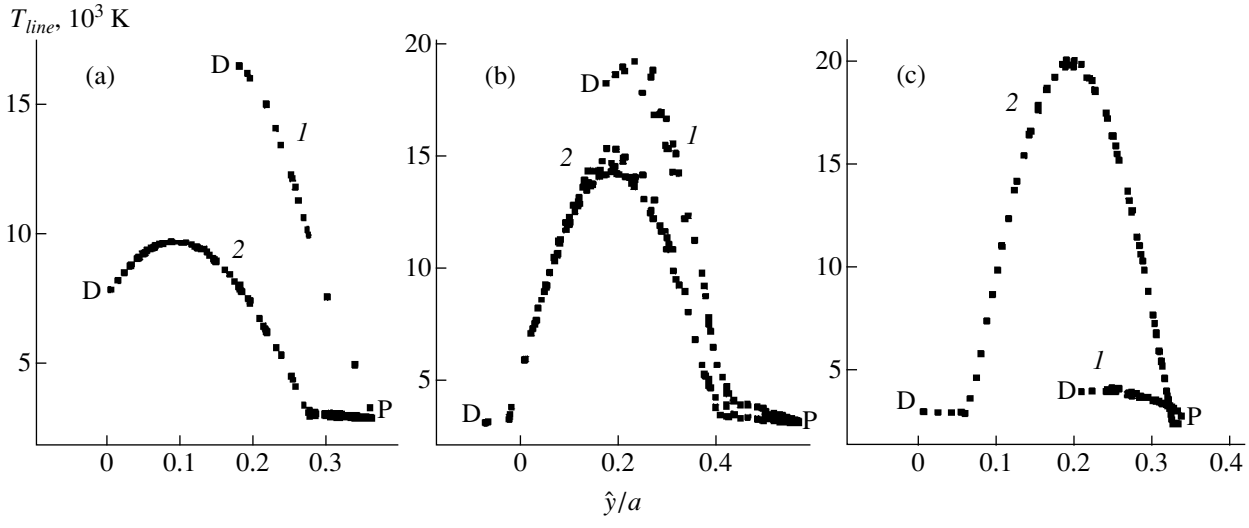

Fig. 7. Temperature distribution of the spindle surface elements ($T = T(\hat{y})$ on the side of the inflowing matter (*1*) and the opposite side (*2*), used to derive theoretical light curves describing the observations of OY Car during the super-flare on April (a) 19 and (b) 20, 1992 and (c) in the inactive state. "D" denotes points of tangency between the spindle and disk surface, "P" denotes the spindle pole.

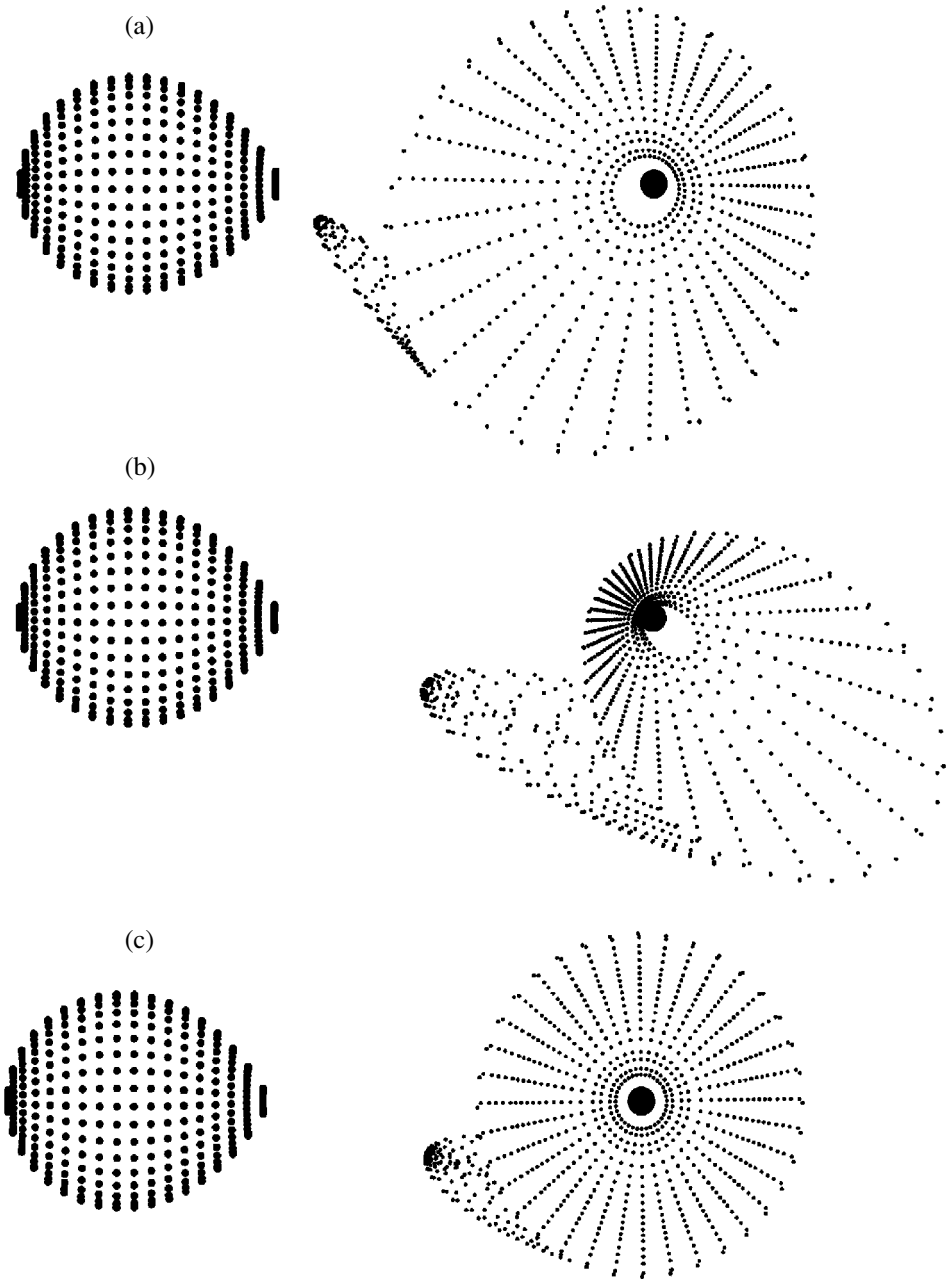

Fig. 8. Computer modeling of the components of OY Car during the super-flare on April (a) 19 and (b) 20, 1992 and (c) in the inactive state. View from above.

and maximum equilibrium temperatures of the spindle surface on the side of the inflowing matter are 10–30% higher than those on the opposite side. During the development of the process, the temperature on the opposite side of the spindle rises. In the inactive state, the situation is reversed: the average equilibrium temperature of the spindle on the side of the inflowing matter is formally equal to only one-third of the temperature on the opposite side. However, the visibility conditions for the radiating surface of the spindle on the side of the inflowing matter are poor, so that the real temperature could be higher.

(7) The brightness of the OY Car system in magnitudes is $1^m.1$ higher in the active than in the inactive stage. This is somewhat smaller than the observed $\Delta V \sim 1^m.5$.

(8) When the same OY Car light curves are described using a classical hot-spot model, the agreement between the observed and theoretical light curves

is generally poorer (see table); details of the light curves out of eclipse are especially poorly represented.

Figure 8 depicts the components of OY Car in various phases of activity, seen at an angle $i = 0°$ (along the system's pole). Variation in the size, shape, and orientation of the disk and the size of the spindle in the course of the super-flare, and also their difference from the parameters for the disk and circum-disk structure in the inactive stage of the system, are clearly demonstrated.

6. CONCLUSIONS

Our model describes an extended region of energy release along the gas stream flowing around the elliptical disk around the white dwarf. The model can reproduce the observed variety of the light curves of cataclysmic variables in more detail than the usual classical model and its various modifications. In our model, anomalous light curves and details of "double eclipses" in systems with high orbital inclinations can be understood, especially in cases when the radiation from circum-disk structures substantially contributes to the total brightness of the system (as, for example, in OY Car). The consistency of our model with the gas-dynamical flow patterns in semi-detached CBSs makes it possible to use it as a basis for interpreting the light curves of cataclysmic variables.

ACKNOWLEDGMENTS

The author is grateful to A.M. Cherepashchuk for useful discussions. This study was supported by the Russian Foundation for Basic Research (project codes 99-02-17589 and 00-02-16471), the State Science and Technological Program "Astronomy. Basic Space Research" (Nos. 1.4.2.1 and 1.4.2.2), and the Federal Programs "Scientific Schools" (No. 00-15-96553) and "Universities of Russia" (No. 991786).

REFERENCES

1. A. M. Cherepashchuk, N. A. Katysheva, T. S. Khruzina, and S. Yu. Shugarov, *Highly Evolved Close Binary Stars. Catalog*, Ed. by A. M. Cherepashchuk (Gordon and Breach, Brussels, 1996).
2. D. V. Bisikalo, A. A. Boyarchuk, O. A. Kuznetsov, and V. M. Chechetkin, Astron. Zh. **74**, 880 (1997) [Astron. Rep. **41**, 786 (1997)]; Astron. Zh. **74**, 889 (1997) [Astron. Rep. **41**, 794 (1997)].
3. D. V. Bisikalo, A. A. Boyarchuk, V. M. Chechetkin, *et al.*, Mon. Not. R. Astron. Soc. **300**, 39 (1998).
4. D. V. Bisikalo, A. A. Boyarchuk, O. A. Kuznetsov, and V. M. Chechetkin, Astron. Zh. **75**, 706 (1998) [Astron. Rep. **42**, 621 (1998)].
5. D. V. Bisikalo, A. A. Boyarchuk, O. A. Kuznetsov, *et al.*, Astron. Zh. **75**, 40 (1998) [Astron. Rep. **42**, 33 (1998)].
6. T. Matsuda, M. Makita, and H. M. J. Boffin, in *Disk Instabilities in Close Binary Systems*, Ed. by S. Mineshige and J. C. Wheeler (Universal Acad. Press, Tokio, 1999), p. 129.
7. M. Makita, K. Miyawaki, and T. Matsuda, Mon. Not. R. Astron. Soc. **316**, 906 (2000).
8. T. S. Khruzina, Astron. Zh. **68**, 1211 (1991) [Sov. Astron. **35**, 607 (1991)].
9. T. S. Khruzina, Astron. Zh. **69**, 58 (1992) [Sov. Astron. **36**, 29 (1992)].
10. T. S. Khruzina, Astron. Zh. **75**, 209 (1998) [Astron. Rep. **42**, 180 (1998)].
11. T. S. Khruzina, Astron. Zh. **77**, 510 (2000) [Astron. Rep. **44**, 446 (2000)].
12. I. B. Voloshina and T. S. Khruzina, Astron. Zh. **77**, 109 (2000) [Astron. Rep. **44**, 89 (2000)].
13. N. I. Balog, A. V. Goncharskiĭ, Z. Yu. Metlitskaya, and A. M. Cherepashchuk, Perem. Zvezdy **21**, 695 (1982).
14. N. I. Shakura and R. A. Sunyaev, Astron. Astrophys. **24**, 337 (1973).
15. M. Hack, in *Cataclysmic Variables and Related Objects*, Ed. by M. Hack and C. la Dous (US Government Printing Office, Washington, 1993), Part 1.
16. K. Horne and R. F. Stiening, Mon. Not. R. Astron. Soc. **216**, 933 (1985).
17. M. Hirose and Y. Osaki, Publ. Astron. Soc. Jpn. **42**, 135 (1990).
18. A. Bruch, D. Beele, and R. Baptista, Astron. Astrophys. **306**, 151 (1996).
19. J. H. Wood, K. Horne, G. Berriman, and R. A. Wade, Astrophys. J. **341**, 974 (1989).

Translated by K. Maslennikov

Astronomy Reports, Vol. 45, No. 4, 2001, pp. 269–280. Translated from Astronomicheskiĭ Zhurnal, Vol. 78, No. 4, 2001, pp. 313–326.

Velocity Field of the Stellar Wind of the Wolf–Rayet Star in the V 444 Cyg Binary System: A Parametric Model

I. I. Antokhin and A. M. Cherepashchuk

Sternberg Astronomical Institute, Universitetskiĭ pr. 13, Moscow, 119899 Russia

Received July 3, 2000

Abstract—An analysis of the λ4244 Å continuum light curve of the eclipsing variable V444 Cyg is used to reconstruct the velocity law $v(r)$ of the stellar wind of the WR star in terms of Lamers parametric and power-law models. Both models are inconsistent with the observed light curve, and can be rejected at the < 2% significance level. Departures of the Lamers parametric relation from the empirical $v(r)$ law reconstructed in previous papers from the same λ 4244 Å light curve on sets of concave and convexo-concave functions are statistically significant. The stellar wind of the WN5 star continues to accelerate at a considerable distance from the star's center. This corresponds to an acceleration parameter $\beta > 1$ in terms of a coarse Lamers-law approximation for the empirical $v(r)$ field. © *2001 MAIK "Nauka/Interperiodica".*

1. INTRODUCTION

Modern models for the extended atmospheres of Wolf–Rayet (WR) stars for computing emitted spectra include a parametric velocity law $v(r)$ for the radial mass outflow as a function of distance r from the center. No full, self-consistent stellar-wind models for WR stars that incorporate gas-dynamical computations and solutions of the transfer equation are available. This is due both to technical difficulties with implementing such models and the fundamental problem of the mechanism for the acceleration of the stellar wind (see, e.g., [1]). The generally accepted form of the velocity field $v(r)$ was first proposed by Lamers [2]:

$$v(r) = v_\infty\left(1 - \frac{r_c}{r}\right)^\beta. \qquad (1)$$

Here, v_∞ is the terminal velocity at infinity, r_c the hydrostatic radius of the WR star, and β a parameter characterizing the degree of acceleration (small and large β correspond to fast and slow acceleration, respectively).

The value $\beta \simeq 1$ is usually adopted for the stellar winds of hot stars [2]. However, recent evidence points toward rather slow ($\beta > 1$) acceleration in the winds of WR stars [3–6]. Furthermore, the very applicability of the parametric law (1) for the stellar winds of WR stars has become a subject of debate (see, e.g., [6, 7]). Therefore, interpretations of observations that allow independent restrictions to be imposed on $v(r)$ have a special importance.

Earlier [6, 8], we derived an empirical $v(r)$ law by analyzing an atmospheric eclipse in V444 Cyg (WN5 + O6, $P \simeq 4^d.2$); this empirical $v(r)$ law differed from the parametric law (1). Unfortunately, the technique used in those papers makes estimating the statistical significance of the inferred departures rather difficult. Therefore, the aim of the current paper is to test the statistical significance of differences between the empirical law $v(r)$ and parametric law (1) for the WN5 star in the V444 Cyg system.

2. FORMULATION OF THE PROBLEM

The radial mass-velocity profile in the photosphere of the WN5 component can be derived from the primary minimum (WN5 eclipses O6) of the binary light curve. The brightness decrease at the phases of the primary minimum is due to the absorption of light from the O6 component as it passes through the semi-transparent photosphere of the WN5 component. The absorption coefficient a distance r from the center of the WN5 star is proportional to the electron density of the photosphere, which, in turn, is related to $v(r)$ through the continuity equation. These relations can be written

$$1 - l_1(\theta) = \int_0^{R_a} K_1(\xi, \Delta, r_{O6}) I_0 (1 - e^{-\tau(\xi)}) d\xi. \qquad (2)$$

Here, θ is the orbital phase angle; $1 - l_1(\theta)$ the loss of light; $K_1(\xi, \Delta, r_{O6})$ a function describing the occultation geometry of the disks of the stellar components (formulas for K_1 can be found, e.g., in [9]); R_a quantity exceeding the total radius of the eclipsing extended atmosphere of the WN5 component; $\Delta^2 = \cos^2 i + \sin^2 i \sin^2\theta$ (in this formula, the component separation is taken to be unity); i the orbital inclination; I_0 the flux density at the center of the disk of the O6 star; and r_{O6} the radius

1063-7729/01/4504-0269$21.00 © 2001 MAIK "Nauka/Interperiodica"

of the O6 star. The line-of-sight optical depth $\tau(\xi)$ of the WN5 star photosphere is given by the formula

$$\tau(\xi) = 2\int_{\xi}^{R_a} \frac{\alpha(r) r dr}{\sqrt{r^2 - \xi^2}}, \quad (3)$$

where $\alpha(r)$ is the absorption coefficient a distance r from the center of the WR star. Obviously, optical photometry cannot penetrate beyond the $\tau(\xi) \sim 1$ layers of the WN5 star photosphere. Let the distance from this point to the center of the disk of the WN5 component be r_0 and the corresponding absorption coefficient be α_0. The absorption in the optical continuum is due primarily to scattering by free electrons, so that the absorption coefficient should be proportional to the density of the material (for a fixed ionization state). Then, in view of the continuity equation, we can write

$$\alpha(r) = \alpha_0 \frac{r_0^2}{r^2} \frac{v_0}{v(r)} s(r), \quad (4)$$

where $v_0 = v(r_0)$ and $v(r)$ is a function describing the dependence of the velocity on distance from the center of the WN5 star. The parameter $s(r)$ in (4) takes into account the ionization state. We assume that the stellar winds of WR stars consist exclusively of helium. In the innermost stellar-wind regions, helium is fully ionized, whereas, at large distances from the WR star, it can become only singly ionized. Since the number of electrons per helium nucleus depends on the ionization state, the formula should include a correction factor: $s(r) = 1$ and $s(r) = 2$ in the He II and He III regions, respectively.

Thus, by solving successively the inverse problems (2) and (3), we can determine $\alpha(r)$ and then derive $v(r)$ from (4). However, in the general case, we must solve not only (2) for the primary minimum of the light curve, but also an analogous equation for the secondary minimum, taking into account the normalization (the so-called "depth equation") relating the two solutions. This is due to the fact that the only way to derive I_0 and reliable estimates of the geometrical parameters affecting the solution (the orbital inclination i and the radius of the O6 star) is to analyze the light curve as a whole.

Equations (2) and (3) belong to the class of so-called ill-posed problems—arbitrarily small variations in the input function can translate into arbitrarily large variations in the solution. Such problems can only be solved by imposing some *a priori* restrictions on the unknown functions. A well known example of such a restriction is approximating an unknown function using a parametric model. For example, the classical theory for interpreting the light curves of eclipsing binaries uses a parametric limb-darkening law for stars with optically thin atmospheres, reducing interpretation of the light curve to the determination of a finite number of parameters (see, e.g., [10]). Since parametric functions always form a compact set, finding a finite number of parameters is always a well-posed inverse problem [11].

There is no satisfactory theory for extended stellar atmospheres, and it is therefore impossible to identify a parametric set of functions that can adequately fit the brightness distribution and absorption properties across the disk of a peculiar star. Cherepashchuk [12, 13] showed that the geometric parameters r_{O6} and i could be derived from the light curve of V444 Cyg without adopting any parametric relations for the functions $I_c(\xi)$ (the brightness distribution across the disk of the WR star reconstructed from the secondary minimum of the light curve) and $1 - e^{-\tau(\xi)}$: one can infer the entire set of unknown quantities r_{O6}, i, $I_c(\xi)$, and $1 - e^{-\tau(\xi)}$ simply by solving the integral equations for the light decrease in the primary and secondary minima. Solving this problem can be made much easier by independently deriving the component luminosity ratio from spectrophotometric data [14]. In this case, the ill-posed nature of the inverse problem can be overcome by choosing a compact set of functions, which need not be parametric, that depends only slightly on the particular physical model for the extended atmosphere and takes into account as much as possible the specific features of the WR star.

Antokhin *et al.* [6, 8] and Cherepashchuk [13] interpreted the λ4244 Å continuum light curve of V444 Cyg using the following *a priori* information about the solution, which allows identification of an appropriate compact set of functions.

(1) The desired functions $I_c(\xi)$ and $1 - e^{-\tau(\xi)}$ are nonnegative, monotonic, and nonincreasing [13].

(2) The function $I_c(\xi)$ is nonnegative and nonincreasing, whereas the function $1 - e^{-\tau(\xi)}$ is concave, nonnegative, monotonic, and nonincreasing, and is bounded from above by a constant equal to unity [6].

(3) The functions $I_c(\xi)$ and $1 - e^{-\tau(\xi)}$ are both convexo-concave, monotonic, nonincreasing, and nonnegative [7, 8]. The convex and concave parts of these functions correspond to the opaque "core" and the extended atmosphere of the WR star, respectively.

The use of *a priori* information about the concave and convexo-concave properties of the unknown functions enabled reconstruction of the spatial structure of the extended atmosphere of the WN5 star and determination of the empirical law $v(r)$ via analysis of an atmospheric eclipse. We emphasize that using all three types of *a priori* information yields virtually the same geometrical parameters r_{O6} and i. In this formulation, two solutions are obtained from the same light curve:

(1) The solution corresponding to the absolute minimum of the residual η: $r_{O6} = 0.25$, $i = 78°.0$, and $L_{WN5}/(L_{WN5} + L_{O6}) = 0.20$, with $\eta_{min} = 0.0036$[1]. Note that

[1] We define the residual as $\eta = \sqrt{\frac{\sum_{i=1}^{n} (l^{th} - l^{obs})^2 w_i}{\sum_{i=1}^{n} w_i}}$, where l^{th} and l^{obs} are the theoretical and intensity-mean observed light curves, respectively, w_i is the weight of the ith normal data point, and n is the number of normal points.

the rms error per normal data point in the light curve is 0.004.

(2) The solution corresponding to the minimum residual η for a fixed relative luminosity of the WN5 star $L_{WN5}/(L_{WN5} + L_{O6}) = 0.38$, derived independently from spectrophotometric observations [14]: $r_{O6} = 0.20$, $i = 78.^\circ4$, with $\eta_{min} = 0.0042$. Since the relative luminosity of the WN5 component is an independently determined observable [14], this second solution should be preferred, in spite of the fact that its residual is 17% higher than in the first case. It is noteworthy that the two solutions lead to the same fundamental qualitative conclusions about the radius of the WR star "core," its temperature, and the velocity field $v(r)$ in the stellar wind.

We can, thus, consider the geometrical parameters of the V444 Cyg binary system to be reliably determined and stable to the use of various types of *a priori* information and to the light-curve rectification procedure [6].

At the same time, the most interesting information about the velocity field in the wind of the WR component was obtained by successively solving two ill-posed problems. In view of the adopted *a priori* assumptions about the solutions, this makes it rather difficult to assess the statistical significance of the conclusions. For this reason, we have approximated the $v(r)$ profile by a parametric function.

By finding a large number of solutions to the direct problem, we can determine the best-fit model parameters and verify their statistical significance. If we adopt (1) as a parametric law $v(r)$, we can assess the statistical significance of the earlier conclusion of [6, 8] that the empirical law $v(r)$ deviated from relation (1). Failure of relation (1) to adequately fit the observed light curve would imply that the departures of the empirical law $v(r)$ from (1) found in [6, 8] are statistically significant and require physical interpretation.

Our initial data were the same rectified λ4244 Å continuum light curve as that used in [6, 8]. To additionally verify the results, we also analyzed the rectified narrow-band λ4789 Å continuum light curve.

3. THE MODEL

We considered two parametric laws for $v(r)$: formula (1) and the power-law relation

$$v(r) = v_0\left(\frac{r}{r_0}\right)^n. \quad (5)$$

We use (4) to compute $\alpha(r)$ only at distances $r > r_0$. Our model assumes infinite optical depth when $\xi < r_0$. The quantity α_0 in (4) is not an independent parameter, and can be derived from the normalization condition $\tau(r_0) = 1$. It can easily be seen that

$$\alpha_0 = \left(2r_0^2 v_0 \int_{r_0}^{R_a} \frac{dr}{r\,v(r)\sqrt{r^2 - r_0^2}}\right)^{-1}. \quad (6)$$

In the general case, the parameters of the problem include the

(1) orbital inclination i;

(2) radius of the O6 star r_{O6};

(3) hydrostatic core radius of the WN5 star r_c (which is obviously less than r_0);

(4) distance r_0 from the center of the disk of the WN5 star where the total optical depth along the line of sight is $\tau(r_0) = 1$;

(5) exponent β of the Lamers law and exponent n of the power-law velocity relation;

(6) radiation intensity at the center of the disk of the O6 star I_0;

(7) radius of the He III region;

(8) linear limb-darkening coefficient x of the O6 star.

Note that neither v_∞ in the Lamers law nor v_0 in the power law can be considered model parameters, as is readily apparent from (6). In fact, R_a is likewise not a free parameter. The radius of the absorbing photosphere of the WN5 star can be assumed to be equal to the separation of the binary components. Here and below, we express all distances in units of this separation ($\sim 38R_\odot$). In this case, $R_a = 1$.

Most of the above parameters can be fixed at values inferred from observations or previous analyses. As noted above, our previous analysis yielded reliable geometrical parameters for the model—i and r_{O6}. We therefore adopted these values and the parameter I_0 from [8]: $i = 78.^\circ43$, $r_{O6} = 0.20$, $I_0 = 5.499$ (model 1) and $i = 78.^\circ0$, $r_{O6} = 0.25$, $I_0 = 4.509$ (model 2). The first solution corresponds to the observed estimate of the relative luminosity of the WN5 star $L_{WN5}/(L_{WN5} + L_{O6}) = 0.38$, and the second to the parameters i and r_{O6} resulting in an absolute minimum of the residual of the theoretical fit to the observed light curve in both minima (the corresponding relative luminosity of the WN5 star is $L_{WN5}/(L_{WN5} + L_{O6}) = 0.20$).

Main-sequence stars are known to obey rather accurately a linear limb-darkening law, whose coefficient for O6 stars is $x = 0.3$ [15].

The problem proved to be insensitive to our choice of the He III-ionization radius, due to the adopted optical-depth normalization a distance r_0 from the center of the WN5 star. Let the radius of the He III ionization region (r(He III) be less than the component separation. This would decrease the electron density $n_e(r)$ at the point $r = r$(He III) by a factor of two. However, the α_0 value computed from (6) increases due to the normaliza-

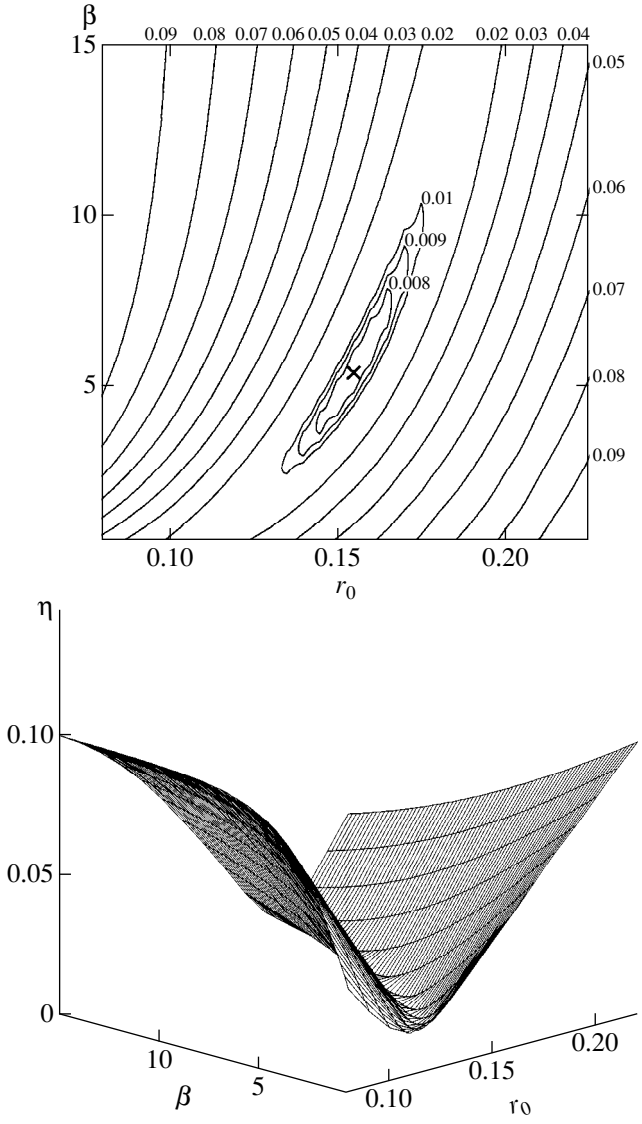

Fig. 1. Residual surface for model 1 ($i = 78.°43$, $r_{O6} = 0.20$, $L_{WN5}/(L_{WN5} + L_{O6}) = 0.38$) with the Lamers law. The upper panel shows contours of equal residual. For ease of viewing, a rarefied grid is shown on the three-dimensional plots, though a grid a factor of a few denser was used in the actual computations: drawing such a grid here would fully blacken the plot.

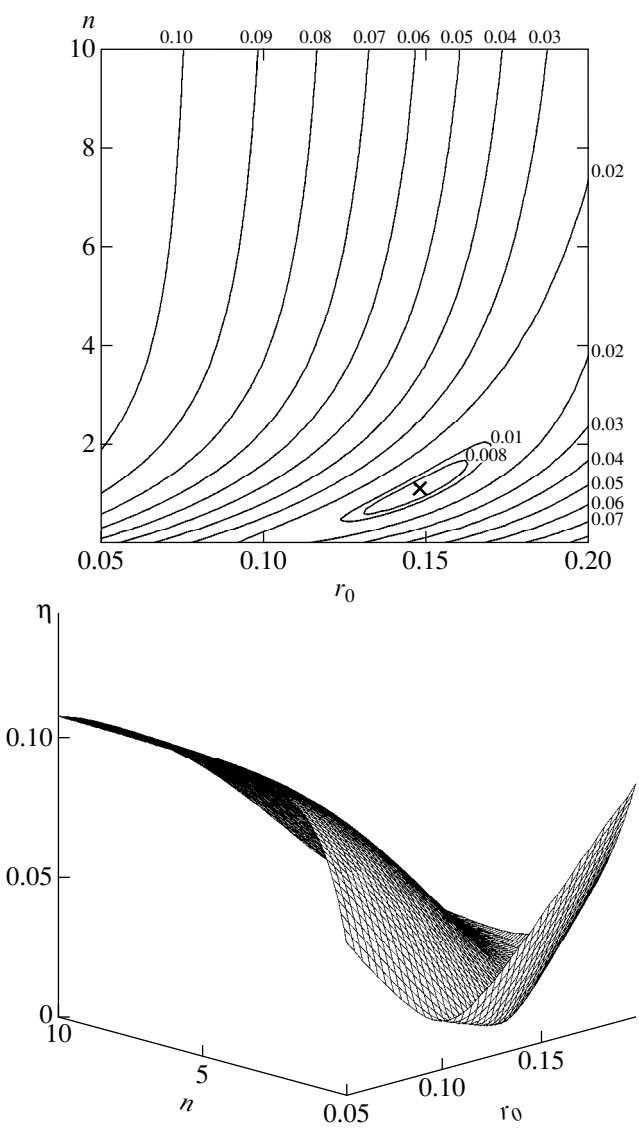

Fig. 2. Same as Fig. 1 for model 1 with the power law.

tion $\tau(r_0) = 1$. As a result, the decrease of $\alpha(r > r(\text{He III}))$ given by (4) is not a factor of two (in proportion to the electron density), but much smaller. This quantity decreased by ~30% in our estimative computations. As a result, the effect of this decrease on the function $1 - e^{-\tau(\xi)}$—a break at $r = r(\text{He III})$—is barely noticeable. We therefore performed all the main computations assuming that the entire atmosphere of the WN5 star consists of the He III ionization state.

It is evident from the above formulas that parameter r_c affects the model only when the Lamers $v(r)$ law is used. We show below that this parameter correlates strongly with β. We therefore fixed r_c at 0.05 (~$2R_\odot$), which is a reasonable estimate for the hydrostatic core radius of a WN5 star with a mass of ~ $9.3M_\odot$ [16]. Thus, the free parameters of the model are β (or n) and r_0.

In the general case, the expressions in (3) and (6) cannot be integrated analytically, because the function $v(r)$ can, strictly speaking, have an arbitrary form. In particular, analytical integration is impossible in the cases of a Lamers law and power-law relations with irrational exponents n. Then, the integral must be computed numerically. Since the integrand has a singularity at the integration limit, we used the Hermitian integration formula [17]. We performed our computations iteratively until we reached the required precision.

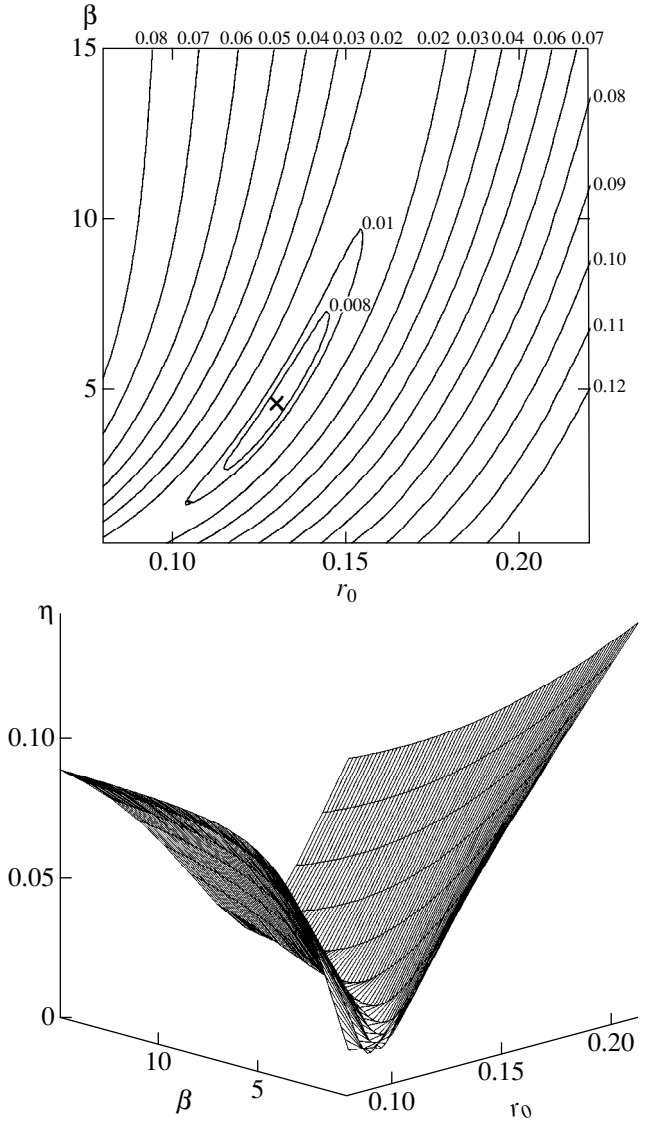

Fig. 3. Same as Fig. 1 for model 2 (i = 78°.0, r_{O6} = 0.25, $L_{WN5}/(L_{WN5} + L_{O6})$ = 0.20) with the Lamers law.

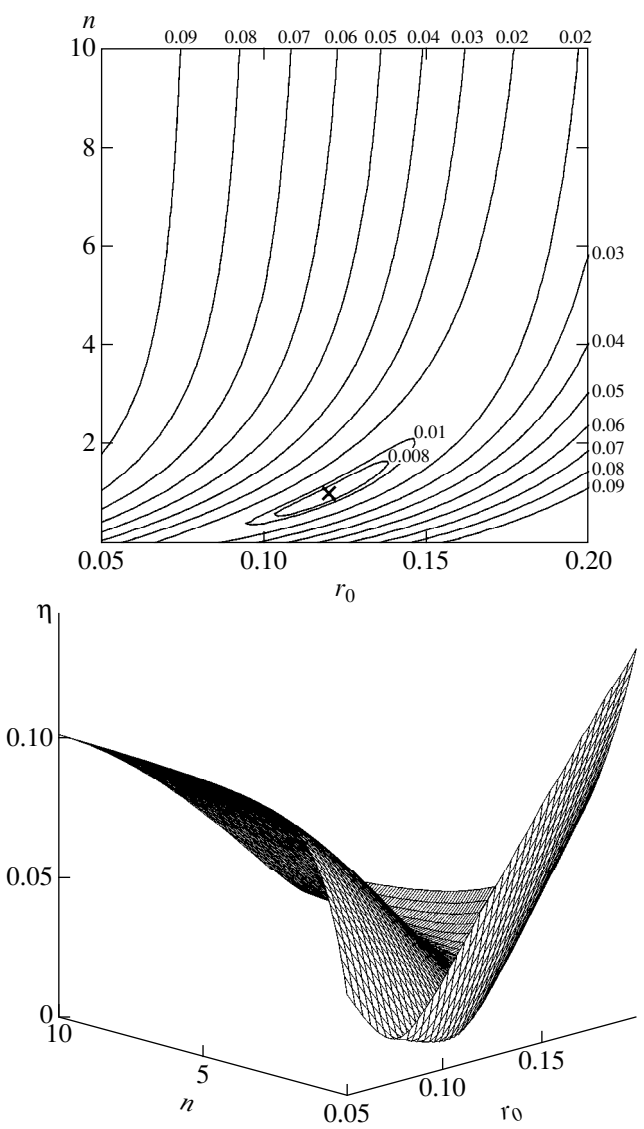

Fig. 4. Same as Fig. 1 for model 2 with the power law.

After the parametric problem is solved, we can estimate the absolute value of the WR star's mass-loss rate using the relations

$$n_e(r) = \frac{\alpha(r)}{\sigma_T},$$

where $\sigma_T \simeq 7 \times 10^{-25}$ cm^2 is the Thomson scattering cross section, and

$$\rho(r) = 2m_p n_e(r),$$

where $m_p = 1.7 \times 10^{-24}$ g is the proton mass (as noted above, we assume that the medium consists exclusively of fully ionized helium):

$$\dot{M}_{WR} = 4\pi r^2 v(r)\rho(r).$$

Here, $n_e(r)$ and $\rho(r)$ are the radial electron and total density profiles, respectively, and $\dot{M}_{WR}$ is the absolute value of the mass-loss rate of the WR star. The mass-loss rate $\dot{M}_{WR}$ can be computed using any distance r and the corresponding expansion velocity, e.g., r_0 and v_0.

4. RESULTS AND DISCUSSION

4.1. Rectified λ4244 Å Light Curve

Figures 1 and 2 show the residual surfaces for model 1 for the Lamers and power-law outflow velocity profiles $v(r)$, respectively. Figures 3 and 4 show the corresponding surfaces for model 2.

The minimum-residual solutions are summarized in the table. The fifth column gives the reduced χ^2 for the

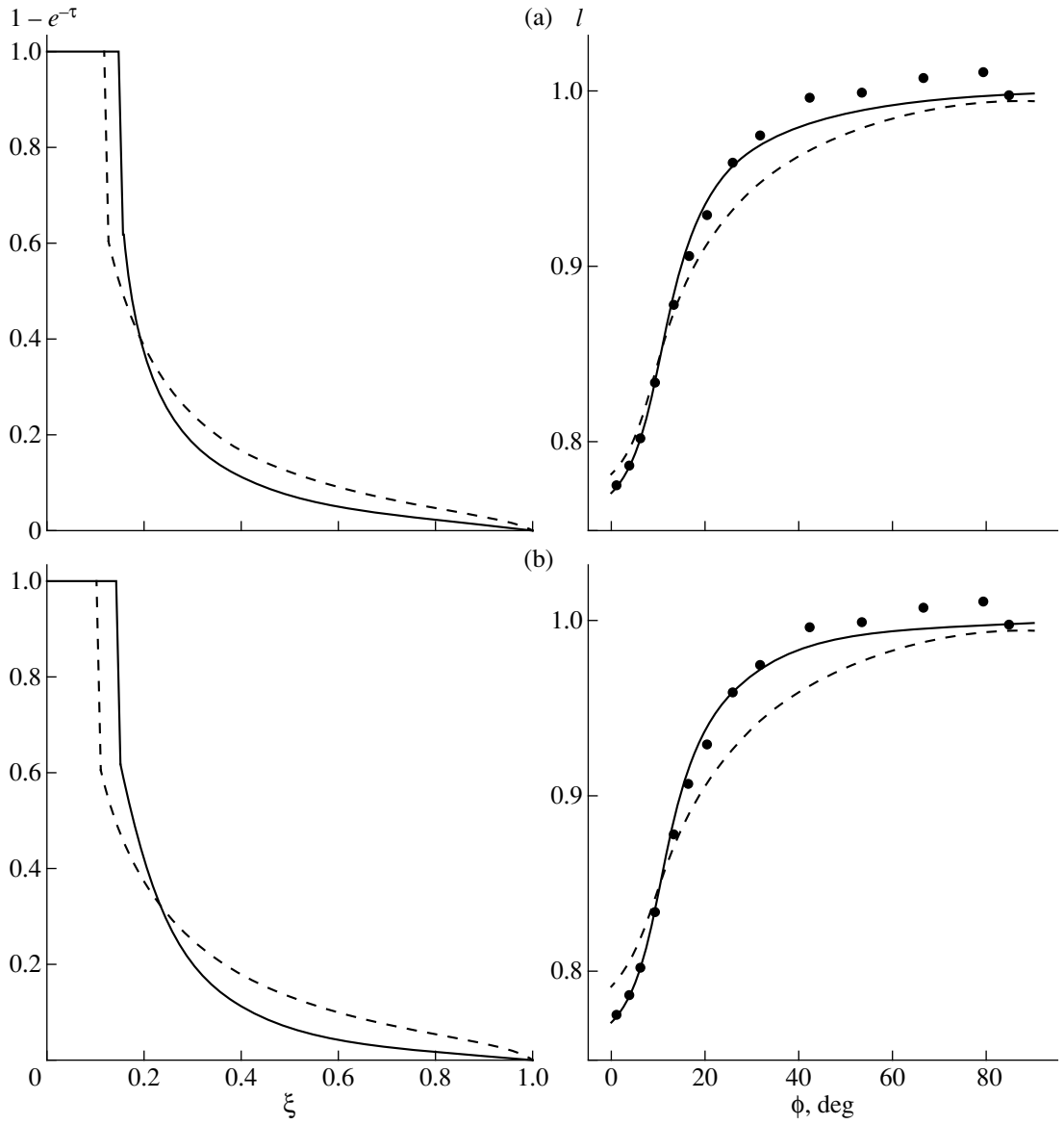

Fig. 5. The functions $1 - e^{-\tau(\xi)}$ and model light curves for the best-fit parameters for model 1: (a) Lamers law and (b) power law. For comparison, the dashed curves show the best-fit light curves for $\beta = 1$ and $n = 0$. Here and in all subsequent figures, the points represent the observational data.

given model and the sixth column the corresponding significance level in percent. The table also gives the estimated mass-loss rate for the WN5 component. To compute this, we must know the absolute velocity at a given point in the stellar wind (e.g., at a distance r_0). The velocities V_0 for the Lamers models were computed for the adopted $V_\infty = 1800$ km/s. For the power-law models, V_0 cannot be inferred from the model itself, and we therefore fixed it at 200 km/s, which approximately corresponds to the case of the Lamers model. Figures 5 and 6 show the corresponding model light curves (and functions $1 - e^{-\tau(\xi)}$).

It is evident from Figs. 5 and 6 and the table that none of the new solutions can compare with the earlier solution of [6, 8] in terms of the residual ($\eta \sim 0.004$). The obvious reason for this is that the parametric model we have used here is less flexible than that adopted in [6, 8]. However, the solutions for the power-law models have χ^2 values that are acceptable at the 1–2% significance levels. It is important to identify the origins of systematic discrepancies of the new model light curves from those obtained in [6, 8]. To this end, we show in Fig. 7 the solution for the same light curve of V444 Cyg from [8] obtained using model 1 on the class of convexo-concave functions.

The origin of the higher residual for the current model becomes evident from a comparison of Figs. 5a, 6a and Fig. 7: when $\xi > 0.8$, absorption is virtually

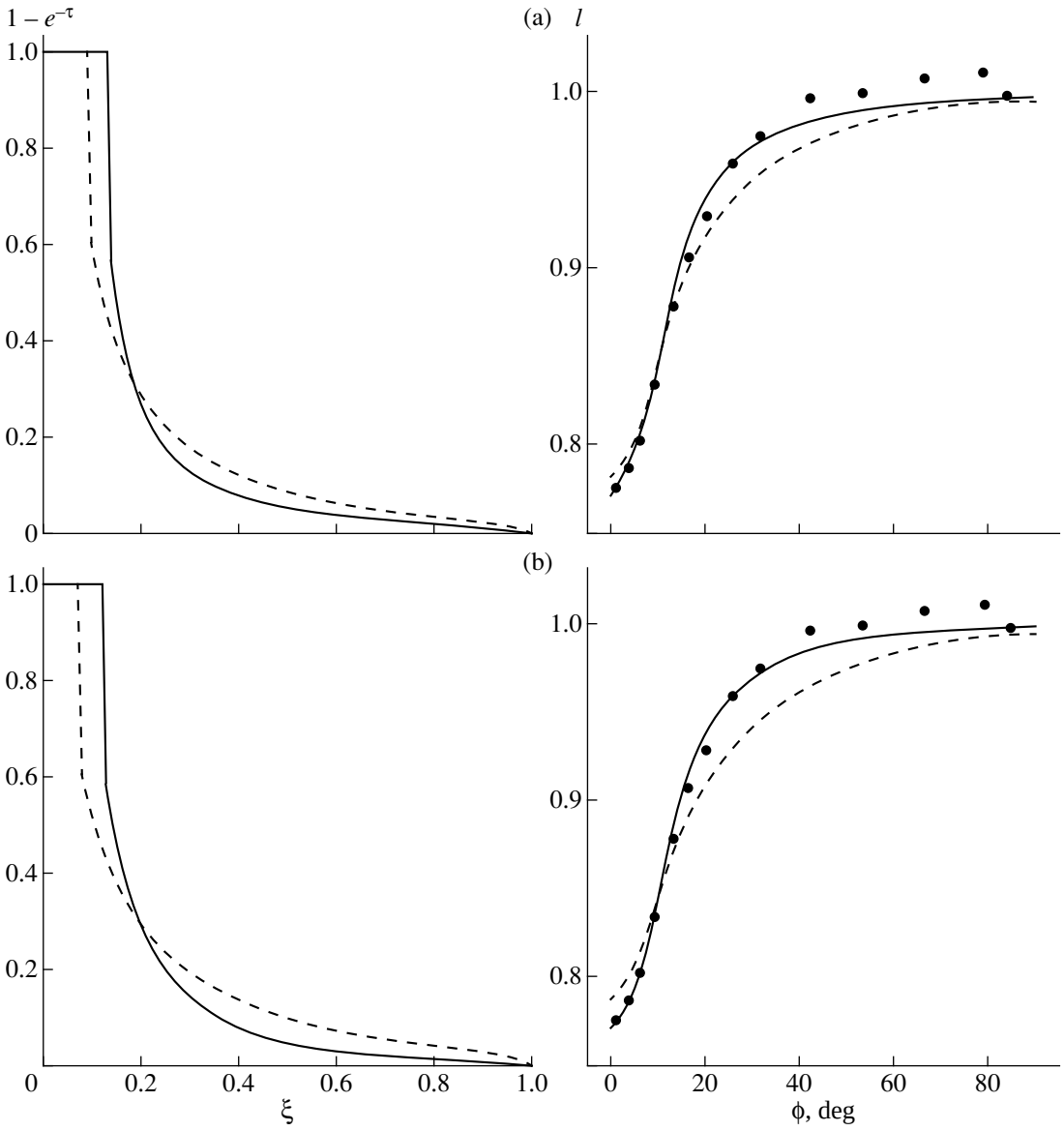

Fig. 6. Same as Fig. 5 for model 2.

absent in the models of [6, 8], whereas it is significantly different from zero in our current model. Therefore, in the current model, there is considerable absorption even at orbital phases far from the eclipse center, resulting in an increased loss of light at these phases (Figs. 5a and 6a) and, consequently, in a higher residual. Thus, this result shows that the Lamers law is not a very good approximation to the real velocity field in the stellar wind of the WR star.

Hamann and Schwarz [18] performed a joint analysis of the light curves and optical spectra of V444 Cyg in the framework of a so-called "standard" WR model atmosphere. They asserted that the observed light curve could be described by various combinations of model parameters. They used a Lamers law with $\beta = 1$. Setting aside other discrepancies between this model and the observational data for the binary system (see, e.g., [19]), we note that Hamann and Schwarz [18] compared only the widths and depths of the minima of the model and observed light curves. The quality of the fit was estimated visually without applying objective statistical criteria. It can easily be seen from a comparison of Fig. 13 in [18] and our Figs. 5 and 6 that the model suggested in [18] would be rejected as having a χ^2 that has a very low significance level.

The best-fit parameter values derived using our current models require a separate discussion. For example, the so-called "standard" model for the wind of an WR star (see, e.g., [20]) is based on a Lamers law with $\beta = 1$. How could we derive a higher β for our Lamers-law models? An analysis of model light curves for various

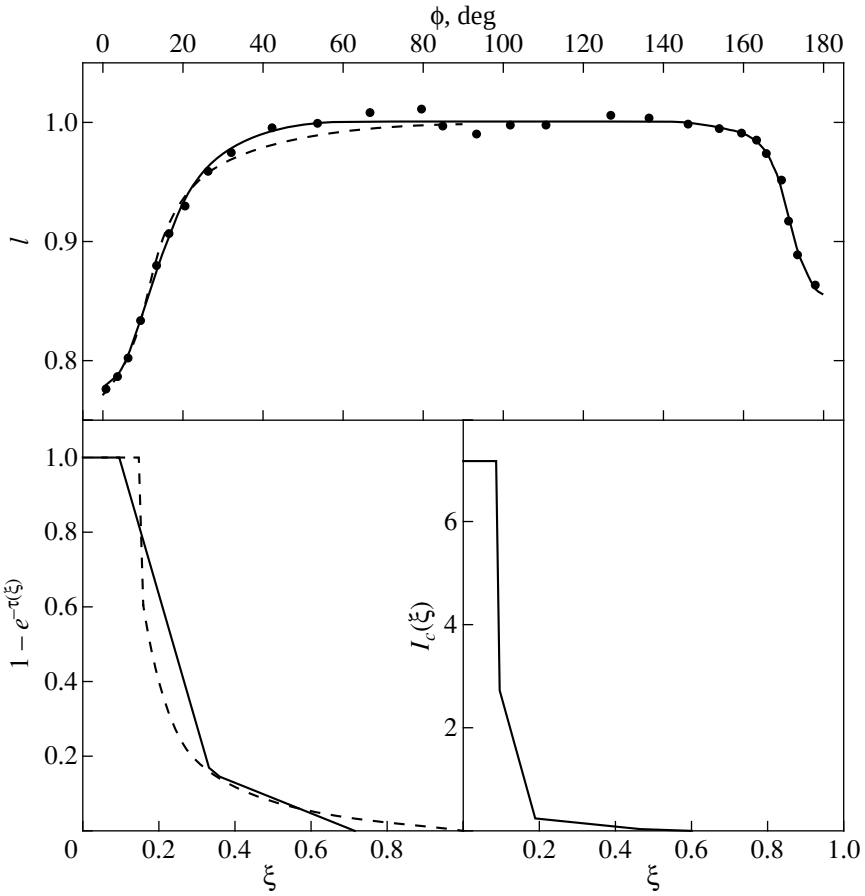

Fig. 7. Solution for model 1 on the class of convexo-concave functions [8] assuming that the relative luminosity of the WN5 component is equal to 0.38. The solid curve corresponds to $I_c(\xi)$—the brightness distribution across the disk of the WN5 star derived from analysis of the secondary minimum—and the dashed curve to the solution obtained in this paper for model 1 with the Lamers law.

combinations of parameters r_0 and β leads us to the following conclusions.

(1) It is obvious that the depth of the primary minimum depends on both I_0 and the behavior of the function $1 - e^{-\tau(\xi)}$ [see (2)]. Since I_0 was derived from the ratio of the depths of the minima and is fixed in this paper, r_0—the radius of the opaque core of the WN5 star—becomes the main factor determining the depth of the minimum. If exponent β is fixed, small and large r_0 values yield model light curves in which the depth of the minimum is either too small or too large, respectively, increasing the residual (Figs. 1 and 3).

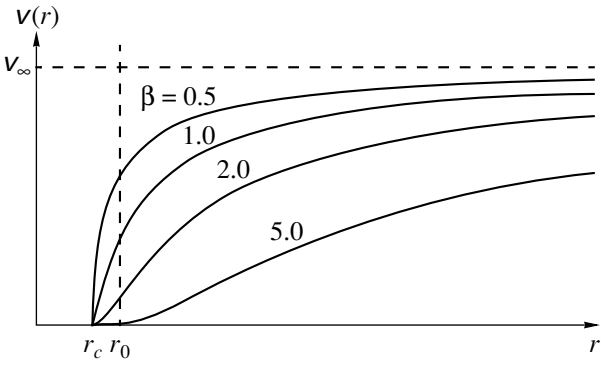

Fig. 8. The Lamers law for various β.

(2) The value of β primarily affects the steepness and extent of the function $1 - e^{-\tau(\xi)}$ at $\xi > r_0$ and, consequently, the shape of the primary minimum. Figure 8 shows the functions $v(r)$ for the Lamers-law models with various β. It is evident from this figure and (4) that $\alpha(r)$—and, consequently, $1 - e^{-\tau(\xi)}$ as well—decrease faster the higher β is, since the "drop" in $v(r)$ at a given distance interval increases with β. At small β, $v(r)$ varies only slightly in the interval $r_0 - \infty$, so that the $\alpha(r)$ fall-off is determined primarily by the r^{-2} factor. Moreover, the line-of-sight absorption exhibits an appreciable "tail" at large distances from the center of the WR star, which increases the loss of light in the wings of the model light curve and, consequently, increases the residual. If β is very high, the WN5 star photosphere becomes almost transparent (because $\alpha(r)$ falls off steeply due to

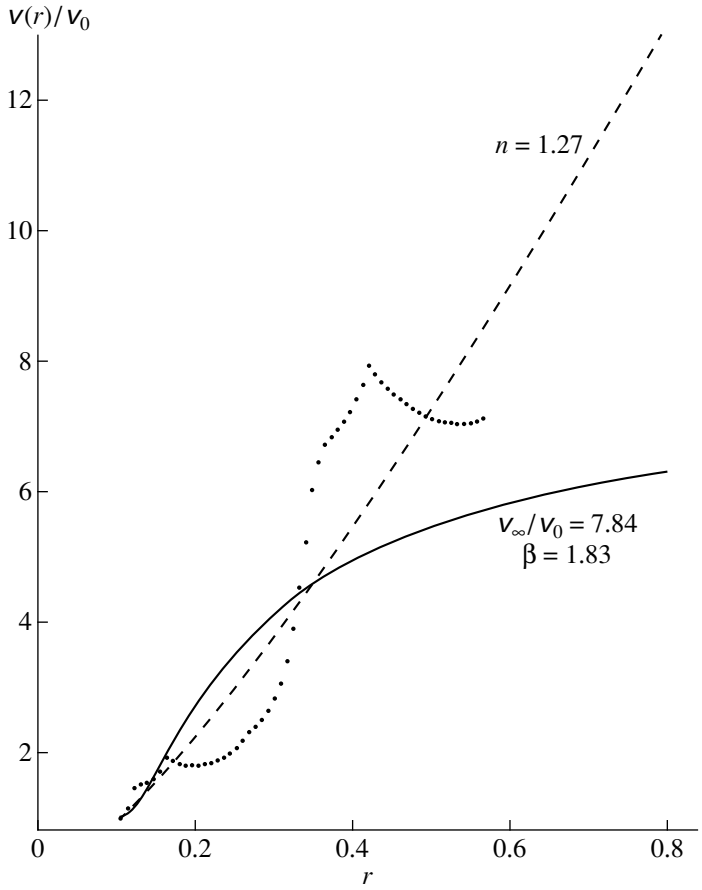

Fig. 9. Reconstructed velocity distribution $v(r)$ (dotted) and its approximation by the Lamers law (solid) and the power law (dashed) from [8] (solution on the class of concavo-convex functions, relative luminosity of the WN5 star equal to 0.38).

the large change in $v(r)$ in the interval $r_0 - \infty$), and the model light-curve minimum becomes too narrow, further increasing the residual (see Figs. 1 and 3). The residual takes its minimum at an intermediate β somewhat exceeding unity.

Thus, a small residual cannot be achieved when $\beta \leq 1$: in this case, there is always an appreciable "tail" of the function $1 - e^{-\tau(\xi)}$, leading to an increase in the residual in the wings of the light-curve minimum. However, the "tails" are present even for the best-fit β values we have obtained, suggesting that this model has a low significance level and should be rejected.

The above results lead us to a very important conclusion about the significance of the "peculiar" behavior of $v(r)$ discovered in [6, 8]: the acceleration in the WN5 star photosphere does not decrease with distance from the star, as it should for a Lamers law, and remains nearly constant or even increases somewhat with distance (Fig. 9). We initially treated this result with caution, since it was obtained by solving two ill-posed problems in succession. However, our current analysis proves that this result is significant. Small values $\beta \sim 1$ (implying rapid decrease in the acceleration) are rejected simply because they yield model eclipses that are substantially broader than those observed. Since this solution is essentially based only on the width of the primary minimum, it can considered to have a firm basis.

The fact that power-law models fit the observed light curve better further supports this result. The power-law models yield stronger acceleration at large distances from the center of the WN5 star compared to the Lamers law. It is noteworthy that the exponents n derived here for the power-law $v(r)$ models are close to those obtained in [6, 8] for a power-law approximation of the reconstructed $v(r)$ field.

Other studies (see, e.g., [3–5]) have also reported evidence suggesting that the stellar wind of the WR star might be accelerated more uniformly (with higher β) than in the standard model. This conclusion has great importance for our understanding of the acceleration mechanism in the stellar winds of WR stars.

4.2. Stability of the Solution to the Rectification Procedure and Choice of the Hydrostatic Core Radius of the WN5 Star

It is important to test whether rectification of the light curve (i.e., correction for component ellipticity and mutual heating) affects the solution of the inverse parametric problem. To this end, we repeated our

Best-fit model parameters

Model	r_0	β or n	Error η_1	χ_0^2	$P(\chi^2 > \chi_0^2)$, %	V_0, km/s	$\dot{M}$, 10^{-6} ($M_\odot$/yr)
1. Lamers law	0.155	5.4	0.0065	3.08	0.02	220	5.5
2. Lamers law	0.130	4.6	0.0063	2.89	0.05	193	4.2
1. Power law	0.148	1.1	0.0054	2.13	1.2	200	4.1
2. Power law	0.120	1.0	0.0053	2.05	1.7	200	3.2

Remarks: corresponds to (1) $i = 78.^\circ 43$, $r_{O6} = 0.20$, $L_{WN5}/(L_{WN5} + L_{O6}) = 0.38$ and (2) to $i = 78.^\circ 0$, $r_{O6} = 0.25$, $L_{WN5}/(L_{WN5} + L_{O6}) = 0.20$. V_0 for the Lamers models corresponds to the adopted $V_\infty = 1800$ km/s. V_0 for the power-law models is equal to the adopted value.

computations for model 1 with the Lamers law using the nonrectified λ4244 Å light curve. These computations yielded the model parameters $r_0 = 0.155$, $\beta = 4.3$, $\eta = 0.0059$, $\chi_0^2 = 2.56$, and $P(\chi^2 > \chi_0^2) = 0.2\%$. The corresponding theoretical and observed light curves are compared in Fig. 10a. It is evident that our previous result for the rectified light curve is insensitive to the adopted rectification procedure.

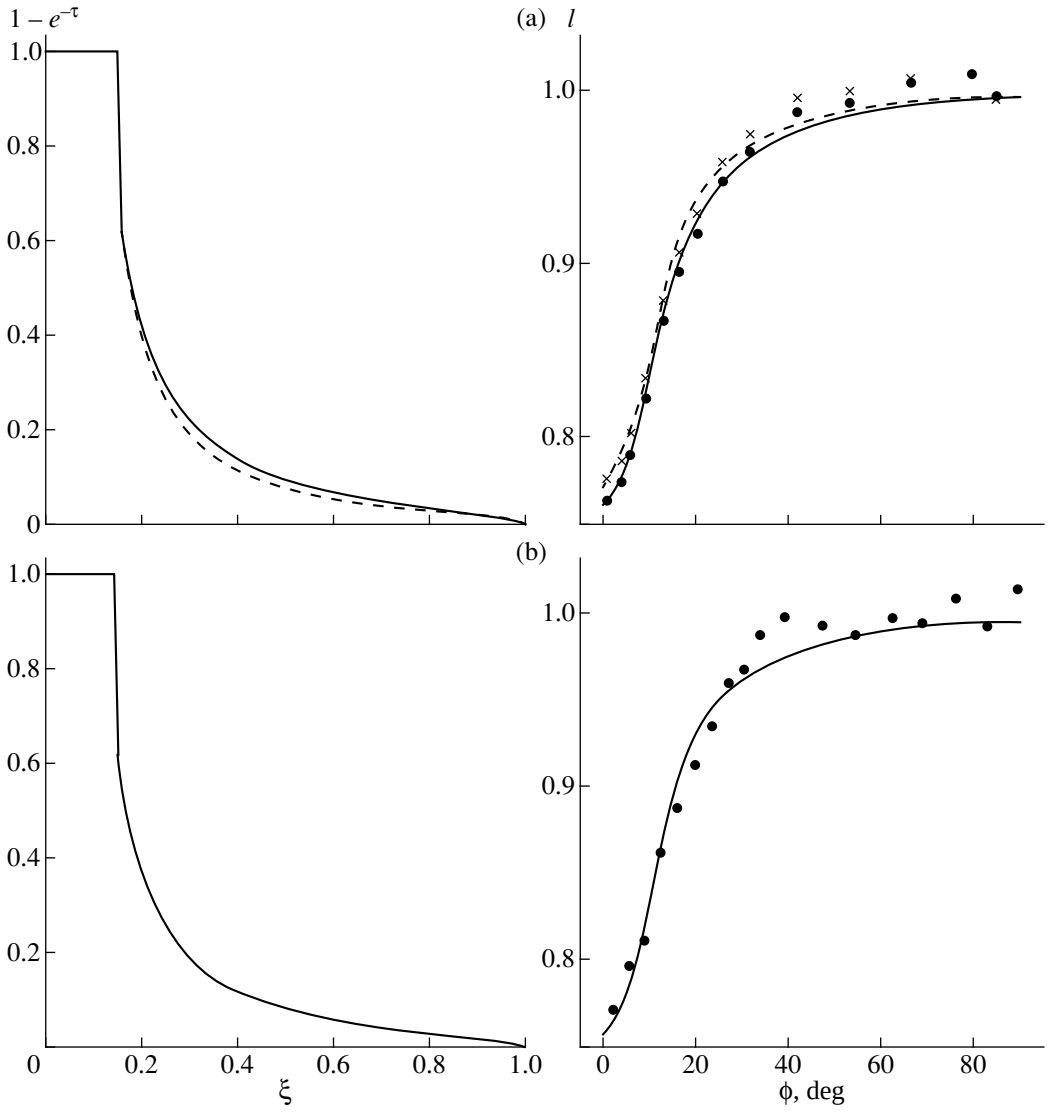

Fig. 10. Functions $1 - e^{-\tau(\xi)}$ and model light curves for the best-fit parameters for model 1 with a Lamers law: (a) nonrectified λ4244 Å light curve (for comparison, the dashed curves and crosses show the best-fit solution for the rectified light curve from Fig. 5 and the observed rectified light curve, respectively) and (b) rectified λ4789 Å light curve. See text for solution parameters.

As noted in Section 3, r_c correlates strongly with β if a Lamers law is used. This follows directly from the above discussion (see also Fig. 8). For instance, decreasing r_c (with fixed r_0 and β) reduces the range of $v(r)$ for $r > r_0$, and the same effect can be achieved by fixing r_c and r_0 and decreasing β. Thus, to compensate for a decrease in r_c, we must increase β, and vice versa. Of course, as follows from (1), this compensation is not absolute. To illustrate the nature of the correlation, we repeated the computations for model 1 using the Lamers law and fixed $r_c = 0.02$ and $r_c = 0.15$ (recall that, in our main series of computations, we adopted $r_c = 0.05$ or $\sim 2R_\odot$). The best-fit model parameters for $r_c = 0.02$ ($\sim 0.8R_\odot$) are $r_0 = 0.150$ and $\beta = 13.6$, with $\eta = 0.0066$, $\chi_0^2 = 3.18$, and $P(\chi^2 > \chi_0^2) = 0.015\%$. For $r_c = 0.15$ ($\sim 5.7R_\odot$), we have $r_0 = 0.165$ and $\beta = 0.95$, with $\eta = 0.0072$, $\chi_0^2 = 3.78$, and $P(\chi^2 > \chi_0^2) = 0.0009\%$. It is clear from this analysis that the residual depends only weakly on the adopted value of r_c. Note that these models use extremely low and high r_c. If more realistic intermediate values were adopted, it would be impossible to distinguish between various combinations of r_c and β. We therefore consider it justified to fix r_c at a value consistent with modern concepts about the hydrostatic radii of WR stars.

It follows from this discussion that the best-fit β decreases with r_c. However, it would be a mistake to say that the acceleration in the stellar winds of WR stars could be described by small β values if we adopt sufficiently large hydrostatic stellar radii. The last computed model has a much higher residual than the basic models, and can be rejected as having a low significance level.

4.3. The λ4789 Å Light Curve

We also verified the stability of our results to changes in the observed light curve. Solving the inverse problem (i.e., interpreting the rectified λ4789 Å continuum light curve) in terms of model 1 using a Lamers parametric law and $r_c = 0.05$ yielded results that were very similar to those for the previous analysis: $r_0 = 0.145$, $\beta = 4.2$, $\eta = 0.0101$, $\chi_0^2 = 1.79$, $P(\chi^2 > \chi_0^2) = 2.6\%$ (in the vicinity of the primary minimum, the λ4789 Å light curve is accurate to about 0.008 in intensity units), $V_0 = 298$ km/s, and $\dot{M} = 6.6 \times 10^{-6} M_\odot$/yr. The corresponding observed and theoretical light curves are shown in Fig. 10b.

5. CONCLUSIONS

Let us now discuss the technique we used to solve the inverse problem of interpreting the continuum light curve of V444 Cyg. Because of the ill-posed nature of this inverse problem, some physically justified *a priori* information about the unknown functions $I_c(\xi)$ and $1 - e^{-\tau(\xi)}$ must be used to identify an appropriate compact set of functions. In our previous papers [6, 8, 13], we solved this inverse problem using the following types of *a priori* information:

(1) $I_c(\xi)$ and $1 - e^{-\tau(\xi)}$ are monotonic and nonnegative;

(2) $I_c(\xi)$ is monotonic and $1 - e^{-\tau(\xi)}$ is concave, both functions are nonnegative;

(3) $I_c(\xi)$ and $1 - e^{-\tau(\xi)}$ are convexo-concave and nonnegative.

Moving from (1) to (3) is equivalent to gradually reducing the compact set of functions by invoking increasingly specific *a priori* information about the nature of the WR star. It is noteworthy that the resulting geometric parameters r_{O6} and i are virtually the same in all cases: with the observed relative luminosity of the WN5 star fixed at $L_{WN5}/(L_{WN5} + L_{O6}) = 0.38$, we always have $r_{O6} \simeq 0.20$ and $i \simeq 78.4$, whereas the solution corresponding to the absolute minimum of the residual always yields $r_{O6} \simeq 0.25$, $i \simeq 78.0$, and $L_{WN5} = 0.20$. The discrepancy between the solutions corresponding to fixed observed luminosity and minimum residual is due either to systematic departures of our light curve from that for an ideal binary system (collisions of the stellar winds of the two component stars, etc.) or to errors in the spectrophotometrically estimated component luminosity ratio in V444 Cyg.

We emphasize, however, that a spherical model for the WN5 stellar wind emitting and absorbing light in the continuum has found a sound basis in recent spectropolarimetric observations of the V444 Cyg system [21]. Note also that the models based on *a priori* information (1)–(3) are in all cases consistent with the observations: they fit the observed light curve within the observational errors.

In the current paper, we further reduced the compact set of functions by using a two-parametric approximation for the velocity field $v(r)$ in the stellar wind of the WN5 star. Since the geometric parameters r_{O6} and i had been determined earlier using various types of *a priori* information (1)–(3), we solved the parametric problem with these parameters fixed at their best-fit values. The results show the parametric model to be inconsistent with the observed light curve: the Lamers-law model law can be rejected at a significance level of 0.02–0.05%, and the power-law model can be rejected at a significance level of 1.2–1.7% (see table). Varying the hydrostatic core radius of the WN5 star, substituting the nonrectified for the rectified λ4244 Å light curve, and solving the inverse problem for the λ4789 Å light curve demonstrated that the significance level for the rejection of the parametric models changed only slightly, and remained very low. This means that rejecting the parametric model is very unlikely to represent an error of the first kind, i.e., rejecting the correct model.

This strongly suggests that the departures of the empirical $v(r)$ law reconstructed in [6, 8] from a Lamers law are real, and not due to errors introduced by solving two ill-posed problems in succession. This leads us to conclude that the stellar wind of the WN5 star continues to accelerate at rather large distances from the star's core. In terms

of a Lamers law (rejected by our model but still widely used *de facto*), this means that $\beta > 1$.

Recently, Hillier and Miller [22] and Lépine *et al.* [23] suggested an alternative model to describe variations in the velocity of matter in the atmospheres of WR stars:

$$v(r) = V_0 + (V_\infty - V_{\rm ext} - V_0)(1 - r_c/r)^{\beta_1} + V_{\rm ext}(1 - r_c/r)^{\beta_2}.$$

This combination of two Lamers laws make it possible for the wind acceleration to differ at large distances from the star. The parameter $V_{\rm ext}$ controls the relative importance of the β_1 and β_2 terms. When $V_{\rm ext}$ is small, acceleration occurs mainly in the vicinity of the WR-star core, whereas it occurs at greater distances when $V_{\rm ext}$ is large. Lépine *et al.* [23] adopted $\beta_1 = 1$ and $\beta_2 = 10$ for the WR135 star (HD 192103, WC8) and obtained the best-fit value $V_{\rm ext} = 900$ km/s for $r_c = 2R_\odot$ ($V_\infty = 1400$ km/s for this star).

We did not try to apply this law to our model, because it would increase the number of free parameters to five (assuming that V_∞ is known and adopting a fixed r_c). It is evident that this new form of the $v(r)$ law is constructed so as to increase the acceleration at large distances from the WR star, as suggested by our current analysis. In this case, the model is likely to fit the observed light curve satisfactorily; however, this can by no means be interpreted as proof of its correctness. The aim of our current work was to see whether the standard Lamers law could satisfactorily describe the observed light curves, and the answer turned out to be negative. In our opinion, the best solution to the $v(r)$ problem will include construction of a self-consistent gas-dynamical model for mass motions in the stellar wind.

We note in conclusion that the mass-loss rates $\dot{M}$ of the WN5 star that we determined independently from the λ4244 Å light curve (see table) are close to the value $\dot{M} \simeq 7 \times 10^{-6} M_\odot$/yr derived from the increase in the orbital period of V444 Cyg [24–26] and from polarization variations [27]. The somewhat lower $\dot{M}$ values we have obtained here could be due to the fact that the parametric laws we adopted for $v(r)$ do not adequately describe the observed light curve of V444 Cyg.

ACKNOWLEDGMENTS

This work was supported by the Russian Foundation for Basic Research (project code 99-02-17589) and the Council for the Support of Leading Science Schools in Russia (grant 00-15-96553).

REFERENCES

1. K. G. Gayley, S. P. Owocki, and S. R. Cranmer, Astrophys. J. **442**, 296 (1995).
2. H. J. G. L. M. Lamers and J. P. Cassinelli, *Introduction to Stellar Winds* (Cambridge Univ. Press, Cambridge, 1999), p. 9.
3. G. Koenigsberger, Astron. Astrophys. **235**, 282 (1990).
4. A. F. J. Moffat, in *Proceedings of the 33rd Liège International Astrophysical Colloquium on Wolf–Rayet Stars in the Framework of Stellar Evolution*, Ed. by J.-M. Vreux *et al.* (Liège, 1996), p. 199.
5. S. Lepine and A. F. J. Moffat, Astrophys. J. **514**, 909 (1999).
6. I. I. Antokhin, A. M. Cherepashchuk, and A. G. Yagola, Astrophys. Space Sci. **254**, 111 (1997).
7. A. M. Cherepashchuk, in *Thermal and Ionization Aspects of Flows from Hot Stars: Observations and Theory*, Ed. by H. J. G. L. M. Lamers and A. Sapar (Astronomical Society of the Pacific, San Francisco, 2000); Astron. Soc. Pac. Conf. Ser. **204**, 249 (2000).
8. I. I. Antokhin and A. M. Cherepashchuk, Astron. Zh. **78**(5) (2001).
9. A. V. Goncharskiĭ, A. M. Cherepashchuk, and A. G. Yagola, *Numerical Methods for Solution of Inverse Problems in Astrophysics* [in Russian] (Nauka, Moscow, 1978), p. 186.
10. A. V. Goncharskiĭ, S. Yu. Romanov, and A. M. Cherepashchuk, *Finite-Parameter Inverse Problems in Astrophysics* [in Russian] (Mosk. Gos. Univ., Moscow, 1991), p. 3.
11. A. N. Tikhonov, Dokl. Akad. Nauk SSSR **39**, 195 (1943).
12. A. M. Cherepashchuk, Astron. Zh. **43**, 517 (1966) [Sov. Astron. **10**, 411 (1966)].
13. A. M. Cherepashchuk, Sov. Astron. **9**, 725 (1975).
14. A. M. Cherepashchuk, G. Koenigsberger, S. V. Marchenko, and A. F. J. Moffat, Astron. Astrophys. **293**, 142 (1995).
15. A. A. Rubashevskiĭ, Astron. Zh. **67**, 860 (1990) [Sov. Astron. **34**, 433 (1990)].
16. N. Langer, Astron. Astrophys. **252**, 669 (1991).
17. N. N. Kalitkin, *Numerical Methods* [in Russian] (Nauka, Moscow, 1978), p. 107.
18. W.-R. Hamann and E. Schwarz, Astron. Astrophys. **261**, 523 (1992).
19. A. M. Cherepashchuk, Astrophys. Space Sci. **221**, 227 (1994).
20. W.-R. Hamann, *Wolf–Rayet Stars: Binaries, Colliding Winds, Evolution (IAU Symposium 163)*, Ed. by K. A. van der Hucht and P. M. Williams (Kluwer, Dordrecht, 1996), p. 105.
21. T. J. Harries, D. J. Hillier, and I. D. Howarth, Mon. Not. R. Astron. Soc. **296**, 1072 (1998).
22. D. J. Hillier and D. L. Miller, Astrophys. J. **519**, 354 (1999).
23. S. Lépine *et al.*, Astrophys. J. (2000) accepted.
24. A. M. Cherepashchuk, *Wolf–Rayet Stars: Binaries, Colliding Winds, Evolution (IAU Symposium 163)*, Ed. by K. A. van der Hucht and P. M. Williams (Kluwer, Dordrecht, 1996), p. 262.
25. Kh. F. Khaliullin, Astron. Zh. **57**, 195 (1974).
26. I. I. Antokhin, S. V. Marchenko, and A. F. J. Moffat, in *Wolf–Rayet Stars: Binaries, Colliding Winds, Evolution (IAU Symposium 163)*, Ed. by K. A. van der Hucht and P. M. Williams (Kluwer, Dordrecht, 1994), p. 520.
27. N. St-Louis, A. F. J. Moffat, L. Lapointe, *et al.*, Astrophys. J. **410**, 342 (1993).

Translated by A. Dambis

Astronomy Reports, Vol. 45, No. 4, 2001, pp. 281–286. Translated from Astronomicheskiĭ Zhurnal, Vol. 78, No. 4, 2001, pp. 327–332.

Dust Formation in Binaries with OB and WR Components in a Two-Phase Stellar-Wind Model

O. V. Aleksandrova and K. V. Bychkov

Sternberg Astronomical Institute, Universitetskiĭ pr. 13, Moscow, 119899 Russia

Received April 24, 2000

Abstract—We describe the formation of carbon dust in binary systems with hot components as a result of the collisions of clouds in a two-phase stellar-wind model. Calculations are made for the well studied system WR 140. The collisions lead to the formation of composite clouds and shock waves, with the temperature at the shock front equal to about 3×10^8 K along both sides of the interface boundary. During isobaric deexcitation to $(0.5–0.7) \times 10^4$ K, the cloud density increases by a factor of several thousand; its thickness in the direction of the shock decreases by the same factor. After deexcitation, the hydrogen inside the composite cloud is in its atomic state, while the carbon remains ionized. The deexcitation is followed by expansion of the cloud, which moves away from both stars. During the first 10^6 s, its thickness remains relatively small, so that the expansion is one-dimensional. The radiation field inside the cloud decays, resulting in the recombination of the carbon. Further expansion of the cloud leads to adiabatic cooling, and the formation of dust particles becomes possible. After the dimensions of the cloud have become roughly the same in all directions, its expansion is isotropic, so that it becomes transparent within approximately 10^6 s, and the dust is heated to $(1.0–1.4) \times 10^3$ K, observed as an IR "flare." The time required for the cloud to move from the exciting star and heat the dust is comparable to the observed delay in the increased IR emission relative to the time of periastron. © *2001 MAIK "Nauka/Interperiodica".*

1. INTRODUCTION

Several binaries with OB and WC components emit IR radiation [1–7], which is usually associated with dust grains of amorphous carbon [5–11]. The estimated size of the particles is approximately several tenths of a micron [5, 12, 13], and their temperature is about 1000 K [10–12, 14]. The formation of dust is related to the wind from the WC component. Essentially all investigators have concluded that the condensation of dust particles occurs in a relatively dense, low-temperature gas, with the carbon in its atomic state. This conclusion leads to the main difficulty connected with dust formation. Due to the high temperatures in stellar atmospheres and the large velocity of stellar winds (of the order of 3000 km/s), these conditions cannot occur in winds from hot stars. In collisions of gas flows in the binaries considered here, the temperatures behind the shock front reach hundreds of millions of degrees. In addition, the gas in the wind is ionized and efficiently heated by the radiation from both stars. Consequently, efficient mechanisms for cooling the wind and protecting it from external radiation must be found.

It is usually thought that the temperature behind the shock front is decreased via deexcitation of the gas. However, in wide systems like WR 140 and WR 137, deexcitation does not occur in most of the wind, since the radiative-cooling timescale appreciably exceeds the dynamical timescale. At the same time, Usov [15] has pointed out that the gas outflow is decelerated in the vicinity of the frontal point. He suggested that a region forms where the dynamical timescale increases considerably, radiative energy losses become appreciable, and the gas can be cooled to temperatures of the order of 10^4 K. Neither cooling to 1000 K, which is required for dust formation, nor the problem of carbon recombination was taken into consideration in [15].

Based on data for the Wolf-Rayet-type carbon star WC 9, Cherchneff and Tielens [8] calculated chemical reactions leading to dust formation and concluded that the presence of dust cannot be understood in models with spherically symmetrical, homogeneous flows. They suggested that the wind from the WC star has two components: one is rather dense and consists of neutral matter concentrated in a plane (which they call an equatorial disk), while the other is spherical, has low density, and consists of ionized matter. Assuming that the mechanisms for dust formation are well understood and the rates of the corresponding reactions are known, Cherchneff and Tielens [8] concluded that the formation of dust requires densities three to four orders of magnitude higher than that of the rarified wind component.

Even earlier, Hackwell *et al.* [12] estimated the required density contrast to be $\sim 10^4$. They also concluded that clouds are formed in the wind from a WC star, where granule condensation occurs and dust grains grow to size a of 10^{-5} cm. Williams *et al.* [10] emphasize the important role of ionizing radiation, and conclude that carbon recombination is possible in dense areas of the wind that are remote from the exciting stars.

1063-7729/01/4504-0281$21.00

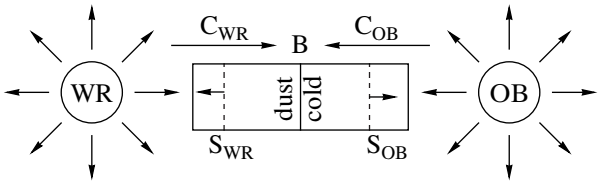

Region of dust formation in a collision of clouds.

In WR 140, the radiation peaks some time after periastron. The delay is around 50 days at 3.8 μm [16] and 90 days in the K band [7]. To explain this, Williams [7] suggested that the dust formation is triggered by a sharp increase in the gas density of the shock wave. The dust cannot form until the compressed matter is moved out to a distance where the gas cannot be heated by the radiation from the stars. The 90-day delay corresponds to a distance of 150 AU and a gas velocity of 2900 km/s.

In our study, we consider dust formation in a two-phase stellar-wind model [19], which we previously proposed to explain the X-ray radiation in the wide binary WR 140. In this model, the wind from each component consists of a rarified gas and dense, compact clouds. When clouds collide, deexcitation occurs behind the shock front, even in such wide systems as WR 140 and WR 137. The clouds rapidly move away from the hot stars, and processes inside them promote the formation of dust. We now turn to a description of these processes.

2. THE MODEL

The figure presents a schematic of a collision of clouds with subsequent deexcitation. The left and right circles display the WR and OB stars, respectively. The cloud C_{WR} ejected from the Wolf-Rayet star collides with a cloud C_{OB} from the OB star. As a result, a composite cloud forms, with the magnitude and direction of its velocity determined by the conservation of momentum for the inelastic collision. The long, horizontal, thick arrows indicate the velocity of the clouds before the collision. The vertical line B marks the boundary of the collision zone. Shock waves S_{WR} and S_{OB} propagate inside each cloud, marked by vertical dashed lines. The short, horizontal, thick arrows indicate the direction of the front velocity relative to each cloud. At each shock front, S_{WR} or S_{OB}, the temperature reaches hundreds of millions of degrees. We assume that both clouds undergo deexcitation; therefore, fairly cool and dense regions of neutral gas can form far from the shock front, near the interface boundary B. In the figure, these are marked "cold" in the cloud from the OB star and "dust" in the cloud from the WR star. Their high density is due to the fact that the temperature decrease occurs under nearly constant pressure.

We suppose that dust forms in the area labelled "dust." To this end, carbon must recombine and cool to roughly 1000 K. Both the lower ionization boundary and the temperature of the de-excited gas are determined by the radiation of the system's stellar components. Let us consider the protection of the carbon from the ionizing radiation of both stars.

3. IONIZATION STATE IN THE CLOUDS

In order to cool the gas to temperatures suitable for dust formation, the "dust" region must be screened from the ionizing radiation of both stellar components of the system. Behind the shock front, the ratio of the deexcitation and recombination rates depends on the instantaneous temperature of the gas T_g. Provided that 5×10^5 K $> T_g > 5 \times 10^3$ K, a cool layer of ionized gas is initially formed, and only afterwards is there recombination [20], which can be inhibited by the radiation of the stars.

We suppose that the OB star is shielded by the cool area C_{OB}, marked "cold" in figure, where a higher density has been preserved due to the relatively short time until the collision. The radiation from the secondary component is considerably less intense. The boundary of the wind collision area is a factor of roughly 5.3 closer to the OB than to the WR star, so that the radiation of the WR star is a factor of 28 more dilute. In addition, the luminosity of the OB star is about a factor of three higher [11]. Consequently, the WR star contributes only about 1% of the ionizing radiation. Its radiation can also impede less dense gas belonging to C_{WR}.

Let us now proceed to quantitative calculations. We first consider the ionization state of the hydrogen. If the hydrogen inside the cloud becomes essentially neutral, conditions favoring carbon recombination can develop there. Therefore, we take the gas temperature T_g in this area to be $T_H \approx 5 \times 10^3$ K. As we will see below, uncertainty in T_H does not affect our main conclusions. Let us denote the relative concentration of neutral hydrogen—i.e., the ratio $n(\mathrm{HI})/n(\mathrm{H})$—as y. At low T_H, we can neglect ionization by electron collisions, in which case the modified Saha formula [21] is valid

$$\frac{(1-y)^2}{y} = A\exp(-\tau), \qquad (1)$$

where τ is the optical depth for threshold photons and the factor A does not depend on τ:

$$A = p\frac{g_i}{g_a} w \sqrt{\frac{T_g}{T_*}} \frac{2(2\pi m k T_*)^{3/2}}{nh^3} \exp\left(-\frac{J}{kT_*}\right). \qquad (2)$$

Apart from T_g and the total density n in units of number of particles of a given chemical element, this relation contains the dilution coefficient w, temperature of the star T_*, and atomic parameters: the ionization potential J, fraction p of recombinations to the first level, and the atomic and ionic statistical weights g_i and g_a.

Let us estimate the ionization state of hydrogen at the cloud boundary facing the OB star. We adopted the required parameters from [11]: semimajor orbital axis a = 14.7 AU, eccentricity ε = 0.84, effective temperature and radius of the OB star T_{OB} = 44000 K and $R_{OB} = 12R_\odot$. The logarithms of the bolometric luminosities in solar units are 5.65 and 5.2 for the OB and WR stars, respectively. The effective temperature and radius are less certain for the WC component: in accordance with [17, 18], we take them to be 43000 K and $7R_\odot$. As noted above, the errors in the parameters of the WR star cannot qualitatively affect the results.

For the frontal point at periastron, the calculated distance from the OB star is $r_s = 5.54 \times 10^{12}$ cm, which corresponds to a dilution coefficient $w = 5.6 \times 10^{-3}$. For these parameters, the numerical value for A obtained from (2) is

$$A \approx 1.2 \times 10^{18}/n. \quad (3)$$

We determine the gas density n as follows. According to our two-phase wind model [19], it is reasonable to adopt $n \approx 10^{12}$ cm^{-3} for the unperturbed gas in the cloud. In the "cold" region, the density is, of course, substantially higher. After compression by a factor of four, isobaric deexcitation occurs at the shock front, at temperatures of order 3×10^8 K to 5000 K. As a result, the density can increase by roughly a factor of 2×10^5. This is, however, an upper limit, since, starting from some moment of time, the pressure of the de-exciting gas is determined by the magnetic field, and the density increase ceases. If the induction lines are parallel to the plane front, the magnetic pressure increases in proportion to the square of the density. For example, for an unperturbed field 10 Oe, the transition to an isochoric regime occurs when the temperature falls by roughly a factor of a thousand. In view of this, we adopt $n = 10^{15}$ cm^{-3}. This value of n corresponds to a very large right-hand side of (2), which essentially implies the total ionization of the hydrogen. This result remains valid for any reasonable density of the clouds.

Let us calculate the thickness of the layer inside which the hydrogen is in its neutral state. The optical depth increment is

$$d\tau = \tau_b y ds. \quad (4)$$

Here, s is the dimensionless distance from the boundary in units of the cloud thickness L. The parameter τ_b is the product

$$\tau_b = \sigma L n, \quad (5)$$

where σ is the threshold photoionization cross section. Simultaneous solution of (1) and (4) makes it possible to find an analytical expression for τ in the form of an implicit function s:

$$\tau_b s = \tau + \frac{A}{2}(1 - e^{-\tau}) + C - C_\tau - \ln\left(1 + \frac{A}{2} + C\right) + \ln\left(1 + \frac{A}{2}e^{-\tau} + C_\tau\right). \quad (6)$$

Here, we have introduced the notation

$$C = \sqrt{A + \frac{A^2}{4}},$$

$$C_\tau = Ae^{-\tau}\left(1 + \frac{A}{4}e^{-\tau}\right).$$

If τ is known, y can be derived from (1):

$$y = z - \sqrt{z^2 - 1},$$

$$z = \frac{A}{2}e^{-\tau} + 1.$$

In the case under consideration, when $\tau \gg 1$ and $A \gg 1$, formula (6) can be simplified. The first condition makes it possible to neglect C_τ compared to C, and also to neglect the last term on the right-hand side compared to the second-last term. Since $A \gg 1$, it follows that $C \approx A/2$ and $\ln\left(1 + \frac{A}{2} + C\right) \approx \ln A$. As a result, (6) reduces to

$$\tau_b s \approx A + \tau - \ln A.$$

Substituting (1) and solving the resulting quadratic equation, we express y as an explicit function of τ_0, A, and s:

$$y = 1 - \frac{1}{\frac{1}{2} + \sqrt{\frac{1}{4} + \frac{1}{G}}}, \quad (7)$$

where

$$G = \exp(A - \tau_b s).$$

The ionization state is determined by the parameter $q = A/(\tau_b s)$. When q is large, the hydrogen is strongly ionized:

$$y \approx \frac{1}{G},$$

while it is essentially neutral when q is small:

$$y \approx 1 - \sqrt{G}.$$

Here, we have taken into account the fact that G is large or small, respectively, together with q.

Let us now apply this result to clouds in real binary systems. Previously [19], we showed that deexcitation

can only occur in cloud collisions in which the running number of particles $\mathcal{N} = nL$ exceeds

$$\Omega \approx 7 \times 10^{22}\ \text{cm}^{-2}.$$

We can write

$$\mathcal{N} = j\Omega, \tag{8}$$

leaving the factor $j > 1$ a free parameter. It follows that $\tau_b \approx 4 \times 10^5 j$. According to (3), the density interval $14 < \log n < 16$ corresponds to the range of possible A values 100–10000. Thus, $q \ll 1$ in the de-excited clouds, and they contain a fairly extended area of neutral hydrogen. Clearly, this result is valid for any reasonable T_H. Thus, there are grounds to further consider the possible existence of regions of neutral carbon.

4. CARBON RECOMBINATION

Let us now analyze the ionization state of carbon. Since we are interested in the area in which dust can be formed, we take T_g to be equal to $T_\text{C} = 1000$ K. Such low temperature can hardly be reached via deexcitation, since the radiation cooling of dense ($n_e > 10^3$ cm^{-3}), semi-transparent gas is rather complex when $T < T_\text{H}$. However, after the shock passes through the entire cloud, the cloud begins to expand under the action of the pressure. The expansion is accompanied by adiabatic cooling, and the required temperature decrease occurs when the cloud size has doubled. We will see below that the specific value of T_g does not affect the result qualitatively, as was shown above for hydrogen.

According to our assumptions, the degree of hydrogen ionization in the region considered is so small that other chemical elements play the role of electron donors. To simplify the calculations, we will take into account only the contribution of carbon. Consequently, the product $n_\text{C} = Z_\text{C} n$ must be substituted into (2) instead of n, where $Z_\text{C} \approx 3 \times 10^{-4}$ is the relative abundance of carbon in units of the number of particles. The fact that we have excluded other chemical elements results in the underestimation of n_e. Therefore, we overestimate the degree of carbon ionization x_C in the region where it is small and where other elements play a significant role. This means that, if (1) and (2) yield a small x_C, in reality, it is even smaller. At $T_g = 1000$ K, the rates of dielectron recombination and electron collisional ionization are negligible. Note, however, that the spectrum of the radiation ionizing the carbon is no longer blackbody, due to absorption by hydrogen atoms located closer to the star. Strictly speaking, this limits the applicability of (1) and (2). However, the main contribution to the photoionization rate is made by threshold photons, which pass through hydrogen unobstructed. Therefore, the use of (1) and (2) is justified here. Substituting numerical values for various carbon parameters ($g_a = 9$, $g_i = 6$, $J = 11.26$ eV) and $n_\text{C} = 10^{15} \times 3 \times 10^{-4} = 3 \times 10^{11}$ cm^{-3} into (2), we obtain $A = 2.1 \times 10^6$. The threshold cross section for carbon photoionization is 1.2×10^{-17} cm^2 [22], implying $\tau_b = 2.5 \times 10^2$ and $q \approx 10^4$ for a running density of hydrogen (8) for the cloud from the OB star. In the cloud from the WR star, Ω is determined by helium, while the carbon abundance can be taken to be 0.05, whence $\tau_b \approx 4 \times 10^4$ and $q \approx 2 \times 10^2$. Consequently, if the cloud is located in the vicinity of the frontal point, for any reasonable assumptions about T_g, there is no region of neutral carbon.

The parameter q for carbon increases due to the dilution factor when the cloud moves away from the hot stars. However, we must take into account the increase in the degree of ionization due to the decrease in the density as the cloud expands. It follows from (2) that

$$q \propto \frac{w}{n}. \tag{9}$$

The dependence $n(r)$ is determined by the cloud geometry. After deexcitation, the cloud assumes an anisotropic shape: its thickness l in the direction of the collision becomes appreciably smaller than the initial size d. For the sake of definiteness, let us suppose that $d = 10^{11}$ cm and $l = 10^8$ cm. We will take the expansion velocity for the cooled cloud to be $v_e = 10^5$ cm/s. During the time interval $\Delta t \leq d/v_e = 10^6$ s, the expansion of the cloud will be essentially one-dimensional. For such anisotropic expansion, the density decreases in inverse proportion to only the first power of distance, $n \propto 1/r$, and, according to (9), $q \propto 1/r$. In this case, the cloud moves to a distance r_d of the order of 3×10^{14} cm. This distance exceeds r_s by a factor of 55; i.e., $q = 4$. Thus, a cloud exactly satisfying the deexcitation criterion $j = 1$ will probably always be ionized by the OB-star radiation. In a cloud with $j = 10$, however, carbon has already been able to make the transition to its neutral state. We will assume that such clouds do exist, since the condition $j \geq 10$ does not seem excessive.

5. DUST FORMATION

Dust condensation should start after some delay, since some time is required for a cloud to move from the hot stars and for dust grains to grow after the corresponding conditions are met. A cloud with a velocity of about 3×10^8 cm/s (taking into account that momentum is partially lost in the collision) covers a distance r_d after roughly 10^6 s. After the formation of the region of neutral carbon, the adhesion of atoms and molecules to the condensation centers of future grains begins in the gas cooled during the adiabatic expansion. To estimate the rate of increase of a dust-grain radius, we will use the simple formula [23]:

$$\frac{da}{dt} = \frac{\rho_\text{C} v_T}{2\delta}. \tag{10}$$

Here, $\delta \approx 0.5$ g/cm^3 is the specific density of the dust, $v_T \approx 5 \times 10^4$ cm/s the thermal velocity of the carbon

atoms, and ρ_C the density of carbon. We will estimate this density as follows. In accordance with the above estimates, we assume the running density of the number of particles in the cloud $\mathcal{N}$ to be $10\Omega = 7 \times 10^{23}$ cm^{-2}. If the cloud consists primarily of helium, its running density is 4.6 g/cm^2, and a size of the cloud before the collision of 10^{11} cm and a carbon abundance in units of the number of particles of $Z_C = 0.05$ correspond to a density for the unperturbed carbon of 6.9×10^{-12} g/cm^3. Further, two processes tend to compensate each other: the compression of the de-excited gas behind the shock front and its subsequent expansion. We are interested in the termination of the one-dimensional expansion phase. We can assume that, at this time, the carbon density at least exceeds $\rho_C = 10^{-12}$ g/cm^3. Then, we can estimate $da/dt \approx 5 \times 10^{-8}$ cm/s from (10). For example, a radius of $a \approx 5 \times 10^{-5}$ cm is reached after about 10^3 s.

After the size of the cloud becomes approximately the same in all directions, its density starts to depend on r as $1/r^3$. As a result, the parameter q begins to increase in proportion to r, the cloud becomes more transparent and heated, and the radiation of the newly formed dust becomes brighter. For $j = 10$, the cloud becomes transparent when its radius roughly doubles, which takes approximately 10^6 s. During this time, the cloud moves another 3×10^{14} cm and, as a result, the dilution coefficient decreases to 5×10^{-7}. The temperature of the dust grains can be estimated from the condition that the rates of heating

$$W_a \approx \pi a^2 \sigma T_{\rm OB}^4 w e^{-\tau}$$

and cooling

$$W_c = \frac{2^8}{3}\pi^2 a^3 \frac{c(kT_g)^5}{(hc)^4} \times 24.9\kappa'$$

be equal. We will take the imaginary part of the index of refraction κ' to be 0.05 [23], and the dust-grain radius to be $(1–5) \times 10^{-5}$ cm. In the time interval considered, the optical depth is approximately equal to unity. Substituting the adopted parameters into the balance equation $W_a = W_e$, we obtain an estimate for the dust temperature: $T_g \approx (1.4 – 1) \times 10^3$ K.

6. DISCUSSION

Our scenario for dust formation concretizes ideas presented in earlier studies (see the Introduction) concerning the existence of two-phase winds and the need for rapid movement of dense, cool areas of the wind away from the exciting stars.

All processes necessary for the condensation of dust particles in the presence of a fast wind and powerful radiation field occur naturally in collisions of clouds and their subsequent movement away from the hot stars. For the system WR 140, our model can simultaneously explain both specific features of the X-ray spectrum and the system's IR radiation. Our calculations for the density contrast, IR flare delay, and temperature and chemical composition of the dust-formation area are consistent with both observations made in various studies and previous estimates of these parameters.

On the other hand, the model with only a rarified component encounters difficulties connected with the cooling of gas below a temperature of 10^4 K, and also the need to protect the carbon atoms from the ionizing radiation of the OB star. Moreover, the Coriolis force, which was not taken into account in [15], can accelerate the gas outflow from the frontal point; near the periastron of WR 140, the contribution of this force reaches 6%.

Thus, the presence of dust in the WR 140 system provides indirect evidence for two-phase winds from hot stars. Here, we have not considered the question of how the cloud component of the wind originates. The purpose of our study was to show that the cloud hypothesis could easily explain the specific features of the radiation of this system at all wavelengths.

REFERENCES

1. K. A. van der Hucht, B. Hidayat, A. G. Admiranto, *et al.*, Astron. Astrophys. **199**, 217 (1988).
2. S. V. Marchenko, A. F. J. Mofat, and Y. Grosdidier, in *IAU Symposium 193: Wolf–Rayet Phenomena in Massive Stars and Starburst Galaxies*, Ed. by K. A. van der Hucht, G. Koenigsberger, and P. R. Eenens, 1999, p. 368.
3. S. V. Marchenko, A. F. J. Moffat, and Y. Grosdidier, Astrophys. J. **522**, 433 (1999).
4. P. M. Veen, K. A. van der Hucht, P. M. Williams, *et al.*, Astron. Astrophys. **339**, L45 (1998).
5. P. M. Williams, K. A. van der Hucht, P. Bouchet, *et al.*, Mon. Not. R. Astron. Soc. **258**, 461 (1992).
6. P. M. Williams, K. A. van der Hucht, M. R. Kidger, *et al.*, Mon. Not. R. Astron. Soc. **266**, 247 (1994).
7. P. M. Williams, in *IAU Symposium 193: Wolf–Rayet Phenomena in Massive Stars and Starburst Galaxies*, Ed. by K. A. van der Hucht, G. Koenigsberger, and P. R. J. Eenens, 267 (1999).
8. I. Cherchneff and A. G. M. Tielens, IAU Symp., No. 163, 346 (1995).
9. S. J. Czyzak, J. P. Hirth, and R. G. Tabak, Vistas Astron. **25**, 337 (1981).
10. P. M. Williams, K. A. van der Hucht, and P. S. Thé, Astron. Astrophys. **182**, 91 (1987).
11. P. M. Williams, K. A. van der Hucht, A. M. T. Pollock, *et al.*, Mon. Not. R. Astron. Soc. **243**, 662 (1990).
12. J. A. Hackwell, R. D. Gehrz, and G. L. Grasdalen, Astrophys. J. **234**, 133 (1979).
13. P. M. Veen, A. M. van Genderen, K. A. van der Hucht, *et al.*, Astron. Astrophys. **329**, 199 (1998).

14. P. M. Williams and E. Antonopoulou, Mon. Not. R. Astron. Soc. **187**, 183 (1979).

15. V. V. Usov, Mon. Not. R. Astron. Soc. **252**, 49 (1991).

16. K. Annuk, IAU Symp., No. 163, 231 (1995).

17. E. L. Fitzpatrick, B. D. Savage, and M. L. Sitko, Astrophys. J. **256**, 578 (1982).

18. D. L. Lambert and K. H. Hinkle, Publ. Astron. Soc. Pac. **96**, 222 (1984).

19. O. V. Aleksandrova and K. V. Bychkov, Astron. Zh. **77**, 883 (2000) [Astron. Rep. **44**, 781 (2000)].

20. K. V. Bychkov, S. B. Egorova, and N. A. Katysheva, Astron. Zh. **70**, 1184 (1993) [Astron. Rep. **37**, 579 (1993)].

21. V. V. Sobolev, *Course of Theoretical Astrophysics* [in Russian] (Nauka, Moscow, 1967).

22. V. V. Golovatyĭ, A. A. Sapar, T. Kh. Feklistova, and A. F. Kholtygin, *Atomic Data for Spectroscopy of Rarefied Astrophysical Plasmas* [in Russian] (Tallin, 1991).

23. S. A. Kaplan and S. B. Pikel'ner, *The Interstellar Medium* [in Russian] (Fizmatgiz, Moscow, 1963).

Translated by K. Maslennikov

Astronomy Reports, Vol. 45, No. 4, 2001, pp. 287–293. Translated from Astronomicheskiĭ Zhurnal, Vol. 78, No. 4, 2001, pp. 333–340.

Modeling of Rapid Variability in the Spectral Line Profiles of Wolf–Rayet Stars

N. A. Kudryashova and A. F. Kholtygin

Astronomical Institute, St. Petersburg State University, Bibliotechnaya pl. 2, Petrodvorets, 198904 Russia

Received April 3, 2000

Abstract—Profiles of variable emission lines in the spectra of Wolf–Rayet stars are calculated using a stochastic cloud model for the inhomogeneous atmospheres of early-type stars. The model assumes that most of the line flux is formed in cold, dense condensations (clouds) that move through a rarified inter-cloud medium whose density monotonically decreases outwards. The formation of clouds is taken to be stochastic. Wavelet analysis is used to estimate the parameters of cloud ensembles. The model can reproduce the general pattern of line-profile variability observed in the spectra of Wolf–Rayet stars. *© 2001 MAIK "Nauka/Interperiodica".*

1. INTRODUCTION

Wolf–Rayet (WR) stars typically display a rapid variability of their emission-line profiles. In general, this variability is dominated by the appearance and disappearance of variable features (spikes) in the line profiles. The formation and evolution of these spikes are characterized by the following properties [1]: (1) the spikes appear and disappear randomly; (2) they evolve with time, drifting from the line center; (3) spikes that are initially displaced toward the red drift towards the red, while those initially displaced toward the blue drift towards the blue. In the spectra of early-type stars, narrow spikes moving along an emission-line profile are considered direct evidence for the presence of gas condensations in the atmosphere of the star. These condensations, which accelerate outward from the center of the star, are often called "clouds" [1, 2]. Additional convincing evidence for clumpy structure of the atmospheres of WR and other early-type stars has also been found [3, 4].

The hypothesis that there are condensations in the atmospheres of WR stars was first put forward as long ago as the middle 1980s [5], based on observations of the eclipsing WR + OB binary V444 Cyg. A cloud model for the atmospheres of WR stars was later suggested in [6] to explain the simultaneous presence in their spectra of lines of ions with low and high ionization potentials. This model proposes that the atmosphere contains an ensemble of condensations of various sizes and masses immersed in a rarified inter-cloud medium.

Despite the fact that the presence of condensations (clouds) in the atmospheres of early-type stars is currently generally accepted, both the mechanism for cloud formation and the law for their motion in the atmosphere remain unclear.

In [1, 7–9], some parameters of ensembles of clouds in the atmospheres of WR stars were derived based on the observed variability of emission-line profiles in the spectra of a number of stars. Here, we solve the inverse problem: reproducing the observed line-profile variability in the framework of the stochastic cloud model for the atmospheres of early-type stars proposed in [10, 11]. A similar model was applied in [9]. However that study, unlike our own, did not take into account the different lifetimes for clouds of different masses or the absorption of continuum radiation from the photosphere (or core) of the WR star by clouds in the line of sight to the observer.

2. STOCHASTIC MODEL FOR MOVING STELLAR ENVELOPES

At present, neither the mechanism for the formation of ensembles of clouds in the expanding atmospheres of WR stars nor the parameters for these ensembles are known. The random nature of the line-profile variability in the spectra of these stars suggests that the processes for the formation and "death" (dissipation) of clouds are also random. In this case, we can only speak of the probability for the formation of a cloud with some particular mass, size, line flux, etc. The values for each cloud are determined by the distributions of the mass, size, cloud gas-velocity dispersion, etc., for the entire cloud ensemble.

At each moment in time, the line profile is determined by random processes connected with the formation and "death" of clouds, while the mean profile obtained by averaging many individual profiles observed at different times depends primarily on the distributions of the parameters of the cloud ensemble. Since the mean line profiles of WR stars can be described by spherically symmetrical atmospheric models [12], this suggests that the cloud ensembles are also spherically symmetrical.

1063-7729/01/4504-0287$21.00

Table 1. Parameters of condensations

σ, km/s	L, cm	$L/R_\odot$
10	7×10^9	0.1
20	1.4×10^{10}	0.2
40	2.8×10^{10}	0.4
80	5.6×10^{10}	0.8
160	1.1×10^{11}	1.6
400	2.8×10^{12}	4.0

A random ensemble of clouds in a stellar atmosphere can be described using the stochastic cloud model proposed in [10, 11]. This model assumes that the clouds form in a layer bounded by the spherical surfaces $R = R_1$, $R = R_2$, and move outward radially with the stellar wind after they form. The total number of clouds in the atmosphere is assumed to be constant, so that, when a cloud is disrupted, a new cloud forms in the formation region. Note that the "death" of a cloud does not necessarily imply the disruption of its structure; rather, it indicates the action of some process that causes the cloud to cease to make an appreciable contribution to the total line profile.

Let us estimate the sizes of condensations in the stellar atmosphere. The widths of spikes in the spectra of WR stars are 40–160 km/s [1]. It is natural to assume that the width of a spike is determined by the dispersion of the gas velocities in the cloud σ, so that

$$\sigma = \langle \nabla V \rangle L, \tag{1}$$

where $\langle \nabla V \rangle$ is the gradient of the gas velocity in the atmosphere averaged over all directions and L is the characteristic size of a cloud. In a spherically symmetrical expanding atmosphere [13],

$$\langle \nabla V \rangle = \left\langle \frac{dV}{dR}\cos^2\theta + \frac{V}{R}\sin^2\theta \right\rangle \approx \frac{V}{R}. \tag{2}$$

Substituting (2) into (1), we obtain $\Delta R \approx (\sigma/\bar{V})\bar{R}$. Here, $\bar{V}$ and $\bar{R}$ are the average velocity of large-scale gas motions in the atmosphere and the distance from the cloud to the center of the star, respectively. Table 1 presents the characteristic size of condensations forming a line feature with velocity dispersion σ. For parameters $\bar{V}$ and $\bar{R}$, we chose the values 1500 km/s and $5R_*$, which are typical of WR stars, where $R_* \approx 5R_\odot$.

Lines 1 and 2 of Table 1 present estimates of the sizes L of condensations corresponding to spikes with widths of 10 and 20 km/s. Due to their low fluxes, such spikes have not yet been detected in the spectra of WR stars; the small condensations that would form them, however, may be present in WR atmospheres. The last line in Table 1 contains estimates of the size of a condensation forming a feature whose width is comparable to the total width of the line.

2.1. Line Radiation of a Cloudy Atmosphere

Let us consider the radiation of a cloudy atmosphere in some spectral line. The estimates of [1, 14] indicate that the total number of clouds in the atmosphere can exceed 10^3. These are primarily small clouds with sizes of $0.1–0.01R_\odot$ and smaller. For this total number of clouds, the average distance between them corresponds to roughly ten Doppler line widths at visible wavelengths, which implies that a line photon radiated by a cloud will probably not be absorbed by other clouds. Therefore, each cloud can be considered independently from the others, which makes it possible to represent the intensity of a line radiated by an ensemble of clouds as the sum of the contributions from individual clouds.

Let us assume that each cloud has its own line flux F, while the entire cloud ensemble has a flux distribution $N(F)$, such that $N(F)dF$ is the number of clouds with flux from F to $F + dF$. As was shown in [10], the clouds' flux distribution corresponds to their mass distribution. Let us assume, in accordance with [10], that the flux distribution is a power law, $N(F) \sim F^{-\alpha}$. Then,

$$N(F)dF = AF^{-\alpha}dF = n(f)df, \tag{3}$$

where $f = F/F_{\max}$ is the flux (in units of the maximum flux from an individual cloud); α is a parameter of the distribution, which we assume to be in the interval 1.25–2.5, in accordance with the estimates of [1]; and A is a normalizing coefficient.

Each cloud is described by the following parameters: θ_i, the angle to the radius vector connecting the cloud with the center of the star, measured from the z axis (which is directed along the line of sight from the observer); $F_i = F_i^0$, the flux from the ith cloud; t_i^0, the time of formation of the ith cloud; V_i^0, the velocity of the ith cloud at the time of its formation; r_i^0, the distance from the ith cloud to the center of the star at this time; τ_i, the lifetime of the ith cloud, determined such that the cloud "dies" a time τ_i after t_i^0. In keeping with the assumption that the formation of a cloud ensemble is stochastic, we take the flux radiated by a cloud to be random, distributed in accordance with (3). The radius vector for the formation site of a new cloud r_i^0 is a random value in the interval $[R_1, R_2]$, and is specified such that the continuity equation for the number density of clouds in the atmosphere is satisfied.

Here, we consider lines whose total flux is determined mainly by the contribution from the cloud component of the atmosphere. As noted above, in this case, the total flux in the line is equal to the sum of the contributions from individual clouds. We assume that each

cloud forms a feature (spike) with a Gaussian intensity distribution in the line profile. This assumption is based, first, on calculations of line profiles formed by a single cloud in a homogeneous atmosphere [10], and, second, on the fact that the observed intensity distributions of spikes in line profiles at visible wavelengths for a number of WR stars are close to Gaussian [1, 7].

Thus, let the energy radiated by the *i*th cloud in a line in the frequency interval $[\nu, \nu + d\nu]$ be

$$f_i(\nu) = I_i^0 e^{-\frac{1}{2}\left(\frac{\nu-\nu_i^0}{\sigma_i}\right)}. \quad (4)$$

Here, ν_i^0 is the central frequency of the spike formed by the *i*th cloud and σ_i is the spike width, which is determined by the dispersion of the gas velocity in the cloud. According to [1], $f_i \sim \sigma_i^2$. For the sake of generality, we assume that

$$f_i = \gamma\sigma_i^\eta, \quad (5)$$

where γ is a coefficient that depends on the line flux units, and the parameter $\eta \approx 2$.

The total flux from the *i*th cloud at the line frequencies considered is

$$f_i = \int_{-\infty}^{+\infty} f_i(\nu)d\nu.$$

Substituting (4) into this last formula, we obtain

$$f_i = I_i^0\sigma_i\sqrt{2\pi}. \quad (6)$$

The line flux at frequency ν radiated by the ensemble of clouds is

$$\mathcal{F}(\nu) = \sum_{i=1}^{N_{cl}} f_i(\nu),$$

where N_{cl} is the total number of clouds in the atmosphere.

The continuum radiation of the photosphere (core) of a WR star can be absorbed by clouds in the line of sight to the observer. The estimate of [10] indicates that the optical depth of clouds in the lines considered does not exceed unity. This absorption does not result in the appearance of absorption components in the line profiles; however, to some extent, it decreases the asymmetry of line profiles calculated without taking the absorption into account, enhancing the consistency between the observed and calculated mean line profiles. We took absorption into account in the continuum spectra, following the procedure described in [11].

Let us introduce the dimensionless units for the frequency of a line photon $x = (\nu - \nu_i^0)/\Delta\nu_\infty$, where $\Delta\nu_\infty = \nu_{ik}(V_\infty/c)$ is the Doppler line width, c the velocity of light, ν_{ik} the central frequency of the line, and V_∞ the limiting (terminal) velocity of the wind (~2000 km/s). In these units, the frequency corresponding to the maximum radiation from the *i*th cloud is

$$x_i^0 = (\nu_i^0 - \nu_{ik})/\Delta\nu_\infty = \frac{V(r_i)\cos\theta_i}{V_\infty}. \quad (7)$$

In dimensionless flux units, the line profile is described by the formula

$$I(x) = \sum_{i=1}^{N_{cl}} I_i^0 e^{-\frac{1}{2}\left(\frac{x-x_i^0}{\sigma(x_i)}\right)^2}. \quad (8)$$

Here, $\sigma(x_i)$ is the line profile width in dimensionless units. To describe gas motions in the expanding atmospheres of early-type stars, a standard β law for the variations of the wind velocity with distance from the center of the star is commonly used:

$$V(r) = V_0 + (V_\infty - V_0)\left(1 - \frac{R_*}{r}\right)^\beta. \quad (9)$$

Here, V_0 is the velocity of the cloud near the boundary of the photosphere, V_∞ the terminal wind velocity, R_* the radius of the stellar photosphere, and β a parameter that takes on values from 0.5 to 1. The time dependence for the cloud velocity can be derived from (9).

This type of distance dependence for the gas velocity in the atmospheres of early-type stars follows from a number of observational and theoretical studies [15, 16], and has been adopted in most studies of the spectra of these stars. We will also use this law for the cloudy component of the atmosphere, since the displacements of individual spikes in the line profiles of some O and WR stars [2, 17] indicate that the motion of the structures responsible for the formation of these spikes can be described by (9).

Let us describe our calculations of variable line profiles using the stochastic cloud model. Initially, we specify the parameters of the cloud ensemble. The values for $\theta_i^0 \in [0, 2\pi]$ and $r_i^0 \in [R_1, R_2]$ are chosen randomly. The initial velocities for the forming clouds are specified so that they depend on parameters r_i^0 in accordance with (9). For each cloud in the ensemble, the line flux is specified to be consistent with the distribution (3). The values for I_i^0, σ_i, and x_i^0 are derived using relations (5)–(7). The values for these parameters at an arbitrary time t can then be found from the law of motion for the clouds (9). We calculated the total line profile in accordance with (8).

The stochastic model for a cloud ensemble developed in [10] assumes that a cloud disappears after crossing some boundary, arbitrarily taken to be the boundary of the stellar atmosphere. This restriction can be removed if we assume that the ensemble consists of individual clouds that "live" for different times and thus

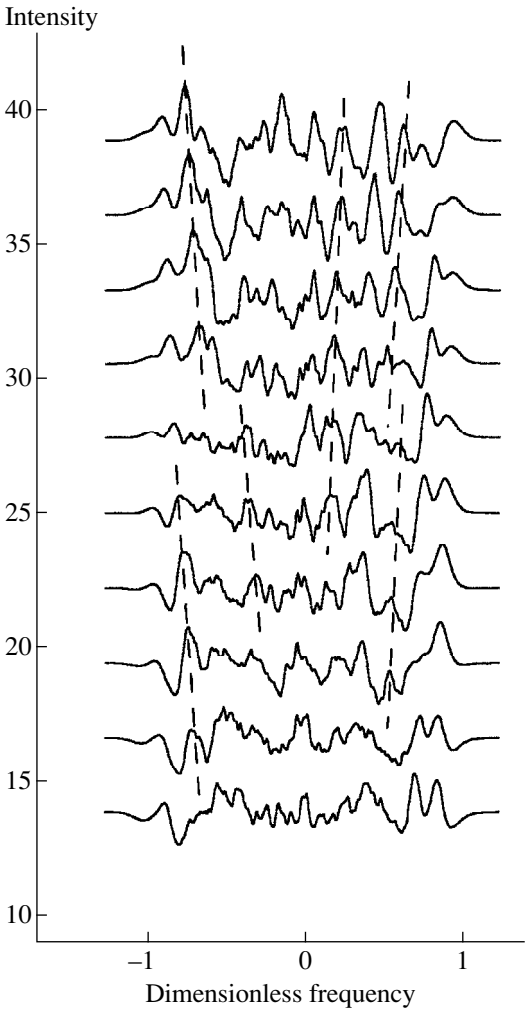

Fig. 1. Differential spectra of WR stars near C III λ5696 (individual minus mean profiles) calculated using the stochastic cloud model. Model parameters: $\varepsilon = 10^{-5}$, $\sigma_{max} = 0.20$. The time interval between consecutive differential spectra is 30 minutes, and the time axis is directed upwards.

"die" at different distances from the center of the star. Following the results of [1], which are based on observations, we can assume that the lifetime of an individual cloud τ is related to the line flux it radiates through the scaling relation $\tau \sim f^m$. Moffat *et al.* [1] suggest that $m \sim 0.8$. For the sake of generality, we assume that

$$\tau = Bf^m, \qquad (10)$$

where coefficient B is determined by the chosen flux units.

In this way, "instantaneous" line profiles for an arbitrary moment in time can be determined. Note that observed line profiles are always averaged and integrated rather than "instantaneous." To make our model more realistic, we calculated both "instantaneous" line profiles and "quasi-observed" profiles, averaged over some time interval Δt.

When calculating the "quasi-observed" line profiles, we specified a time interval t, corresponding to a total observation time. In this interval, we calculated individual "instantaneous" line profiles and then averaged over the interval Δt. Individual line profiles were calculated for all times of real line-profile observations, with the observation time for the first profile corresponding to $t = 0$. Further, we calculated the mean line profile for the entire period of "observations" (which equals the real observation time), and derived differential line profiles in the form of deviations of individual "quasi-observed" line profiles from the mean profiles.

2.2. Model Parameters

A cloud ensemble in the atmosphere is described by the parameters

$$\varepsilon, \sigma_{max}, \zeta, \beta, \alpha, N_{cl}, R_1, R_2, V_\infty, q, m, \qquad (11)$$

where $\varepsilon = F_{min}/F_{max}$ is the ratio of the minimum and the maximum line fluxes from individual clouds in the ensemble; σ_{max} the width of a spike in the line profile formed by a cloud with the maximum flux; and ζ the ratio of the energies radiated in the line and in the underlying continuum. For the sake of convenience, we express F_{max} as fractions of ζ. Note that, specifying ε and ζ, we completely determine F_{min} and F_{max}; β is the power-law index in (9); and α is a parameter of the flux distribution (3) of the clouds. Following the results of [1, 7, 8], which are based on a large amount of observational data, we take β and α to be equal to 1.0 and 2.0, respectively. N_{cl} is the total number of clouds in the atmosphere; we adopt $N_{cl} = 10^3$, in accordance with the estimates of [14]. R_1 and R_2 are the distances from the center of the star delineating the area of cloud formation; V_∞ is the terminal velocity of the wind (~2000 km/s), determined from observed line profiles; and $q = V_0/V_\infty \sim 0.1$.

Irrespective of the cloud-formation mechanism, the calculations of the ionization structure of the clouds performed in [6] indicate that the cloud density can exceed that of the surrounding medium by three to four orders of magnitude. In this case, the gas pressure in the clouds could appreciably exceed the mean gas pressure in the inter-cloud medium. Consequently, the clouds should be short-lived formations.

There is observational evidence [7] that the lifetimes of the largest peaks in line profiles can reach days, while the lifetimes of the smallest are minutes. We adopt the parameter B in relation (10) in accordance with these estimates. The parameter m in (10) is equal to 0.8, as was determined in [1] on the basis of observations.

Thus, despite the formally large number of parameters, in fact, our model depends primarily on only two. The parameters ε and σ_{max} cannot be derived directly from observations, and must be determined by other methods, as described below in Section 4.

Figure 1 presents some of our differential C III λ5696 line spectra. We chose the parameters of the stochastic cloud model to reproduce the type of variability observed for the profile of this line in the spectra of a number of WR stars [8]. The dashed lines mark the positions of spikes in the differential spectra, drifting from the line center toward the wings. Note the similarity between the general pattern of the variability in the model differential spectra and in the observed spectra for WR stars [1, 8, 17] and OB supergiants [2].

3. POWER SPECTRUM OF THE WAVELET TRANSFORMATION

Both the observed and model line profiles indicate that spikes are well localized, and the total line profile can be represented as a combination of the mean profile and several discrete spikes. Wavelet analysis is the most appropriate mathematical method to study the variability of such profiles. A wavelet method was used to analyze the variability of emission line profiles in the spectra of WR stars in [1, 7, 8], in particular, to identify spikes in total, summed line profiles.

We chose the so-called MHAT wavelet $\psi(t) = (1-t^2)\exp(-t^2/2)$ as the analyzing wavelet. It has a narrow energy spectrum and two zero-valued moments (the zeroth and first moment). The MHAT wavelet is well suited for the analysis of complex signals. Note that this wavelet is the second derivative of a Gaussian function, and the line fluxes from individual clouds can be represented by Gaussian profiles.

Using this wavelet, the integrated wavelet transformation can be written in the form (see, for example, [8, 18]):

$$W(a,b) = \frac{1}{a}\int_{-\infty}^{\infty} f(t)\psi\left(\frac{t-b}{a}\right)dt = \int_{-\infty}^{\infty} f(t)\psi_{ab}(t)dt. \quad (12)$$

The density of the signal energy $E_W(a, b) = W^2(a, b)$ describes the energy levels of the studied signal in the space (a, b) = (scale, time). The total energy is distributed over scales in accordance with the global energy spectrum for the coefficients of the wavelet transformation

$$E_W(a) = \int_{a_1}^{a_2} W^2(a,b)db = \int_{a_1}^{a_2} E_W(a,b)db. \quad (13)$$

This function is also called the power spectrum of the wavelet transformation. According to [8], the scale a where the function $E_W(a)$ reaches its maximum is called the dominating scale of the studied signal $f(t)$.

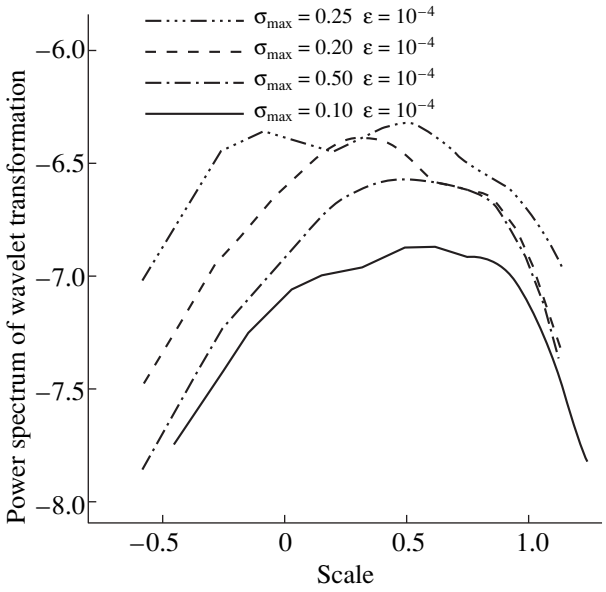

Fig. 2. Mean power spectra of the wavelet transformations for the calculated differential line profiles as a function of model parameters.

4. RESULTS OF LINE-PROFILE MODELING

We have calculated line profiles formed by a cloud ensemble for a broad range of parameters (11). To compare the observed and calculated line-profile variability, we used the procedure for modeling the observing process described in Section 2. In accordance with typical durations of observations, we adopted t = 600 min. In addition to individual line profiles, we also calculated profiles averaged over the time t, as well as differential (individual minus mean) profiles corresponding to a specified time. In this way, we obtained sequences of $t/\Delta t$ profiles; for each differential profile, we calculated the wavelet transformation (12) and its power spectrum (13). The power spectra obtained for a given realization of the model were then averaged.

Due to the random character of the cloud formation, we obtained different sets of line profiles for different

Table 2. Parameters of cloud ensembles in the atmospheres of WR stars

Object	Spectral type	ζ	V_∞, km/s	ε	σ_{max}
WR 103	WC9	17.0	1190	10^{-4}	0.22
WR 111	WC5	1.7	2415	10^{-5}	0.25
WR 134	WN6	2.0	1905	10^{-3}	0.20
WR 135	WC8	10.0	1405	10^{-5}	0.21
WR 136	WN6	2.3	1605	10^{-5}	0.20
WR 137	WC7 + OB	2.5	2550	10^{-5}	0.22
WR 138	WN5 + OB	0.4	1345	10^{-5}	0.23
WR 140	WC7 + O4-5	1.25	2900	10^{-4}	0.035

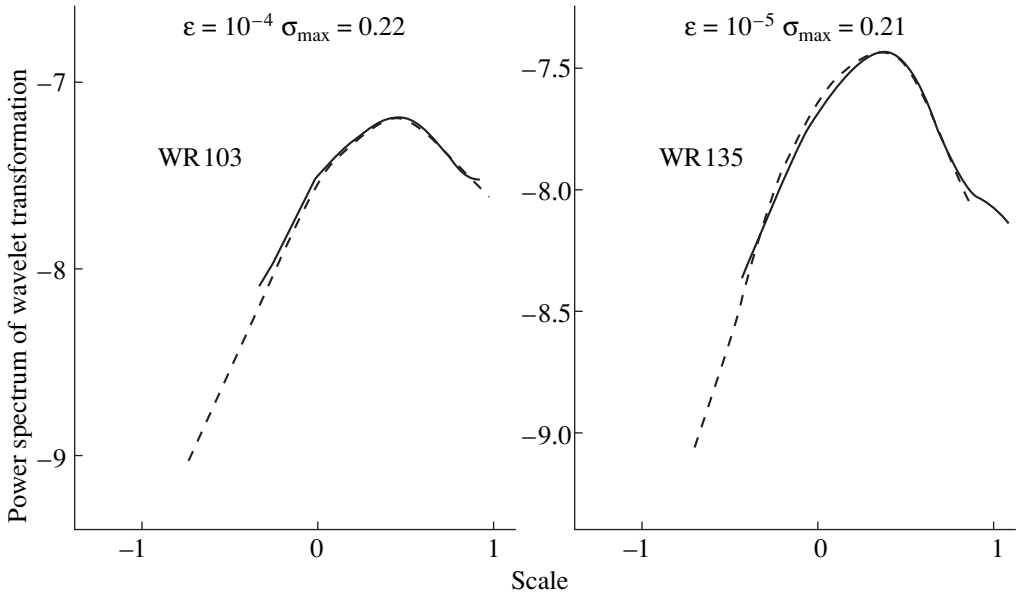

Fig. 3. Mean power spectra of the calculated differential line profiles (solid curves) compared with power spectra derived from observed C III 5696 and He II λ5511 line profiles in the spectra of WR stars [8] (dashed curves).

realizations of a model with a single set of parameters; however, the power spectra of the wavelet transformation for the differential profiles vary little. This means that the power spectrum describes the parameters of the cloud ensemble as a whole, rather than the parameters of the individual clouds making it up; thus, it can provide a criterion for our choice of the ensemble parameters.

To determine the characteristics of the cloud ensembles of specific stars, we selected the model parameters ε and σ_{max} to provide the best fit to the power spectra of the wavelet transformations for the differential line profiles of the observed spectra of WR stars [8]. For each star, we used V_∞ and ζ from [10]. Figure 2 presents the mean power spectra of the wavelet transformations for the calculated line profiles for various values of the model parameters. We can see that the mean power spectra are very sensitive to minor variations in the parameters.

Table 2 presents the resulting values of ε and σ_{max} for eight WR stars, together with the ζ values from [10]. The spectral types of the stars and their terminal outflow velocities from [8] are also presented and are given in Table 2. To illustrate the accuracy in the parameters of the cloud ensembles, Figure 3 compares the mean power spectra for the modeled differential profiles and the corresponding power spectra for the WR stars from [8].

5. DISCUSSION

When the calculated wavelet power spectra are compared with those derived from observations (Fig. 3), it is apparent that the observed variability in the line profiles is well described by the stochastic cloud model. The proximity of the σ_{max} values for different WR stars stands out (Table 2), suggesting that the parameters of the cloud ensembles in the atmospheres of these stars are also similar.

Note that σ_{max} is very large for all the stars (except WR 140). Assuming the terminal velocity is $V_\infty \approx 1.5$–2.0×10^3 km/s, as is typical for WR stars, we obtain a velocity dispersion of 200–600 km/s for the condensations responsible for the formation of the spikes with the maximum fluxes. According to Table 1, the size of condensations with such velocity dispersions can reach $4R_\odot$. There is no evidence for such large condensations in the atmospheres of WR stars [1], suggesting that no single atmospheric structure can be responsible for the formation of line-profile features with such large velocity dispersions. Most likely, broad peaks are formed by clusters of smaller clouds with similar average radial velocities. This supports the suggestion that cloud ensembles in the atmospheres of Wolf–Rayet stars have a hierarchical distribution [10].

The value ε can be used to determine the velocity dispersion for clouds with the minimum flux F_{min}. From relation (5) between the flux and the velocity dispersion of the clouds, we easily obtain $\sigma_{min} = \sqrt{\varepsilon}\,\sigma_{max}$. Substituting values from Table 2 into this formula, we find σ_{min} = 3–10 km/s, which corresponds to the thermal velocity of gas atoms in the clouds.

The special case of WR 140 ($\sigma_{max} = 0.035$) does not have an obvious explanation. This star is not set aside from the other WR stars in any clear way. Its only distinguishing feature is that it has the maximum terminal velocity (2900 km/s). It is possible that, at such high

V_∞, large clusters of clouds do not have sufficient time to form during the passage of clouds through the region in the atmosphere that radiates in the lines under consideration.

6. CONCLUSIONS

Comparisons between the observed and calculated line profiles, and also between the wavelet power spectra for the modeled and observed line profiles, show that the stochastic cloud model can reproduce the observed pattern of profile variability for emission lines in the spectra of WR stars. The model can be used to determine the parameters of cloud ensembles in the atmospheres of WR stars. The resulting parameter values suggest that clusters of clouds can form.

ACKNOWLEDGMENTS

The study was supported by the State Science and Technology Program in Astronomy (project 1.4.3.2). The authors are grateful to V.G. Gorbatsky for critical comments during the preparation of this work.

REFERENCES

1. A. F. J. Moffat, S. Lépine, R. N. Henriksen, and C. Robert, Astrophys. Space Sci. **216**, 55 (1994).
2. T. Eversberg, S. Lépine, and A. F. J. Moffat, Astrophys. J. **494**, 799 (1998).
3. A. M. Cherepashchuk, Astron. Zh. **67**, 955 (1990) [Sov. Astron. **34**, 481 (1990)].
4. S. Marchenko, A. F. J. Moffat, *et al.*, in *Wolf–Rayet Phenomena in Massive Stars at Galaxies (IAU Symposium 193)*, p. 47.
5. A. M. Cherepashchuk, J. A. Eaton, and Kh. F. Khaliullin, Astrophys. J. **281**, 774 (1984).
6. I. I. Antokhin, A. F. Kholtygin, and A. M. Cherepashchuk, Astron. Zh. **65**, 558 (1988) [Sov. Astron. **32**, 285 (1988)].
7. S. Lépine, Astrophys. Space Sci. **221**, 371 (1993).
8. S. Lépine, A. F. J. Moffat, and R. N. Henriksen, Astrophys. J. **466**, 392 (1996).
9. S. Lépine and A. F. J. Moffat, Astrophys. J. **514**, 909 (1999).
10. F. V. Kostenko and A. F. Kholtygin, Astrofizika **42**, 373 (1999).
11. A. F. Kholtygin, ASP Conf. Ser. **204**, 231 (2000).
12. D. J. Hillier, in *Wolf–Rayet Stars: Binaries, Colliding Winds, Evolution (IAU Symposium 163)*, Ed. by K. A. van der Hucht and P. M. Williams (Kluwer, Dordrecht, 1995), p. 116.
13. V. V. Sobolev, *A Course in Theoretical Astrophysics* [in Russian] (Nauka, Moscow, 1975), p. 354.
14. A. F. Kholtygin, in *Wolf–Rayet Stars: Binaries, Colliding Winds, Evolution (IAU Symposium 163)*, Ed. by K. A. van der Hucht and P. M. Williams (Kluwer, Dordrecht, 1995), p. 160.
15. Kh. F. Khaliullin and A. M. Cherepashchuk, Itogi Nauki Tekh., Ser. Astron. **21**, 5 (1982).
16. J. I. Castor and H. J. G. L. M. Lamers, Astrophys. J., Suppl. Ser. **39**, 481 (1979).
17. A. F. J. Moffat, L. Drissen, R. Lamontagne, and C. Robert, Astrophys. J. **334**, 1038 (1988).
18. N. M. Astaf'eva, Usp. Fiz. Nauk **166** (11), 145 (1996) [Phys. Usp. **39**, 1085 (1996)].

Translated by K. Maslennikov

Astronomy Reports, Vol. 45, No. 4, 2001, pp. 294–300. Translated from Astronomicheskiĭ Zhurnal, Vol. 78, No. 4, 2001, pp. 341–348.

Unusual Features of the Millisecond Pulsar 1937 + 21 at 406.9 MHz

V. A. Soglasnov[1], A. D. Skulachev[1], N. D'Amico[2,3], S. Montebugnoli[2], K. V. Semenkov[1], A. Maccaferri[2], and A. Cattani[2]

[1]*Astro Space Center, Lebedev Physical Institute, Profsoyuznaya ul. 84/32, Moscow, 117810 Russia*
[2]*Istituto di Radioastronomia, CNR, via Gobetti 101, Bologna, 40129 Italy*
[3]*Bologna Astronomical Observatory, via Zamboni 33, Bologna, 40126 Italy*

Received April 20, 2000

Abstract—Observations of the millisecond pulsar PSR B1937 + 21 acquired in Summer 1997 with the Medicina cross telescope revealed two interesting features: the existence of long-lived microstructures persisting over several minutes, and a close relationship between the pulsar flux and pulse arrival times, due to refraction on a discrete inhomogeneity. The latter effect, though observed earlier at higher frequencies by the Nancay group, is rather peculiar at our low frequency. © *2001 MAIK "Nauka/Interperiodica".*

1. INTRODUCTION

The radio emission of millisecond pulsars (MSPs)—very interesting but, unfortunately, rather faint objects—has thus far been studied less thoroughly than that of "normal" pulsars, which have periods of the order of a second. This is especially true for events with extremely short timescales (less than a milliperiod), such as microstructure, which are important for our understanding of the physical mechanisms for energy generation in the magnetospheres of neutron stars. Pulsars (including MSPs) have very steep spectra, making preferable observations at low frequencies, where they have the highest flux densities. In addition, observations of MSPs at low frequencies are of interest for studies of propagation effects in the interstellar medium and in the pulsar magnetospheres, which are more strongly manifest at lower frequencies.

The first millisecond pulsar discovered, PSR B1937 + 21 (J1939 + 2134 in the notation of epoch 2000), is the brightest in the northern hemisphere (only the very nearby pulsar J0437 – 4715 is brighter), making it a suitable target for further study. However, this pulsar has the shortest period (1.557 ms) and a dispersion measure that is large for an MSP (71.04 cm^{-3} pc). These factors strongly hinder observations at frequencies below 1 GHz, where the group pulse delay due to the dispersion of the radio waves in the interstellar plasma strongly distorts the pulse shape. Such distortions place a fundamental limit on the time resolution of multichannel systems with filter combs that are usually used in pulsar observations. For the pulsar in question at 407 MHz, it is impossible to achieve a resolution better than 100 μs, twice its profile width. Therefore, we used a more complex technique for predetection reduction of the signal [1], which has no fundamental time resolution limitation. The data were reduced in real time using the digital spectrometer of the radio observatory in Medicina, which was specially programmed for this purpose [2].

Our observations, which had sub-microsecond resolution, yielded interesting results. We detected two rather unusual features, the first probably related to propagation effects, and the second to the pulsar itself. An earlier set of low-frequency observations of PSR 1937 + 21, also with predetection compensation for the dispersion (but with poorer resolution), was acquired mainly with the 300-m Arecibo radio telescope. Those results were primarily concerned with interstellar scattering and other propagation effects [3]; the remarkable phenomenon of "giant" pulses was also noted [4, 5].

2. OBSERVATION AND REDUCTION TECHNIQUES

Our observations were obtained on June 16–July 12, 1997, using the north–south arm of the cross radio telescope of the CNR Istituto di Radioastronomia near Medicina (Italy) [6] at 406.9 MHz. The telescope recorded linearly polarized signals. The receiver bandwidth was 2 MHz (of which 1.6 MHz was effectively used). The signal, reduced to the zero frequencies, was digitized using 250-ns bins and sent to the digital spectrometer in a "coherent de-dispersor" [2] mode in blocks of 131072 (128 K) counts. The dispersion removal was conducted in real time via signal processing in the spectral domain: after computing the complex Fourier spectrum, each harmonic was multiplied by a phase factor, equal in absolute value but opposite in sign to the phase increment due to dispersion in the interstellar medium. Further, the inverse Fourier transform was computed and digitized, and the restored signal was sent to an adder that accumulated the mean profile. The total number of cycles accumulated was 1831, corresponding to one minute of time. The dataset was then sent to a control computer to be saved on disk, and a new accumulation cycle was initiated. The algorithm used was

1063-7729/01/4504-0294$21.00

such that, of the initial 131072 counts, only 56092 were valid after removal of the dispersion (corresponding to 14.023 ms, or nine pulsar periods); thus, the effective profile integration time in a single one-minute exposure was 25.7 s (16 479 periods).

The observations were acquired near culmination, since the telescope is a transit instrument. The total time for PSR 1937 + 21 to cross the beam between the zero levels was 14 min. During each transit, 24 one-minute exposures were recorded. Nine registered near the center of the beam were used to derive the mean profile, study the pulse timing, etc., whereas the first few and last few exposures were used as "empty sky" records for comparison and error estimation. For this, we added an "artificial" smooth profile to the "empty sky" record and reduced the data in the same way as the pulsar records. We estimated the actual accuracy of the measured parameters for different signal-to-noise ratios by changing the amplitude of the artificial profile; this is especially important when analyzing short variations of the pulse arrival times (PATs) during a transit, when the signal is strongly variable. For the PATs, such estimates give an rms error of 2.2 μs for a one-minute exposure and 0.8 μs for accumulation over the entire transit.

We used the TIMAPR software written by O.V. Doroshenko [7, 8] for the computation of the pulsar period (needed for observations) and subsequent analysis of the PATs.

3. RESULTS AND DISCUSSION

3.1. The Mean Profile

The mean profile of PSR 1937 + 21 accumulated for 1862127 pulses over the entire observation period (Fig. 1) clearly shows the effects of interstellar scattering: both the main pulse and the interpulse have exponentially extended trailing edges, characteristic of a large number of ray scatterings (a so-called "diffraction mode"). The observed profile shape is in good agreement with a simple Gaussian pulse model, $\exp[-(t^2/2w^2)]$, scattered by a thin phase screen, represented by convolution with the function $U(t)\exp[-(t/\tau_s)]$. Here, $U(t)$ is a step function—$U(t) = 0$ for $t < 0$ and $U(t) = 1$ for $t \geq 0$—and we used the following values for w and τ_s (the profile width and scattering timescale): $w = 20 \pm 1$ μs, $\tau_s = 25 \pm 2$ μs for the main pulse and $w = 21 \pm 3$ μs, $\tau_s = 28 \pm 6$ μs for the interpulse. These values agree with other measurements at similar frequencies [3]. PSR 1937 + 21 has been observed more often than other MSPs, and its profile is relatively well known, especially at frequencies of 1400 MHz and above [9, 11]. High-frequency data have shown the main pulse to consist of two components with an intensity ratio of about 3 : 1, with the fainter pulse being narrower and separated from the maximum by 35 μs (towards later times) [9, 11]. At our frequency, this component is difficult to distinguish, as it is strongly masked by the scattered radiation of the stronger and broader central component. A slight deformation of the trailing edge offers a hint of its presence.

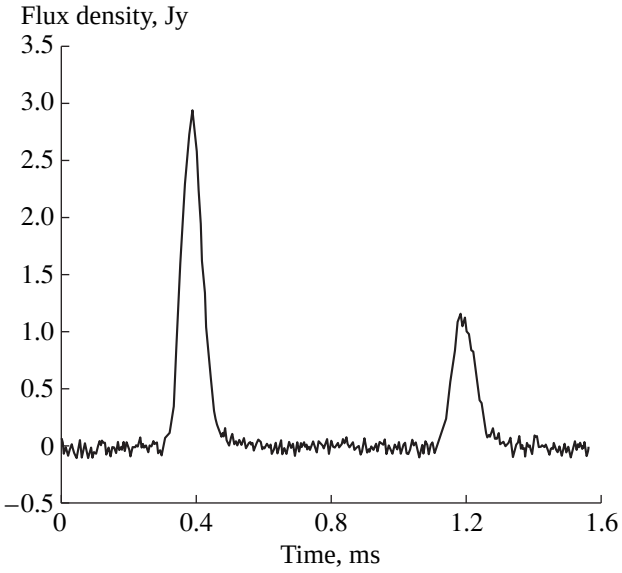

Fig. 1. Mean profile of PSR B1937 + 21. The data were smoothed with a Gaussian filter with a time constant of 11.3 μs.

Another faint component of the main pulse leading the strong pulse is manifest as a rise before the leading edge (also detectable at high frequencies); a similar component is present in the interpulse.

3.2. Intensity and PAT Variations

During our observations, the flux from the pulsar varied by up to 35%. This can be seen, for example, in Fig. 2, which presents the amplitudes of the main pulse and interpulse derived for each one-minute exposure as a function of time relative to culmination. The mean curves drawn through these points represent to good accuracy the shape of the antenna beam, but the data points themselves demonstrate a large scatter, especially near the beam center, considerably in excess of the errors. Rapid flux changes within a single transit, as well as slower, day-to-day variability, were observed. We determined the mean flux in a single transit from the amplitude of a least-squares-fit $\sin x/x$ curve representing the beam shape (Fig. 2). The deviations of the data points from these curves exceed the noise and represent real intensity changes during a transit. The flux shows correlated changes in the main pulse and interpulse, with a correlation coefficient of 0.36 (uncorrected for noise; the corrected value is 0.44). We can see from the auto- and cross-correlation functions (Fig. 3) that the timescale of the variations slightly exceeds 1 min, the individual accumulation time, and is approximately 100 s. Variation amplitudes are usually described using the modulation index m: $m^2 = \overline{(I - \bar{I})^2}/\bar{I}^2$, which varies between 0.1 and 0.28 on various dates (the mean value is 0.178). This scatter is primarily due to the small statistics for a

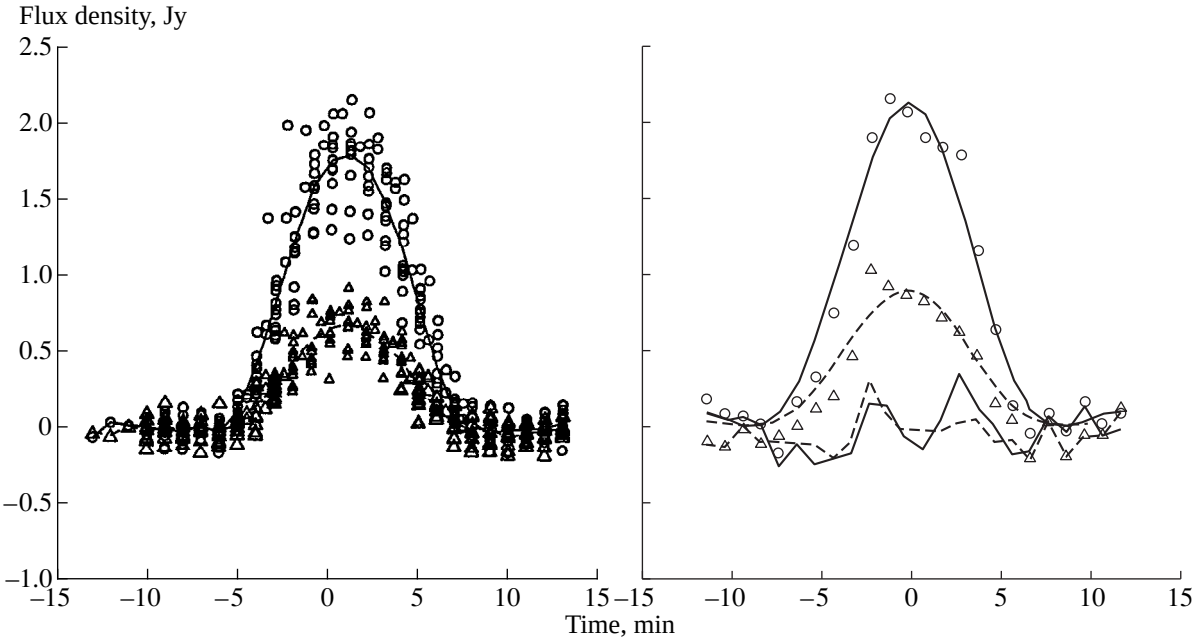

Fig. 2. Flux density of the main pulse (circles) and interpulse (triangles) as a function of time relative to culmination. Each point represents a one-minute integration. The left panel shows data acquired over the entire observation period, and the right panel data from the single transit of July 4, 1997. The solid and smooth dashed curves are the radio telescope beam superposed on these data. The curves in the bottom of the right panel are rapid variations of the flux density. The solid and dashed curves refer to the main pulse and interpulse, respectively.

single transit, the duration of which exceeds the variation timescale by only a factor of four to five.

Similar behavior is demonstrated by the PATs. The differences between the precalculated and observed PATs fluctuate synchronously in the main pulse and interpulse (the correlation coefficient is 0.41) to within ±10 μs, with an rms deviation of 2.1 μs. The variation timescales for the intensity and PATs coincide, as indicated by a comparison of their auto-correlation functions (Fig. 3); however, the PATs and the intensities fluctuate independently, and no correlation between them was detected.

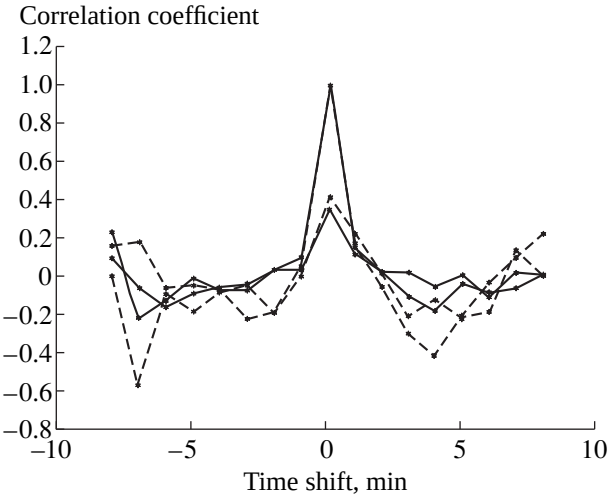

Fig. 3. Auto- and cross-correlation functions of the flux variations (solid curves) and the pulse arrival times (dashed curves) for the main pulse and interpulse. The auto-correlation function for the main pulse corresponds to the right side of the figure (positive shifts), and for the interpulse to the left side (negative shifts).

Rapid variations are the main factor limiting the accuracy of flux determinations in a single transit to 2–3%. However, the observed day-to-day flux variations are significantly in excess of this value (Fig. 4). The flux varies synchronously in the main pulse and interpulse. Against the background of the overall slow decline, we can see a smooth minimum with a duration of 14 days (from June 21, 1997 to July 4, 1997) and amplitude 35% and a local maximum on June 28–29, 1997, when the flux increased by 20%. Interestingly, the ratio of the intensities of the main pulse and interpulse was not constant, and decreased roughly linearly from 2.6 to 2.2 from the beginning to the end of our observations, except for an abrupt drop on June 28, 1997 (i.e., near the local maximum), when it suddenly decreased to 2.0 and then gradually returned to the linear trend. The origin of this abrupt change was that the intensity increase in the local maximum was stronger for the interpulse, and started somewhat earlier than for the main pulse.

The flux variability associated with these slow variations is accompanied by changes in the PAT. The difference between the predicted and observed PATs varies by up to 13 μs (Fig. 4); most remarkable is that the

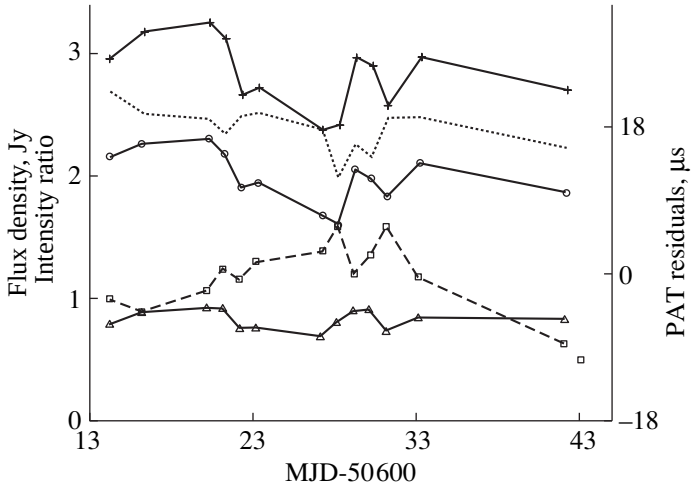

Fig. 4. Flux variations in the main pulse (circles) and interpulse (triangles), their ratio (dashed curve), variations in the combined flux (asterisks), and the PATs (squares) for the entire observation period. The numbers along the vertical axis are the same for the flux density and the intensity ratio.

PAT curve is, in virtually all details, a mirror image of the flux variations: decreasing intensity corresponds to increased pulse delays and vice versa (the correlation coefficient is -0.69 ± 0.04; the minus sign indicates that the pulses arrive earlier at increasing intensity).

A similar anticorrelation between flux and PAT variations was noted for this pulsar at a higher frequency (1400 MHz) in [12, 13] as a rather rare phenomenon (nine events observed in three years) with close time scales (12–15 days), however, without a detailed correspondence between the PAT and intensity curves.

3.3. Interstellar Scintillation, Scattering, and Refraction

Flux-density variations can be due to the pulsar's intrinsic variability, as well as the propagation of the radio waves through an inhomogeneous turbulent plasma, either in the interstellar medium or the region surrounding the pulsar (scintillations). Diffractive and refractive scintillations must be distinguished. Diffractive scintillation is due to the motion of the Earth with respect to the diffraction pattern formed by radiation scattering on numerous small inhomogeneities; refractive scintillation is due to the diffraction of rays on one or several larger inhomogeneities. Both types of scintillation can be generated by the same turbulent medium. In this case, the ratio of the timescales for "normal" refractive and diffractive scintillations should be of the order of $\sim\tau_s\nu$, and the ratio of the amplitudes of the PAT variations should be $\sim(\tau_s\nu)^{-1/3}$, where ν is the observing frequency.

The nature of the rapid variations is beyond doubt: they are described well by diffractive scintillation. It is characteristic of diffractive scintillation that intensity fluctuations are correlated within a frequency band $\Delta\nu_s$ (the "decorrelation bandwidth"), which is related to the scattering timescale τ_s, by the "uncertainty relation" $2\pi\Delta\nu_s\tau_s = 1$. The same is true of the PAT fluctuations. If the received bandwidth B is narrower than $\Delta\nu_s$, the modulation index for the intensity fluctuations will be close to unity, ($m \sim 1$), and the amplitude of the PAT fluctuations will be $\Delta t \sim \tau_s$. However, if B is broader than $\Delta\nu_s$, then m and Δt are reduced by a factor of $\sim(B/\Delta\nu_s)^{0.5}$. In our observations, the effective bandwidth was 1.6 MHz and the modulation index was $m \approx 0.17\%$, which coincides with the observed value for the short-timescale variations. The timescale for diffractive scintillations τ_s measured at the nearby frequency of 430 MHz is 100 s [3], which also corresponds to the timescale for rapid variations. The pulsar's tangential velocity,

$$V = \frac{A}{\nu}\left(\frac{cD}{8\tau_s}\right)^{1/2}$$

is usually determined from τ_s; we will use it below for some numerical estimates. The distance to the pulsar D is determined from the dispersion measure, based on a model for the n_e distribution in the Galaxy. Following [17], we adopt the value $D = 3.6$ kpc (a value a factor of two larger was estimated earlier). The coefficient A depends on the turbulence parameters and the scattering model used; following [15], we adopt the value 0.15. In this case, $V = 47$ km/s.

The nature of the slow variations is much more interesting: they show the unusual property of a strong (nearly functional) relationship between the intensity and PAT variations (correlation coefficient -0.69 ± 0.04 the minus means that as the intensity increases, the pulses begin to arrive ear lier; Fig. 4). This suggests that the slow variations are due to propagation effects, since the intrinsic PAT variations for PSR 1937 + 21 measured at high frequencies where such effects have little influence do not exceed 1 μs [9] (this is one of the most stable pulsars).

Such a relation between the pulse delay and the observed intensity is characteristic of refractive scintillation [14], when a large inhomogeneity with dimensions $a \geq (c\tau_s L)^{-0.5}$ crosses the line of sight ($L = L_1L_2/(L_1 + L_2)$, where L_1 and L_2 are the distance from the refracting inhomogeneity to the pulsar and to the Earth, respectively). This leads to an additional delay in the PATs, consisting of two terms: a dispersive delay, $\tau_D \propto \nu^{-2}\delta\mathrm{DM}$, where $\delta\mathrm{DM}$ is the additional dispersion measure due to the inhomogeneity, and a geometric delay, τ_G, due to the fact that the inhomogeneity deflects the rays by an angle $\theta_{\mathrm{ref}} = c\,\mathrm{grad}\,\tau_D$:

$$\tau_G \approx 0.5cL(\mathrm{grad}\,\tau_D)^2 \propto \nu^{-4}L(\mathrm{grad}\,\delta\mathrm{DM})^2.$$

Convergence or divergence of the refracted rays will correspondingly increase or decrease the observed intensity, $I = I_0 + \delta I$: $\delta I/I_0 \sim (1 - cL\,\mathrm{div}\,\mathrm{grad}\,\tau_D)^{-2} - 1$. Appreciable variations of the intensity, $\delta I/I_0 \geq 0.1$, will occur if the dispersion delay and geometric delay are of the same order of magnitude: $\tau_D \sim \tau_G$. The index of refraction of a plasma is smaller than unity, giving rise to a "focusing" effect (intensity increase) in an inhomogeneity with reduced density, whereas an inhomogeneity with enhanced density will reduce the intensity. This can explain the relationship between the PAT and intensity variations: τ_D and τ_G are minimum near the minimum of $\delta\mathrm{DM}$, where the convergence of the rays (and hence the intensity) is maximum; thus, increasing intensity will correspond to decreasing delay and vice versa. However, in the general case, for an arbitrary n_e distribution, this relation will only be approximate, without a detailed correspondence. For any realistic distribution, the PAT curve has a minimum when the line of sight is close to the center of the inhomogeneity, where $\mathrm{grad}\,\delta\mathrm{DM}$ is near zero; however, a corresponding local maximum of the intensity appears only when there is a region with reduced density at the center of the inhomogeneity.

Note that this effect cannot originate in the same turbulent medium that is responsible for the diffractive scintillation: according to the relations presented at the beginning of this section, the timescale for "normal" refractive scintillation should be of the order of 20 to 30 days, close to the observed timescale, while the PAT variation amplitude will be only 1 μs, significantly below the observed value. Thus, the refraction takes place in a discrete inhomogeneity (a similar phenomenon is observed in the "extreme scattering events" observed in some compact extragalactic sources [16]). Assuming that the inhomogeneity's tangential velocity (relative to the line of sight) is $V \approx 50$ km/s, we can use the duration of the minimum, $\sim 14^{\mathrm{d}}$., to estimate the linear size of the inhomogeneity to be $a \sim 6 \times 10^{12}$ cm. This is a factor of ~50 smaller than the size of the scattering circle in the interstellar medium. Therefore, in order to give rise to appreciable flux variations, the refracting inhomogeneity must be close to either the Earth or the pulsar, at a distance < 80 pc. Assuming that $\mathrm{grad}\,\delta\mathrm{DM} \sim \delta\mathrm{DM}/a$ and using the above relations, we obtain $\delta\mathrm{DM} \sim 2 \times 10^{-4}$ cm^{-3} pc. This yields an estimate for the mean density of free electrons in the inhomogeneity of $n_e \sim 100$–200 cm^{-3}; this should be ~25% lower at the center, in order for the central region to focus the rays and create a local intensity maximum and corresponding PAT minimum with the observed amplitudes. Such an object cannot exist in the interstellar medium for long because of the large implied pressure difference (a factor of several hundred). To avoid this difficulty, a model with a special multi-filament structure was suggested in [10, 14]. We find it more natural to suppose that this phenomenon is associated with activity of the pulsar itself, with such inhomogeneities arising near the pulsar in the "pulsar wind" zone, where the properties of the turbulent plasma strongly differ from those of the standard interstellar medium.

4. MILLISECOND-TIMESCALE PHENOMENA: MICROPULSE BURSTS

Ordinary pulsars (with periods of the order of a second) exhibit microstructure phenomenon in which short bursts of radiation—micropulses lasting for 10^{-3} to 10^{-6} of the period—are observed in some pulses. The lifetime of this microstructure is brief, much shorter than the period; the microstructure never survives until the next pulse, and is therefore not represented in the mean profile. Millisecond pulsars are too faint for individual pulses to be observed (with a single exception; see below), so that the existence of microstructure similar to that observed for ordinary pulsars remains an open question. However, thanks to the high time resolution of our observations, we were able to detect an interesting phenomenon, resembling "long-lived" microstructure surviving for several minutes, enabling its detection in the mean profiles for short accumulation times as "micropulse bursts." During such bursts, a very narrow peak with width of the order of a microsecond appears in the profile and becomes stronger, until its amplitude becomes comparable to that of the main pulse itself. Further, its intensity decreases and it disappears completely.

To get a more detailed picture of this phenomenon, we consider the strongest burst, observed on June 17, 1997, when the peak's maximum amplitude became equal to that of the main pulse (Fig. 5). The peak is present in three subsequent one-minute integrations, so that the phenomenon lasted about 2 min. During this time, no drift or longitude displacement of the peak was observed; it followed the pulsar period with high precision (at least to 10^{-8}), possibly testifying that the event was associated with the pulsar itself and not due to propagation effects. At the burst maximum, the microsecond peak is visible in each of the nine profiles independently accumulated during a single one-minute interval. It follows that the peak could not be formed from one or several "giant" pulses, and is associated with a comparatively

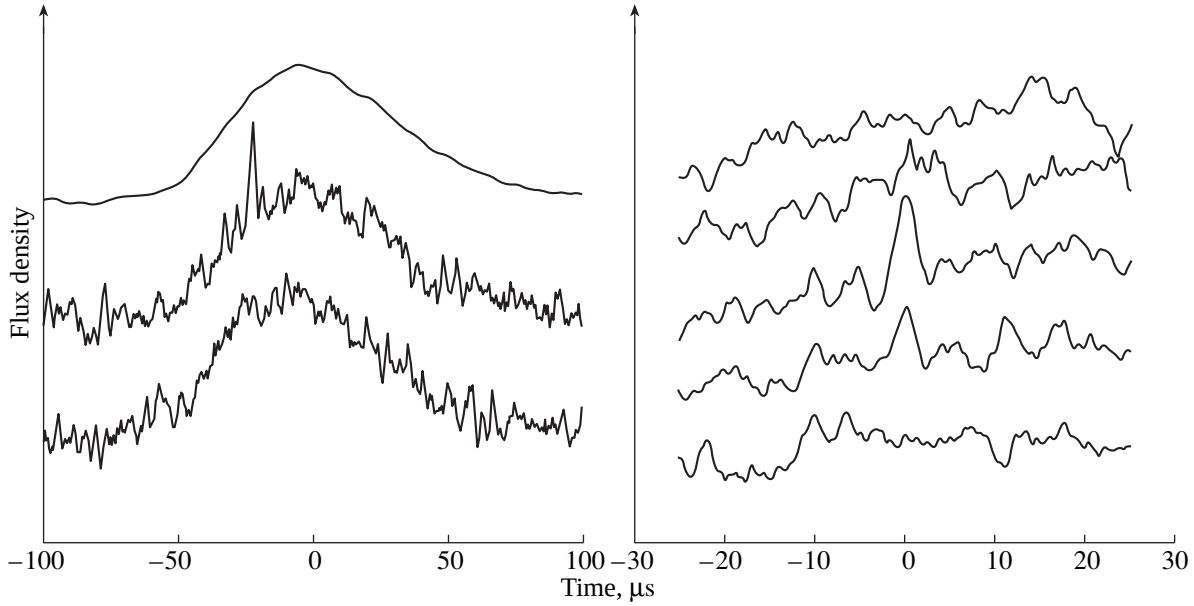

Fig. 5. The strong micropulse burst of June 17, 1997. The left panel shows the profile of the main pulse for a long accumulation (0.8 h; upper curve) and several short accumulations: for three minutes during the burst (middle curve) and the remaining six minutes, and for one minute before the burst and five minutes after it (lower curve). The right panel shows the development of the phenomenon in time. The 50 μs part of the profile in five subsequent one-minute accumulations are shown from top to bottom.

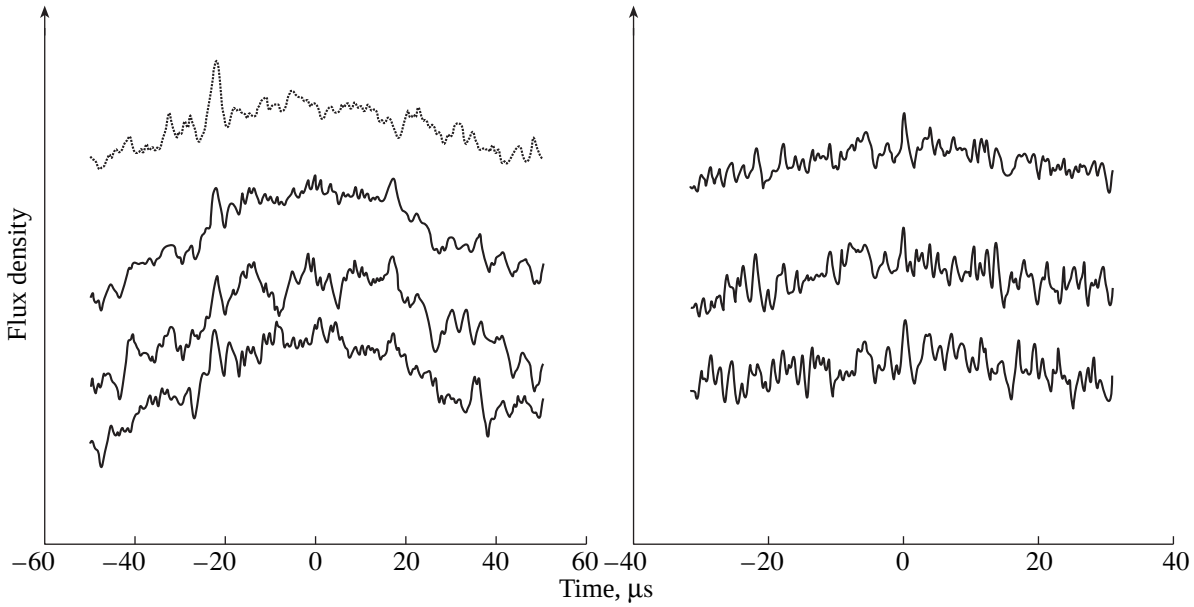

Fig. 6. Two fainter bursts apparent during the whole transit. For both, the fraction of the profile accumulated over the entire transit and two independent half-time accumulations are shown. In the profile of the burst of June 24, 1997 (left panel), two micropulse peaks are simultaneously present. The phase of one of these (preceding the maximum of the profile) exactly coincides with the phase of the peak for the burst of June 17, 1997, shown by the dotted line.

stable formation with an enhanced generation of radiation within a narrow longitude interval.

Although such bright bursts are probably fairly rare, the phenomenon is not unique: we also found several fainter (with lower peak amplitude) but longer bursts, some lasting for at least 9 min (the beam-crossing time for the pulsar). Figure 6 presents two such bursts. It is interesting that one of these (on June 24, 1997) has its peak exactly at the same longitude as for the burst of June 17, 1997. The accumulated statistics are insuffi-

cient to judge whether the bursts are concentrated in certain preferred longitude ranges or whether this coincidence is due to chance.

Another type of phenomenon with a short, microsecond, timescale in PSR 1937 + 21 is individual "giant" pulses observed at a given longitude in both the main pulse and interpulse [5]. It is possible, however, that these two types of event are actually manifestations of the same phenomenon and have a common physical nature. We can speculate that a "hot spot" appears in the polar cap, producing a "bright filament" in the magnetosphere: an excited region extended along a line of force is formed, where the generation of radiation is enhanced.

The long-lived microstructure observed for PSR 1937 + 21 may present the first evidence for a strong dissimilarity between ordinary and millisecond pulsars; the other properties of the radio emission of MSPs and normal pulsars are remarkably similar, despite substantial differences in the physical conditions in their magnetospheres. Note that the microstructure of normal pulsars is due to modulation of the plasma flow along open lines of force.

Is the presence of long-lived microstructure a typical property of all or most MSPs, or is PSR 1937 + 21 unique in this respect? Currently, we cannot answer this question definitively, because the observational data on the radio emission of MSPs on short timescales are too sparse and, moreover, contradictory. Until now, only one MSP was studied—J0437 – 4715, the closest (and thus brightest). This is the only known MSP with detectable individual pulses for each period. It has been observed by two groups: in Ooty (India) at 318 MHz [18] and Parkes (Australia) at 1380 MHz [19], with completely different results and conclusions. According to [18], very narrow unresolved micropulses are often observed within individual pulses, with amplitudes much higher than the mean intensity, appearing predominantly at specific preferred longitudes. For short profile-integration times, a picture similar to the micropulse-burst phenomenon observed by us could be derived. However, the high-frequency Parkes observations do not confirm this result.

5. CONCLUSION

(1) The correlation between flux variations and pulse arrival times observed for PSR 1937 + 21 at high frequencies becomes a detailed correspondence at low frequencies. This effect is due to refraction in an inhomogeneity with dimensions $\sim 6 \times 10^{12}$ cm with a density of free electrons $n_e \sim 100$–200 cm^{-3}. Such inhomogeneities most likely arise in the turbulent medium close to the pulsar, in the "pulsar wind" zone.

(2) The millisecond pulsar PSR 1937 + 21 shows "long-lived" microstructure, with lifetimes from several minutes to possibly dozens of minutes. This phenomenon has no counterpart in "normal" (second) pulsars. It may be associated with the appearance of a compact "hot spot" in the polar cap, which ignites a bright filament in the magnetosphere.

ACKNOWLEDGMENTS

The authors wish to thank the staff of the radio observatory in Medicina for their assistance during observations, as well as M.V. Popov, who initiated this study and made a number of useful comments. This study was supported by the Russian Foundation for Basic Research (project code 98-02-16917) and INTAS (project 96-02-0154).

REFERENCES

1. T. H. Hankins and B. J. Rickett, Methods Comput. Phys. **14**, 55 (1975).
2. A. D. Skulachev, V. A. Soglasnov, N. D'Amico, *et al.*, Tr. Fiz. Inst. Akad. Nauk **229**, 105 (2000).
3. J. M. Cordes, A. Wolszczan, R. J. Dewey, *et al.*, Astrophys. J. **349**, 245 (1990).
4. A. Wolszczan, J. M. Cordes, and D. R. Stinebring, in *Millisecond Pulsars*, Ed. by S. P. Reynolds and D. R. Stinebring (NRAO, Green Bank, 1984), p. 63.
5. I. Cognard, J. A. Shrauner, J. H. Taylor, and S. E. Thorsett, Astrophys. J. Lett. **457**, L81 (1996).
6. N. D'Amico, G. Grueff, S. Monebulgoni, *et al.*, Astron. Astrophys., Suppl. Ser. **106**, 611 (1995).
7. O. Doroshenko, http://www.mpifr-bonn.mpg.de/div/pulsar/former/olegd/soft.ht
8. O. Doroshenko and S. Kopeikin, Mon. Not. R. Astron. Soc. **274**, 1029 (1995).
9. I. Cognard, G. Bourgois, J.-F. Lestrade, *et al.*, Astron. Astrophys. **296**, 169 (1995).
10. B. J. Rickett, A. J. Lyne, and Y. Gupta, Mon. Not. R. Astron. Soc. **287**, 739 (1997).
11. J. Kijak, M. Kramer, R. Wielebinski, and A. Jessner, Astron. Astrophys. **331**, 804 (1998).
12. I. Cognard, G. Bourgois, J.-F. Lestrade, *et al.*, Nature **366**, 320 (1993).
13. J.-F. Lestrade, B. J. Rickett, and I. Cognard, Astron. Astrophys. **334**, 1068 (1998).
14. J. M. Cordes, M. Pidwerbetsky, and R. V. E. Lovelace, Astrophys. J. **310**, 737 (1986).
15. J. M. Cordes, Astrophys. J. **311**, 183 (1986).
16. R. L. Fiedler, B. Dennison, K. J. Johnston, and A. Hewish, Nature **326**, 675 (1987).
17. J. H. Taylor and J. M. Cordes, Astrophys. J. **411**, 674 (1993).
18. J. G. Ables, D. McConnel, A. A. Deshpanand, and M. Vivekanand, Astrophys. J. Lett. **475**, L33 (1997).
19. F. A. Jenet, S. B. Anderson, V. M. Kaspi, *et al.*, Astrophys. J. **498**, 365 (1998).

Translated by N. Samus'

Astronomy Reports, Vol. 45, No. 4, 2001, pp. 301–308. Translated from Astronomicheskiĭ Zhurnal, Vol. 78, No. 4, 2001, pp. 349–358.

A Comparative Analysis of Chemical Abundances in the Atmospheres of Red Giants of Different Age Groups

A. A. Boyarchuk[1], L. I. Antipova[1], M. E. Boyarchuk[1], and I. S. Savanov[2]

[1]*Institute of Astronomy, Russian Academy of Sciences, ul. Pyatnitskaya 48, Moscow, 109017 Russia*

[2]*Crimean Astrophysical Observatory, Ministry of Science and Technology of Ukraine, p/o Nauchnyĭ, Crimea, 334413 Ukraine*

Received April 14, 2000

Abstract—We analyze previously published chemical abundances in the atmospheres of red giants. Excess abundances are observed not only for Na, but also for Al and Si, with the overabundances increasing with the stars' luminosity. The observed anomalies provide evidence that, in addition to the CNO hydrogen-burning cycle, the Mg–Al and Ne–Na cycles operate in the interiors of main-sequence stars; their products are brought to the stellar atmospheres by convection after the transition to the red-giant phase. The abundance anomalies for *s*-process elements, also observed in the atmospheres of field stars, testify to the presence of a substantial number of neutrons. The *s*-process abundance anomalies are absent from giants of the young Hyades cluster.

1. INTRODUCTION

It has been established that nuclear reactions that synthesize chemical elements are the main source of stellar energy. Because of their widespread nature and high energy release, reactions transforming hydrogen into helium dominate. These processes can occur in two ways. The first is consecutive proton merging (the p–p cycle). The second involves the bonding of protons to carbon, nitrogen, or oxygen atoms in the region of nuclear burning, forming unstable isotopes of these elements and leading to subsequent beta decay, followed by the attachment of a new proton; a chain of such transformations ends in the formation of an alpha particle (the CNO cycle). The relative efficiency of the two series of reactions depends on the temperature in the region of burning, which depends, in turn, on the star's mass.

Stellar hydrogen burning occurs mainly in the cores of main-sequence stars. The computations of internal stellar structure show that, at this evolutionary stage, a star consists of a convective core, where nuclear reactions occur, and a radiative envelope, where hydrogen-burning reactions do not take place due to its low temperature. The atmospheric chemical compositions of such stars should not differ from that of the proto-stellar material—the interstellar medium—with the exception of the abundances of lithium, beryllium, and boron, which burn at low temperatures.

However, the situation changes drastically when the main-sequence stars become red giants. Calculations show that the core shrinks after the depletion of hydrogen, while the envelope expands in size by a factor of several dozen and becomes convective. Thus, the possibility arises for nuclear reaction products to be dredged up into the stellar atmosphere, where they can be detected.

First and foremost, we expect a significant increase of the helium abundance. However, the atmospheric temperatures of red giants are insufficient to excite helium lines, and so they are not observed. Further, during the CNO cycle, the total number of CNO atoms is conserved, but their relative abundances change, as observed in the atmospheres of giants. This is considered confirmation of the theory of stellar structure and evolution.

For a long time, possible changes of other elements' abundances were neglected. Only in the 1980s was an excess sodium abundance detected in the atmospheres of supergiants [1–3], which was correlated with luminosity [3] and the $^{12}C/^{13}C$ isotope ratio [4]. The reason for this lack of attention to possible changes in the abundances of other elements is probably the huge number of nuclear reactions occurring in the mixture of elements making up stellar gas. They cannot all be fully taken into account, and so stellar-evolution computations have included only reactions with the largest energy output. In addition, until recently, accuracies of abundance determinations were low for at least three reasons:

(a) signal-to-noise ratios for photographic plates were about 30, whereas those for modern observations with CCDs reach 100 to 200 or higher;

(b) formerly, uncertainties in oscillator strengths exceeded a factor of two, whereas they are now several percent for many lines;

(c) modern model atmospheres enable analysis of abundances with much higher accuracy than, for example, the curve-of-growth method.

1063-7729/01/4504-0301$21.00

Table 1. Program stars and adopted atmospheric parameters

HR	Star	Spectral type	T_e, K	log$g$	V_t, km/s
		Normal red giants			
437	η Psc	G7IIIa	4955	2.10	1.50
951	δ Ari	K2IIIv	4346	2.03	1.30
2077	δ Aur	K0III	4935	2.64	1.24
2990	β Gem	K0IIIb	4933	3.00	1.25
4924	37 Com	G9III	4745	2.35	1.80
7310	δ Dra	G9III	4897	2.86	1.41
7615	η Cyg	K0III	4906	2.85	1.30
7942	52 Cyg	K0III	4930	3.06	1.30
8684	μ Peg	G8III	5022	2.73	1.41
		Mild barium stars			
3475	ι Cnc	G7.5IIIaBa0.1	4895	2.18	1.96
8115	ξ Cyg	G8III–IIIaBa0.6	4977	2.52	1.40
8667	λ Peg	G8IIIaCN1Ba0.3Hδ – 1	4860	2.05	1.85
		Hyades red giants			
941	κ Per*	K0III	4923	2.77	1.16
1346	γ Tau	K0IIIabCN1	4956	2.83	1.35
1373	δ^1 Tau	K0IIICN0.5	4980	2.84	1.25
1409	ε Tau	G9.5IIICN0.5	4880	2.50	1.46

* Belongs to the Hyades moving group.

These improvements in techniques for analyzing stellar spectra make it possible to detect comparatively small deviations in elemental abundances. With this in mind, several years ago, we commenced a program to investigate abundances in the atmospheres of red giants using ample and homogeneous spectroscopic material and uniform techniques, to ensure reliable comparative analyses for stars of different subtypes. We concentrated on the abundances of the light elements Na, Al, and Si (which can vary at temperatures that are not extremely high) and of elements with very low abundances, such as the rare earths. The abundances of this latter set of elements can change appreciably due to neutron capture. (Current theories of stellar evolution predict that the abundances of the iron-peak elements should not vary in the main-sequence and red-giant stages, and change only in supernova outbursts.)

During this program, we obtained spectroscopic observations for several dozen red giants. Thus far, we have performed analyses for 16 of them. Table 1 presents a list of the stars studied, which can be subdivided into three groups:

(a) giants of the general field, with no indications in the literature concerning any peculiarities in their spectra, which we call "normal" (nine stars);

(b) mild-barium field stars (three stars);

(c) giants from the Hyades supercluster (three known bright giants of the Hyades cluster and one giant belonging to the Hyades moving group).

It is of interest to compare the abundances in the atmospheres of these groups of stars. In our earlier papers [5–9] devoted to individual stars, we discussed the principal aspects of our techniques for abundance analyses in stellar atmospheres in detail, and briefly discuss here only those pertaining to the accuracy of our estimates.

2. OBSERVATIONS

Our observations were acquired with the 2.6-m telescope of the Crimean Astrophysical Observatory, using a CCD detector in the first chamber of the Coud'e spectrograph of the telescope. The dispersion was 3 Å/mm and the signal-to-noise ratio was $S/N \geq 100$–300. A spectral band with a width of either 30 or 60 Å could be recorded simultaneously, depending on the type of CCD detector used. The bands (from 14 to 20 used) were chosen to record the number of spectral lines required for the problem at hand. We reduced the data using software developed for this purpose at the Crimean Astrophysical Observatory.

Our analysis of stellar spectra is differential, using the Sun as the comparison star. Accurate differential analyses require the reduction of data for both the program objects and the comparison object using the same techniques. Therefore, we carried out observations of the Sun—i.e., of scattered daylight—with the same instrument at the 2.6 m G. Shain telescope [10].

The extent to which the spectrum of the scattered daylight corresponds to the solar spectrum and can be used for comparative astrophysical studies was discussed in detail in [11], on the basis of special observations. The depths of the lines in the day sky spectrum depend, to some extent, on the angle between the telescope and the direction towards the Sun. The larger this angle, the shallower the lines, and, accordingly, the lower the corresponding equivalent widths. The largest deviations from the real values were 3–4%, corresponding to $\Delta \log W_\lambda \leq 0.02$ dex, and occurred at deviations from the Sun of about 100°; upon further increase of this angle, the deviations become smaller again. We note in this connection that, in our observations, the telescope was oriented 30° from the direction towards the Sun [10]; therefore, we do not expect errors $\Delta \log W_\lambda > 0.01$ dex, so that our errors do not exceed the errors in the equivalent widths.

3. ANALYSIS OF SPECTROGRAMS

We paid much attention to careful tracing of the continuum: to a considerable extent, this procedure determines the accuracy of the final results for red giants. Because the CCD detector recorded only small portions of the spectrum, we drew the continuum tak-

ing into account photographic spectrograms covering about 1000 Å. We selected lines that were not distorted by blends and had trustworthy oscillator strengths for subsequent analysis. The line equivalent widths were determined using the EW program written at the Crimean Astrophysical Observatory [12], which enables approximation of the profile of an unblended spectral line with a Gaussian curve and plotting of the residual intensity vs. equivalent width calibration curve. This calibration curve was used to determine the equivalent widths of lines with blended wings that could not be approximated using Gaussian profiles; in such cases, only lines whose central depths were not distorted by blends were taken.

4. CHOICE OF MODEL ATMOSPHERE. COMPUTATION OF ELEMENTAL ABUNDANCES

We analyzed the line equivalent widths for the abundance determinations using model atmospheres computed with Kurucz's ATLAS9 package [13]. We computed the elemental abundances from the measured equivalent widths using the WIDTH9 program. Our estimates of the model atmosphere parameters $T_{\rm eff}$ and $\log g$ for the program objects were based on the technique described in detail in [8]. This technique applies the criterion that, according to current theories of stellar evolution, the relative abundances of iron-peak elements should not change during the main-sequence and giant stages. Therefore, the abundances of all iron-peak elements in a giant's atmosphere relative to the solar values should be the same, and reflect the star's metallicity. With this in mind, we computed the abundances of iron-peak elements for each of the program stars from the measured equivalent widths for various $T_{\rm eff}$ and $\log g$ that were close to the expected values, and then determined the atmospheric parameters giving the minimum scatter in the relative abundances for these elements. As an example, Fig. 1 displays a plot of $\log(\varepsilon/\varepsilon_0)$ for 52 Cyg. It was shown in [8] and [10] that this type of analysis for the iron-peak elements can simultaneously yield estimates of the effective temperature (with an accuracy of ±20 K), gravity (with $\log g$ values accurate to ±0.10), and mean metallicity of the stellar atmosphere (to ±0.05 dex) without invoking additional data. Further, we used the ATLAS9 software to compute the corresponding model atmosphere for the analysis of the composition of the atmosphere of the program red giant.

Note that the choice of atmospheric parameters described here gives "formal" values that are not always coincident with spectroscopic estimates. For example, the solar effective temperature, corresponding to the known solar constant, is T_e = 5777 K, and the Sun's gravity derived from the motions of planets around the Sun is $\log g$ = 4.44; however, as shown in [10], the line spectrum of the Sun is best described by the model atmosphere from [13] with T_e = 5887 K and $\log g$ = 4.57 (the "formal" solar parameters for the grid of models in [13]). Unfortunately, the Sun is the only star whose parameters have been determined independently of model atmospheres and with satisfactory accuracy.

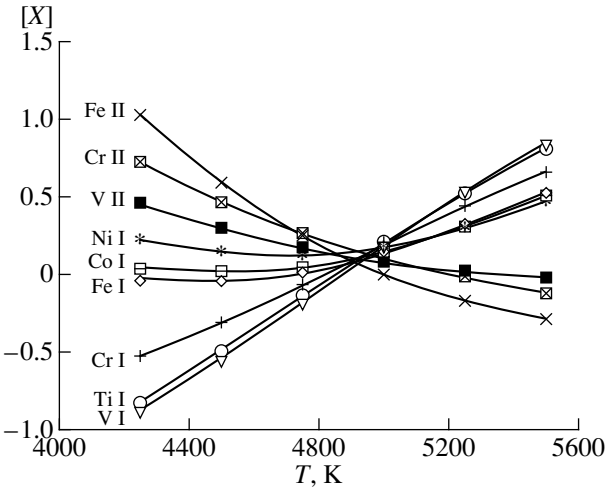

Fig. 1. Abundances of iron-peak elements relative to their solar values, derived from the observed equivalent widths of absorption lines in the spectrum of 52 Cyg for $\log g$ = 3.06 and various temperatures.

Currently, the most accurate stellar effective temperatures are those derived from stellar angular diameters based on either interferometric or lunar-occultation measurements. In the formula used to determine T_e, the angular diameter—i.e., the ratio of the star's linear diameter to its distance—is raised to the –1/2 power, whereas the bolometric flux is raised to the 1/4 power (see, for instance, [14]). Thus, errors in bolometric flux estimates do not strongly influence T_e, and the main sources of errors in T_e are errors in the angular diameter, which are typically about 10%. For the temperatures of the stars in our study, such methods yield errors in T_e of about 250–300 K—much higher than the errors in the model-atmosphere parameters.

The situation with stellar surface-gravity estimates is worse. For this purpose, the star's mass and radius must be known. Information about the masses of single stars is extrapolated from data on binary stars. It is very difficult to estimate the accuracy of this procedure. We cannot prove that the (mass–spectral type, luminosity) relations for single and binary stars are the same. In addition, the errors in the masses for the components of binary systems reach tens of percent. A star's radius is derived from its apparent bolometric magnitude, which, in turn, is determined by the star's parallax (if known) and surface temperature. Here, the temperature is raised to the fourth power, and the influence of its error (about 10%) on the error in the surface gravity increases accordingly. In addition, the average parallax

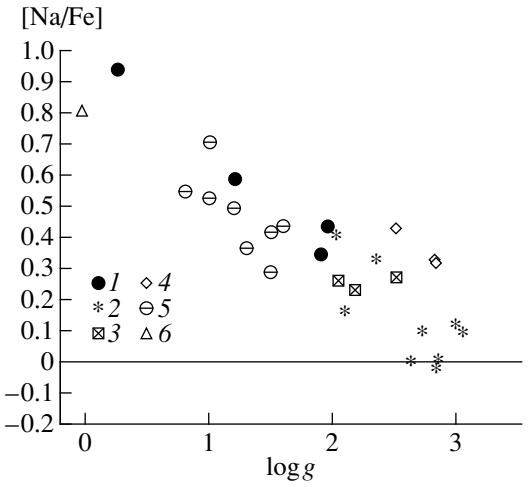

Fig. 2. Excess sodium abundance in the atmospheres of red giants and supergiants: (*1*) normal giants; (*2*) mild barium stars; (*3*) Hyades giants; (*4*) supergiants from [1–3]; (*5*) supergiants from [26]; (*6*) supergiants from [27].

error is about 10%. Thus, we estimate the errors in $\log g$ for single stars to be $\pm(0.3–0.5)$ dex.

In light of these considerations, we will treat the derived values of T and $\log g$ exclusively as atmospheric parameters of the program stars that may deviate from the effective temperature T_e and the surface gravity, though not by a large amount. Our analysis of the spectra for a single star using models from different model-atmosphere grids shows that T_e and $\log g$, as well as the resulting metallicities ([Fe/H] ratios), can be somewhat different for different models, but the ratios of various abundances to the iron abundance are in good agreement, and it is this information that is most important for our study.

Using analogous techniques and Kurucz models, we determined the parameters for the solar model atmosphere, then used the corresponding model atmosphere to determine elemental abundances in the solar atmosphere based on the spectral lines used for the analysis of the red-giant spectra [10]. The resulting abundances coincided with those published for the solar atmosphere by Grevesse and Sauval [15] to within ±0.05 dex, suggesting that we have correctly chosen the oscillator strengths. Further, for each of the studied lines, we found the differences in the abundances (log N) for the atmospheres of the star and the Sun, and then averaged these differences for each element. In this way, we avoid possible errors due to the use of inaccurate individual oscillator strengths.

We determined the turbulent velocity V_t from iron lines, which are numerous and cover a wide range of equivalent widths. We chose the V_t value for which there was no dependence between the iron abundance and the line equivalent width. This value was used in the subsequent analysis. Having determined the final values of T_e and $\log g$, we then checked the correctness of V_t and, if necessary, repeated the analysis with an improved value of V_t.

The resulting atmospheric parameter values for each star are collected in Table 1. The final chemical composition of the stellar atmospheres was determined using the model computed for these parameters and the ATLAS9 package. It is shown in [9, 13] that such determinations are accurate to ±0.10 dex.

5. RESULTS

Table 2 presents the abundances in the atmospheres of the program stars. For each star and each element, we give

$$[\text{elem/H}] \equiv \log[\varepsilon(\text{elem})/\varepsilon(\text{H})]_* - \log[\varepsilon(\text{elem})/\varepsilon(\text{H})]_\odot,$$

i.e., the difference of the abundances relative to hydrogen for the atmospheres of the studied star and of the Sun. (Note that, in our earlier studies [5–7], we used the model atmospheres from [16] for some of the stars. Later we re-reduced these observations using the models from [13], and the latter results are presented in Table 2.) We analyze the data from this table below.

Na abundance. As stated above, enhanced Na abundances were first noted for supergiants [1–3], and it was shown that the Na excess depended on luminosity. Note that the Na abundances were derived from the λ6161 and λ6154 Å subordinate lines. Special studies of possible deviations from LTE [17, 18] demonstrated that non-LTE effects were small for these lines, as was confirmed in subsequent studies [19, 20]. Figure 2 shows the dependence of [Na/Fe] on $\log g$ for supergiants [1–3] and for the 16 red giants studied by us, with the abundances determined from the same subordinate lines. We can readily see that the positions of the giants are in good agreement with the supergiant relation, suggesting that the Na abundances in the supergiants and giants have the same nature. The mild barium stars also agree well with this relation, whereas the Hyades stars lie somewhat above it.

Boyarchuk and Lyubimkov [3] suggested that Na could be formed in the reaction $^{22}\text{Ne}(p, \gamma)^{23}\text{Na}$—part of the neon cycle in the cores of main-sequence stars—and could be dredged up from deep layers to the stellar atmosphere by convection during the star's evolution from the main sequence to the red-giant stage. The computations in [4, 21] and the observational relation between the anomalous Na excess and the $^{12}\text{C}/^{13}\text{C}$ isotope ratio [4] support this hypothesis.

Thus, the spectra of giants, as well as supergiants, probably provide evidence that products of the core Ne–Na hydrogen-burning cycle have been dredged up into surface layers. The fact that the mild barium stars follow the relation of Fig. 2 suggests that the Na production in their stellar cores and its dredging-up are essentially the same as for normal field red giants.

Table 2. Relative atmospheric elemental abundances

Elements	Normal red giants									Mild barium stars			Hyades red giants			
	η Psc	δ Ari	δ Aru	β Gem	37 Com	δ Dra	η Cyg	52 Cyg	μ Peg	ι Cnc	ξ Cyg	λ Peg	κ Per	γ Tau	δ^1 Tau	ε Tau
	[elem/H]															
Na I	+0.16	+0.33	+0.09	+0.19	+0.51	−0.09	+0.13	+0.20	+0.01	−0.01	+0.19	+0.33	–	+0.43	+0.51	+0.51
Al I	–	+0.17	+0.26	+0.34	+0.31	+0.00	+0.33	+0.26	+0.07	+0.01	+0.16	+0.27	+0.29	+0.23	+0.27	+0.31
Si I	+0.14	+0.01	+0.09	+0.22	+0.36	+0.04	+0.26	+0.13	−0.02	−0.05	+0.09	+0.23	+0.19	+0.18	+0.24	+0.20
Ca I	−0.05	+0.04	+0.10	+0.11	+0.21	+0.01	+0.12	+0.11	−0.06	−0.13	−0.03	+0.06	+0.10	+0.12	+0.19	+0.10
Sc II	−0.17	+0.11	+0.04	+0.01	+0.10	+0.01	+0.16	+0.12	−0.05	–	−0.02	+0.08	+0.06	+0.11	+0.20	–
Ti I	−0.01	−0.05	+0.14	−0.04	+0.22	−0.15	+0.11	+0.10	−0.14	−0.27	−0.11	+0.09	+0.07	+0.10	+0.15	+0.06
V I	−0.04	–	+0.09	+0.01	+0.17	−0.06	+0.18	+0.07	−0.06	−0.31	−0.04	+0.06	+0.14	+0.12	+0.21	+0.07
V II	−0.16	−0.12	+0.07	+0.08	–	−0.16	+0.15	+0.12	−0.10	–	–	+0.08	+0.11	–	–	+0.10
Cr I	−0.03	−0.17	+0.08	+0.06	+0.23	−0.15	+0.12	+0.10	−0.10	−0.28	−0.08	+0.07	+0.06	+0.10	+0.15	+0.11
Cr II	−0.06	−0.10	–	+0.14	+0.18	−0.09	+0.19	+0.15	−0.06	–	−0.07	+0.07	+0.06	+0.08	+0.18	+0.05
Fe I	−0.02	−0.08	+0.08	+0.07	+0.12	−0.08	+0.15	+0.09	−0.06	−0.21	−0.03	+0.09	+0.11	+0.11	+0.19	+0.11
Fe II	−0.01	−0.08	+0.08	+0.08	+0.14	−0.12	+0.08	+0.02	−0.08	−0.14	−0.11	+0.05	+0.08	+0.11	+0.18	+0.05
Co I	−0.05	−0.03	+0.10	+0.13	+0.24	−0.03	+0.23	+0.11	−0.14	−0.24	−0.13	+0.09	+0.14	+0.13	+0.20	+0.10
Ni I	+0.01	−0.23	+0.08	+0.15	+0.21	−0.10	+0.18	+0.13	−0.06	−0.20	−0.09	+0.10	+0.14	+0.11	+0.24	+0.11
Y II	−0.07	+0.04	−0.01	+0.11	+0.21	−0.07	+0.12	+0.35	−0.01	−0.03	+0.30	+0.08	+0.00	+0.12	+0.14	+0.06
Ba II	+0.33	+0.19	+0.35	+0.17	+0.20	−0.05	+0.35	+0.31	+0.31	−0.04	+0.54	+0.38	+0.17	+0.20	+0.34	+0.20
La II	+0.11	+0.17	+0.23	+0.15	+0.29	+0.00	+0.17	+0.32	+0.11	+0.05	+0.45	+0.20	+0.02	+0.08	+0.14	−0.06
Ce II	+0.02	+0.15	+0.17	+0.18	+0.35	+0.13	+0.35	+0.48	+0.16	+0.10	+0.33	+0.28	+0.09	+0.03	+0.14	+0.06
Pr II	+0.09	+0.12	+0.32	+0.27	+0.38	+0.18	+0.37	+0.49	+0.23	–	+0.43	+0.33	+0.09	+0.15	+0.13	+0.06
Nd II	+0.07	+0.16	+0.19	+0.20	+0.39	+0.20	+0.40	+0.62	+0.23	+0.09	+0.23	+0.30	+0.17	+0.13	+0.21	+0.01
Eu II	+0.06	+0.31	+0.25	+0.29	+0.32	+0.22	+0.34	+0.48	+0.22	+0.17	+0.22	+0.29	+0.16	+0.36	+0.29	+0.16
[M/H]*	−0.02	−0.09	+0.09	+0.13	+0.19	−0.10	+0.15	+0.10	−0.09	−0.24	−0.08	+0.08	+0.10	+0.10	+0.19	+0.08

* Mean metallicity derived as the mean abundance for iron-peak elements.

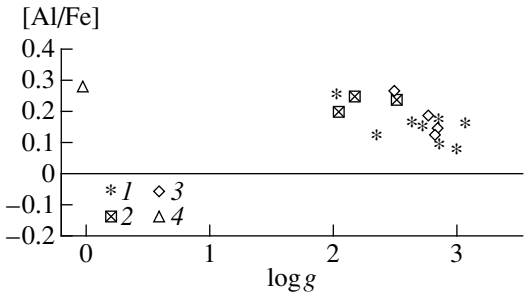

Fig. 3. Excess aluminum abundance in the atmospheres of red giants and supergiants: (*1*) normal giants; (*2*) mild barium stars; (*3*) Hyades giants; (*4*) Hyades giants from [26].

The Hyades giants merit further discussion. Estimates of the oxygen and nitrogen abundances in the atmospheres of F dwarfs of this young open cluster were obtained in [22], and indicated a N abundance exceeding the solar abundance by 0.3 dex. Takeda *et al.* [22] suggest that the N abundances in dwarfs correspond to their initial abundances; i.e., the cluster was formed from material with an enhanced nitrogen abundance. In this case, the N abundance in red giants could also exceed the initial abundance due to convection and the dredging-up of hydrogen-burning (CNO-cycle) products to surface layers. Table 3 presents N abundances in the atmospheres of the studied Hyades members collected from the literature [23, 24]. The N abundances of the Hyades red giants do exceed the value for normal giants somewhat (+0.3 dex), possibly due to an enhanced initial N abundance. This possibility is also supported by the spectra of bright Hyades giants possessing enhanced CN bands. Thus, the material from which the Hyades were formed probably had an enhanced nitrogen abundance, relative to iron. It seems likely that there was also an enhanced abundance of Ne, an element that is close to N in the periodic table. If this is true, we would expect a somewhat enhanced Na abundance: according to our general picture of the chemical evolution of the Galaxy, new-generation stars are formed from interstellar material enriched in the products of core nuclear reactions that have been lost by evolved stars. In this sense, the somewhat enhanced Na abundance compared to "normal" field giants (Fig. 2) could prove to be real.

Table 3. Relative nitrogen abundances in the atmospheres of Hyades red giants

Star	[N/Fe]		
	[23]	[24]	mean
κ Per*	–	+0.49	+0.49
γ Tau	+0.45	+0.51	+0.48
δ Tau	+0.39	+0.46	+0.42
ε Tau	+0.37	+0.59	+0.48
Mean value for all the stars			+0.47

* κ Per belongs to the Hyades moving group.

Al abundance. Table 2 indicates that the Al abundances of the studied stars are somewhat enhanced. We attempted to analyze these abundances using a plot for Al (Fig. 3) similar to that for Na. Figure 3 shows that the Al abundance increases, though slightly, with decreasing $\log g$, as is observed for Na. Note that there is no separation between the three groups of stars.

The spectrum of aluminum is not rich in lines that are strong enough for reliable measurements and possess trustworthy oscillator strengths. Most studies of Al abundances in the atmospheres of stars in the Galactic disk and halo are based on measurements of the λ3961 Å resonance line, and a few studies have worked with the λ6696/6698 and λ8772/8773 Å subordinate lines. However, it was shown in [23] that the resonance line exhibits considerable non-LTE effects whose strength depends strongly on metallicity. In addition, the equivalent widths of the λ3961 Å line can be seriously distorted by interstellar reddening. Our Al abundances are based on observations of the λ6696/6698 Å lines; for these, the non-LTE corrections are also positive, but have much lower values than the corrections for the λ3961 Å line, though they are also metallicity dependent [23]. Unfortunately, we could find only one paper [26] containing an estimate of the Al abundance in the atmosphere of a field supergiant derived from the λ6696/6698 Å lines. For this reason, we could not continue the relation of Fig. 3 towards lower $\log g$ values corresponding to supergiants with confidence, as we could for Na (Fig. 2) and Si (see below).

The question arises as to whether the weak dependence of the Al abundance on $\log g$ could be due to non-LTE effects that have not been taken into account. Such effects have been considered for various Al lines in [25]. For all the studied lines, the non-LTE abundance corrections were positive, with their values increasing with decreasing $\log g$ and with decreasing metallicity. In addition, this correction was smaller for the subordinate λ6697 and λ6698 Å lines than for the resonance lines, though it also increased with decreasing metallicity. Thus, taking into account the non-LTE correction could somewhat increase the spectroscopic [Al/Fe] values; the lower $\log g$, the larger the increase. Therefore, we conclude that the relation in Fig. 3 is not a consequence of non-LTE effects.

Aluminum could be formed on the main sequence in the Mg–Al hydrogen-burning cycle [24], in the reaction $^{26}Mg(p, \gamma)^{27}Al$, and, like Na, be dredged up to the surface by mixing during the star's evolution toward the red-giant stage.

Si abundance. Figure 4 shows a plot for Si, similar to those for Na and Al (Figs. 2 and 3). As for Na, the data for the giants and supergiants follow a single relation. We did not find any corrections for non-LTE effects for Si I lines in the literature. However, the exci-

tation potentials for the lower levels of the Si I lines used in our analysis are high (above 5.5 eV). Therefore, these lines are formed rather deeply in the stellar atmospheres, where the populations of energy levels are determined by collisions (this is especially true for levels close to the ionization limit, as is also true for Si II lines), and we do not expect large deviations from LTE. We thus conclude that the relation in Fig. 4 reflects the real situation. The mild barium stars and Hyades giants show good agreement with the relation.

Figure 4 also plots the data on Si abundances in the atmospheres of supergiants from [27]. Despite the large scatter, these data agree, on average, with our own data.

During hydrogen burning in the Mg–Al cycle, the reaction ^{27}Al(p, γ)^{28}Si (the so-called nuclear-leak reaction from this cycle; cf. [28], p. 187) also takes place. This reaction can enhance the Si abundance in deep layers on the main sequence, and first mixing can lead to an observed excess of Si in the atmospheres of giants.

Abundances of s-process elements. We found in our earlier papers [8, 9] that *s*-process elements are overabundant to various degrees in the atmospheres of red giants. Since rare earths are usually thought to result from consecutive slow neutron capture (the *s*-process), the discovery of excesses of these elements in the atmospheres of normal giants was somewhat unexpected. According to stellar-evolution theory, a sufficiently intense flux of neutrons is created during thermal pulses in the helium core—i.e., at later evolutionary stages—and abundance anomalies for *s*-process elements are usually observed in stars at later stages of their evolution, on the asymptotic giant branch.

To investigate the nature of this result, we plotted the overabundance of an element as a function of its solar abundance (Fig. 5). We were guided by the following logic: during the *s*-process (i.e., consecutive neutron capture with subsequent beta decay), the relative abundance increments should be greater for elements with lower original abundances. Of course, this suggestion does not have a very firm basis; however, such a tendency could well occur. The asterisks show the mean abundances for the nine normal (with no spectral peculiarities) red giants analyzed in this paper. The figure shows that there is indeed a trend for greater enhancement of the abundances for elements with lower original abundances. Note that the barium stars (crossed squares; the data are based on mean abundances for the three mild barium stars in our program) and the evolved globular-cluster red giants (circles) [29] share the same trend.

In this figure, the diamonds show the abundances for the Hyades red giants, which suggest a complete absence of overabundances for these elements. The differences between the Hyades stars and field stars may be due to the different ages of these two groups, which imply different degrees of convective mixing. In the young Hyades stars, mixing has not yet enriched the

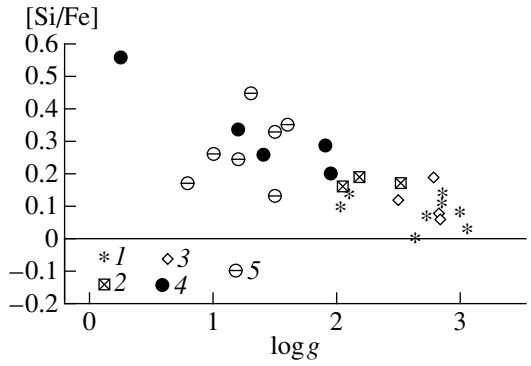

Fig. 4. Excess silicon abundance in the atmospheres of red giants and supergiants: (*1*) normal giants; (*2*) mild barium stars; (*3*) Hyades giants; (*4*) supergiants from [1–3]; (*5*) supergiants from [27].

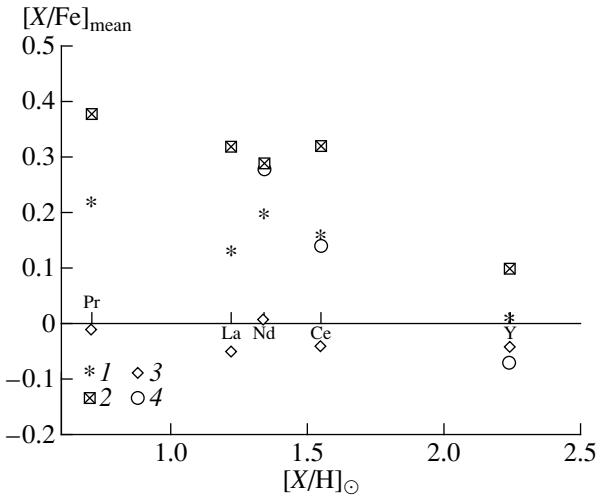

Fig. 5. Excesses of *s*-process elements in the atmospheres of red giants: (*1*) normal giants; (*2*) mild barium stars; (*3*) Hyades giants; (*4*) globular cluster giants from [32].

atmospheres in *s*-process elements. The field stars are much older, and their atmospheres demonstrate various degrees of enrichment in *s*-process elements.

Figure 5 suggests that the enrichment of stellar atmospheres in rare earths can already occur at the red giant stage, when the convective envelope is formed. These elements can originate in either the core or the shell source; i.e., in regions of active nuclear reactions.

The results of a spectroscopic analysis of the star 31 Aql presented in [30] support this conclusion. Since this star has an excess Fe abundance (+0.32 dex), it is young; according to [30], it is slightly evolved off the main sequence, and its convective envelope is beginning to expand. Overabundances of Na and Al, compared to the solar values, were found in the star's atmosphere, but the *s*-process elements remain slightly deficient (within the errors), in complete agreement with our results for the Hyades giants.

6. CONCLUSIONS

The chemical abundance anomalies we have found testify that, in addition to the CNO cycle, which is responsible for the observed anomalies of the CNO abundances, the Mg–Al and Ne–Na cycles are also active in the interiors of main-sequence stars. We observe the products of these cycles in the atmospheres of stars after they become red giants and, consequently, develop convective zones (the so-called first dredge-up). In addition, the abundance anomalies for *s*-process elements provide evidence for the presence of a substantial quantity of neutrons.

Usually, helium-burning reactions, such as $^{13}C(\alpha, n)^{16}O$ and $^{22}Ne(\alpha, n)^{25}Mg$, which occur at very high temperatures ($T \sim 2 \times 10^8$ K), are considered to be the main suppliers of neutrons. The corresponding high temperatures occur on the asymptotic giant branch. The observed overabundances of *s*-process elements are somewhat unexpected from this point of view. Photoneutron reactions, such as $^{13}C(\gamma, n)^{12}C$, $^{14}N(\gamma, n)^{13}N$, etc., which occur at comparatively low temperatures ($T \sim 10^7$–10^8 K) [31], could play an important role here. This problem certainly requires more detailed study. The absence of *s*-process element overabundances in giants of the Hyades, a young cluster, while these elements show appreciable excesses in field giants, clearly suggests an evolutionary factor for the observed dependence.

ACKNOWLEDGMENTS

This work was partially supported by the Russian Foundation for Basic Research (project code 97-02-17959). Observations of several stars were acquired with an SDS-9000 (Photometrics GmbH) CCD chip installed at the 2.6-m telescope of the Crimean Astrophysical Observatory thanks to grants from the International Science Foundation (R2Q000 and U1C000) and the ESO C&EE Program (A-05-067).

REFERENCES

1. A. A. Boyarchuk and M. E. Boyarchuk, Izv. Krym. Astrofiz. Obs. **63**, 66 (1981).
2. A. A. Boyarchuk and L. S. Lyubimkov, Izv. Krym. Astrofiz. Obs. **64**, 3 (1981).
3. A. A. Boyarchuk and L. S. Lyubimkov, Izv. Krym. Astrofiz. Obs. **66**, 130 (1983).
4. P. A. Denisenkov and V. V. Ivanov, Pis'ma Astron. Zh. **13**, 520 (1987) [Sov. Astron. Lett. **13**, 214 (1987)].
5. L. I. Antipova, S. V. Berdyugina, and I. S. Savanov, Astron. Zh. **72**, 855 (1995) [Astron. Rep. **39**, 761 (1995)].
6. A. A. Boyarchuk, L. I. Antipova, M. E. Boyarchuk, and I. S. Savanov, Astron. Zh. **72**, 864 (1995) [Astron. Rep. **39**, 770 (1995)].
7. A. A. Boyarchuk, I. S. Savanov, M. E. Boyarchuk, and L. I. Antipova, Izv. Krym. Astrofiz. Obs. **94**, 36 (1998).
8. A. A. Boyarchuk, L. I. Antipova, M. E. Boyarchuk, and I. S. Savanov, Astron. Zh. **73**, 862 (1996) [Astron. Rep. **40**, 783 (1996)].
9. A. A. Boyarchuk, L. I. Antipova, M. E. Boyarchuk, and I. S. Savanov, Astron. Zh. **77**, 96 (2000) [Astron. Rep. **44**, 76 (2000)].
10. A. A. Boyarchuk, L. I. Antipova, M. E. Boyarchuk, and I. S. Savanov, Astron. Zh. **75**, 586 (1998) [Astron. Rep. **42**, 517 (1998)].
11. D. F. Gray and K. Brown, Publ. Astron. Soc. Pac., 2000.
12. I. S. Savanov and Yu. Yu. Selezneva, Astrofizika **39**, 5 (1996).
13. R. L. Kurucz, Rev. Mex. Astron. Astrofis. **23**, 181 (1992).
14. S. T. Ridgway, R. R. Joyce, N. M. White, and R. F. Wing, Astrophys. J. **235**, 126 (1980).
15. N. Grevese and A. J. Sauval, Space Sci. Rev. **85**, 161 (1998).
16. R. A. Bell, K. Eriksson, B. Gustafsson, and A. Nordlund, Astron. Astrophys., Suppl. Ser. **23**, 37 (1976).
17. A. A. Boyarchuk, L. S. Lyubimkov, and N. A. Sakhibullin, Astrofizika **22**, 339 (1985).
18. A. A. Boyarchuk, I. Gubeny, J. Kubat, *et al.*, Astrofizika **28**, 343 (1988).
19. L. Mashonkina, N. Sakhibullin, and V. Shimanskiĭ, Astron. Zh. **70**, 372 (1993) [Astron. Rep. **37**, 192 (1993)].
20. S. A. Korotin and T. V. Mishenina, Astron. Zh. **76**, 611 (1999) [Astron. Rep. **43**, 533 (1999)].
21. P. A. Denisenkov, Pis'ma Astron. Zh. **14**, 1023 (1988) [Sov. Astron. Lett. **14**, 435 (1988)].
22. Y. Takeda, S. Kawanomoto, M. Takeda-Hidai, and K. Sadakane, Publ. Astron. Soc. Jpn. **50**, 509 (1998).
23. D. L. Lambert and L. M. Ries, Astrophys. J. **248**, 228 (1981).
24. R. G. Gratton, Astron. Astrophys. **148**, 105 (1985).
25. D. Baumüller and T. Gehren, Astron. Astrophys. **325**, 1098 (1997).
26. P. R. Warren, Mon. Not. R. Astron. Soc. **161**, 427 (1973).
27. V. V. Smith and D. L. Lambert, Mon. Not. R. Astron. Soc. **227**, 563 (1987).
28. *Essays in Nuclear Astrophysics*, Ed. by C. Barnes, D. Clayton, and D. Schramm (Cambridge Univ. Press, Cambridge, 1982; Mir, Moscow, 1986).
29. R. G. Gratton and G. Contarini, Astron. Astrophys. **283**, 911 (1994).
30. T. V. Mishenina, Astron. Astrophys., Suppl. Ser. **119**, 321 (1996).
31. T. G. Harrison and T. W. Edwards, Astrophys. J. **187**, 303 (1974).
32. B. J. Armosky, C. Sneden, G. E. Langer, and R. P. Kraft, Astron. J. **108**, 1364 (1994).

Translated by N. Samus'

Astronomy Reports, Vol. 45, No. 4, 2001, pp. 309–318. Translated from Astronomicheskiĭ Zhurnal, Vol. 78, No. 4, 2001, pp. 359–369.

Emission Lines of the Red-Dwarf Flare Star EV Lac: Stellar Flares

É. A. Baranovskiĭ, R. E. Gershberg, and D. N. Shakhovskoĭ

Crimean Astrophysical Observatory, National Academy of Sciences of Ukraine, p/o Nauchnyĭ, Crimea, 334413 Ukraine

Received March 28, 2000

Abstract—We present equivalent widths and profiles for H_α, H_β, H_γ and He I λ4471 Å emission lines obtained in observations of the flares of EV Lac made at the Crimean Astrophysical Observatory in 1994 and 1995. Our semi-empirical modeling of the flares gives insight into the structure of the emitting regions, including a temperature plateau, and also into the physical parameters, size, and location of the star's relatively quiescent chromosphere. © *2001 MAIK "Nauka/Interperiodica".*

1. INTRODUCTION

In the course of sporadic flares in red dwarf UV Ceti stars, the hydrogen and calcium emission lines in their spectra undergo substantial variations: they rapidly become stronger and their profiles become appreciably broader. Since the detection of broad wings of the hydrogen-line profiles in the flare spectra, two mechanisms have been proposed to explain them: pressure (Stark broadening), or the motion of flare matter (Doppler broadening) [1–9]. However, neither of these mechanisms is able to describe the entire collection of observational data on its own. For example, both at the phase of maximum brightness and in the decay stage of the March 2, 1970 flare of AD Leo, the simultaneously determined FWHMs for H_β, H_γ, H_δ, and H_ϵ + H turned out to be rather similar: 10–13 Å [10]. A similar closeness of the FWHMs for H_β, H_γ, H_δ, and H_ϵ + H was detected in the decay stage of the February 18, 1971 AD Leo flare [11]. The similarity of the $\Delta\lambda$ values corresponds to the variability of $\Delta\lambda/\lambda$ for these lines, which suggests that thermal or macroscopic movements are insufficient to explain the observed profiles, and/or that the flare has substantial optical depths in these lines. However, this conclusion is not very firm due to the appreciable instrumental profile width (exceeding 6 Å).

On the other hand, the considerable broadening of hydrogen lines and the simultaneous absence of broadening in the Ca II K line during the September 8, 1979 flare of UV Cet [1] was initially interpreted as a manifestation of the Stark mechanism. However, in their more detailed analysis of these observations, Eason *et al.* [12] failed to find adequate agreement between the data and calculated H_α Stark profiles, leading them to the idea that the regions of the formation of the calcium and hydrogen lines might be different. Eason *et al.* [12] also suggested that a rising flow of very hot gas from the chromosphere was responsible for the broad H_α wings.

Further, analyses of spectra of the March 4, 1985 flare of YZ CMi [3, 4, 13] indicated that neither the H_γ nor H_δ profiles could be fit well by one or two Stark profiles, although they can be successfully described by a sum of two Gaussians with appreciably different widths. The wider Gaussian, which reproduces the wings of the profile, corresponds to motion with velocities of hundreds of km/s. Strictly speaking, the decomposition of the observed profiles into Gaussian components does not give a basis for direct modeling of the flare. The decomposition is nonetheless useful for understanding the line broadening during flares, since it provides estimates for parameters that must be reproduced by the profile-formation mechanism. The decomposition of observed profiles into Gaussian components has become quite widespread [5, 7, 8, 12, 14, 15].

All these comparisons between observed and predicted profiles broadened by pressure effects were made in accordance with calculations carried out by Vidal *et al.* [16]. However, these calculations assume an optically thin radiating medium, while stellar flares are definitely optically thick in the first terms of the Balmer series. The flat tops of the hydrogen-line profiles with their slightly reduced intensities at the line center [11, 12] provide direct evidence for appreciable optical depths in these lines, whatever the mechanism for the formation of the broad wings. Indeed, as was recently shown by Sobolev and Grinin [9], taking into account the appreciable line optical depth can yield rather broad Stark profiles, and, in particular, can successfully reproduce the broad wings of the H_β profile detected during the September 1, 1992 flare of EV Lac [15].

Here, we present a quantitative analysis of emission lines in flare spectra of EV Lac obtained at the Crimean Astrophysical Observatory (CrAO) during international coordinated observing campaigns in 1994 and 1995. The analysis is based on the technique described in [17].

1063-7729/01/4504-0309$21.00 © 2001 MAIK "Nauka/Interperiodica"

2. OBSERVATIONS

All the spectral observations of EV Lac at the CrAO were made with the 2.6-m Shain Telescope equipped with CCD spectrographs. In 1994, we obtained spectra at blue to green wavelengths, including the Balmer H_β and H_γ lines and several helium and metallic lines. In 1995, we obtained spectra at red wavelengths, including the H_α line. The observations are described in detail by Baranovskiĭ *et al.* [17].

2.1. H_β and H_γ Lines

In 1994, we carried out spectral monitoring of EV Lac at 4190–5480 Å with a resolution of 4 Å. Using simultaneous photometric monitoring data, we selected from the 179 spectrograms obtained 20 corresponding to the active state of the star. We selected spectra with the largest equivalent widths W_{H_β} and the maximum values of $FWQM_\beta$; i.e., the full width of the H_β line at one-quarter its maximum intensity.

The first five of the 20 selected spectra correspond to relatively brief flares at 18:48, 19:17, and 23:32 UT on August 28, 1994 and 20:39 UT on August 29, 1994 and to the double-peaked flare at 19:30 UT on August 30, 1994. The remaining 15 spectrograms cover the three-hour active state of the star on August 31, 1994 at 20:30–23:30 UT, which included at least eight rapid flares of various amplitudes and the slow decay of the star's brightness after the double flare at 21:21 UT.

During six nights of observations in the quiescent state of the star, the values for W_{H_β} were 4.4–5.0 Å, while the values for the selected spectra were 10.2–20.9 Å; W_{H_γ} was 8.6–12.5 Å for quiescence and 16.0–28.9 Å in the active state. Thus, the effect of the flaring on the measured equivalent widths can clearly be seen. For the selected spectra obtained during the active state, the correlation coefficient between the measured equivalent widths was fairly high: $r(W_{H_\gamma}, W_{H_\beta}) = 0.84$. The widths of these lines were even more closely correlated at the quarter-maximum level: $r(FWQM_\beta, FWQM_\gamma) = 0.93$.

Profiles of emission lines in the active state obtained by subtracting the mean quiescent-state spectra for the corresponding nights from the selected spectra (the procedure used is described by Abdul-Aziz *et al.* [15]) indicated essentially the same close correlation between the line widths—$r(FWQM_\beta, FWQM_\gamma) = 0.90$—despite the fact that the FWQM for these "pure" flare spectra did not always exceed the corresponding widths of the quiescent profiles and, in a number of cases, were rather close to the instrumental width. However, when these "pure" flare profiles were fit by sums of narrow and broad Gaussians, the widths of both the narrow and broad components of the H_β and H_γ lines are not correlated with each another. Apparently, this means that the estimates for the Gaussian widths are unstable due to the low spectral resolution of the original data. Nonetheless, the fractions of the total radiation in lines contained in the broad Gaussians proved to be rather closely correlated: $r((E_{wide}/E_{tot})_\beta, (E_{wide}/E_{tot})_\gamma) = 0.80$.

2.2 H_α Emission Line

In 1995, spectral monitoring of EV Lac was carried out near H_α with spectral resolution 0.37 Å during the first night and 0.74 Å during the remaining four nights. Based on simultaneous photometric monitoring, we selected 14 of 64 spectrograms corresponding to the active state of the star: four spectra with the largest W_{H_α} values correspond to the flare brightness maximum, three to decay phases, and the others to a prolonged period of activity on September 4, 1995, similar to the extended period of line emission at blue and green wavelengths on August 31, 1994.

During the five nights of CrAO observations, the W_{H_α} values for the quiescent state of the star varied from 3.5 to 5.3 Å and were in counterphase with the total *V*-band brightness of the star, whose variations were due to the irregular spotting of the stellar surface. For the spectra in the active state, W_{H_α} varied from 4.7 to 10.6 Å. The widths of the H_α line profiles were FWHM = 1.3 Å and FWQM = 1.5–1.8 Å in the quiescent state, and FWHM = 1.3–1.5 Å and FWQM = 1.6–2.0 Å in the active state. Thus, in the active state, H_α is less enhanced than H_β and H_γ, possibly due to a larger optical depth in the H_α line. Nonetheless, owing to the higher spectral resolution achieved for this line, "pure" profiles for the active state obtained by subtracting the mean quiescent spectra on the corresponding nights from the selected active-state spectra were determined with higher certainty. When these "pure" flare profiles were fit by sums of narrow and broad Gaussians, the widths of the broad components were 4.0–5.8 Å. It is evident that these estimates (which are factors of five to eight higher than the instrumental profile width) are trustworthy.

2.3. Helium Emission Lines

During the 1994 coordinated EV Lac campaign, we detected several He I lines and the He II λ4686 Å line in the active state of the star at blue to yellow wavelengths. The behavior of these emission lines was very different: the correlation of the rapid onset of the flare in the *U* band with that in the He I λ4471 Å line was tighter than the correlation with the Balmer lines. In addition, we did not find any significant correlation between the emission in the hydrogen lines and the He II λ4686 Å line.

The relative faintness of the helium lines prevents reliable estimation of quantitative parameters from individual spectrograms. For this reason, we summed all the "pure" spectra for the active state of the star. Figure 1 presents the normalized summed profile for the strongest helium

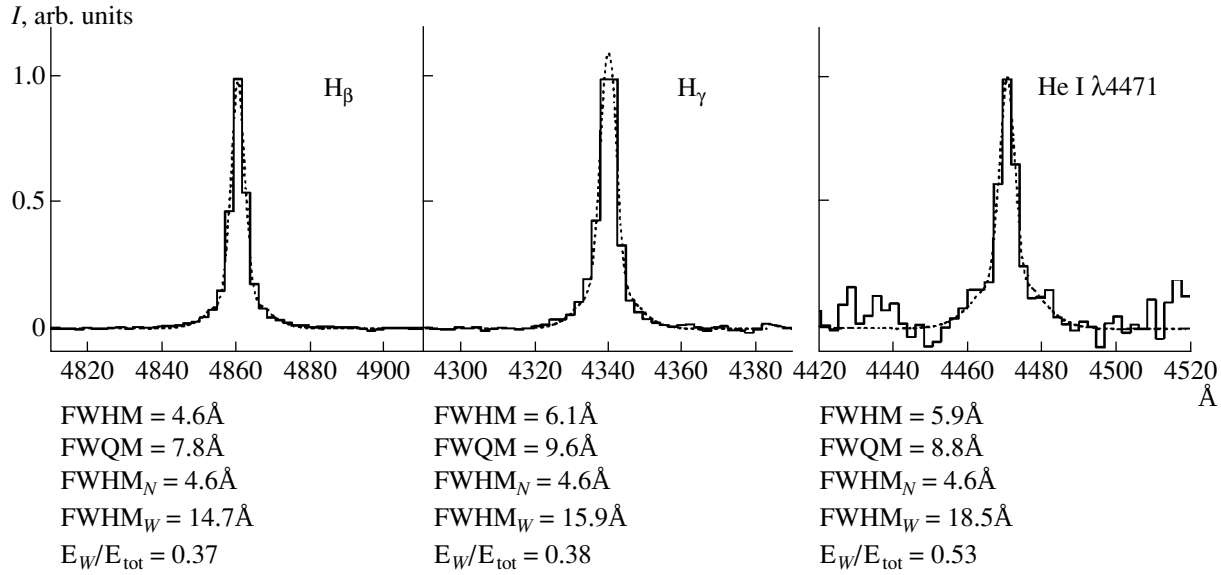

Fig. 1. Profiles of emission lines obtained by summing "pure" spectra of EV Lac in active states. Under each profile, the widths of the summed profile at half- and quarter-maximum intensity (FWHM and FWQM), the widths at half-maximum intensity for the narrow and broad Gaussians into which the profile is decomposed (FWHM$_N$ and FWHM$_W$, respectively), and the fraction of the broad Gaussian energy in the total profile E_W/E_{tot} are marked.

line λ4471 Å. The same figure presents corresponding summed profiles for the H_β and H_γ lines. We can see that all three of these profiles can be well fit by sums of two Gaussians with different widths; the widths of the narrow Gaussians are the same for all three profiles. Apparently, this indicates that the instrumental profile determines the form of these narrow components. The widths of the broad Gaussian of the neutral helium line are somewhat larger than those for hydrogen lines. This means that both Doppler broadening, which is related to macroscopic motions that should be the same for all spectral lines, and temperature Doppler broadening, which should be appreciably smaller for the helium line than the hydrogen lines, are of little importance in the formation of the broad Gaussian components.

Observations of He II λ4686 Å emission in the flares of UV Cet stars are comparatively rare. We note two new facts demonstrated by the CrAO observations of EV Lac. First is the already mentioned absence of any significant correlation between the intensities of this helium line and of the Balmer lines: the He II λ4686 Å line was observed both near the maxima of intense, rapid flares and during their subsequent slow decay; this is apparently the first time such prolonged emission in this line has been observed. Secondly, we have detected for the first time the splitting of this line into two components with roughly equal intensities in the combined spectrum.

The red component has the same radial velocity as the other emission lines, while the blue component is displaced towards shorter wavelengths, providing direct evidence for an upward motion of the emitting material with a velocity of about 400 km/s. It is important that, in some spectrograms, only the red or only the blue component is seen, while some spectra display both components. To order of magnitude, 400 km/s is close to the velocity detected in the impulsive phase of the AU Mic flare of September 3, 1991 observed with the Hubble Space Telescope [18]. In that case, however, the strengthening of the red wing of the L_α line lasted only three seconds, and was probably associated with a proton beam directed from the area of primary energy release towards the photosphere. The blue component of the He II line detected in the CrAO observations probably provides the first direct evidence for dynamical processes in the upper chromosphere, which can result in events similar to solar transients; i.e., macroscopic ejections of material into circumstellar space.

3. SEMI-EMPIRICAL MODELS FOR THE EV LAC FLARES

In this section, we apply the algorithm for modeling quiescent stellar chromospheres developed by Baranovskiĭ *et al.* [17] to spectral observations of stellar flares for the first time. Some justification is needed here.

This scheme for calculating emission line profiles in a quiescent chromosphere assumes that the radiating matter is in hydrostatic equilibrium. Since the turbulent velocity enters into the calculations, this assumption is natural for quiescent chromospheres, but is not obvious when applied to stellar flares, where we see velocities of many tens of km/s. Nevertheless, such models for flares can be justified by the following arguments.

There is a long-standing tradition of using this approach to describe solar flares. We consider two examples below.

In the study of Machado *et al.* [19], the use of an equation of hydrostatic equilibrium in the flare calculations is justified on the grounds that "the velocity fields of chromospheric flares are to a great extent unknown." This doubtful argument is even more true of stellar flares. Nonetheless, following the model for the quiescent solar spectrum developed by Vernazza *et al.* [20–22], Machado *et al.* [19] successfully fit both the line and continuum spectra of solar flares at wavelengths from 300 to 1700 Å, the Mg II and Ca II resonance doublets, and the Ca II infrared triplet. According to their semi-empirical models, the temperature minimum in a flare is located deeper and the temperature itself is higher compared to both the quiescent Sun and to active regions, while the electron temperature and electron density in the regions of formation of the Lyman lines and continuum are increased. The transition zone is also deeper, encompassing layers with higher density.

Recently, Fang *et al.* [23] have constructed a semi-empirical model for a white-light flare that likewise assumes hydrostatic equilibrium of the radiating matter. Both the flares themselves and the types of original observational data considered in the studies of Machado *et al.* [19] and Fang *et al.* [23] differ substantially; in spite of this, the temperature distributions with height obtained in [23] are very close to those in one of the models constructed in [19]. All hydrostatic models assume stationarity and fulfillment of radial equilibrium conditions.

On the other hand, a gas-dynamical model for these processes has been developed in parallel with hydrostatic-equilibrium models for solar flares, starting with the study of Kostyuk and Pikel'ner [24]. The central idea here is the formation of a pressure jump in place of the initial impulsive energy release, from which intense gas-dynamical perturbations propagate down into the photosphere and up into the corona. However, the fulfillment of the condition of radial equilibrium in this type of model is not obvious. This concept of solar flares was soon applied to flares in red dwarfs [25].

It has been shown in the framework of gas-dynamical models of stellar flares that the perturbation that originates immediately after the impulsive heating and propagates downwards forms condensations that are the main source of optical radiation for the flare; these propagate in a quasi-stationary mode, and the physical conditions inside them vary slowly [26]. This latter circumstance justifies the application of radial-equilibrium conditions in these models, and explains the success of this approach in the interpretation of the observed parameters of solar flares. Naturally, the integration of the concepts of gas-dynamical and radial-equilibrium modeling, as was recently done for the first time by Katsova *et al.* [27], should yield the best approximations to observed flare parameters.

Let us turn again to the 1994 and 1995 CrAO spectral observations of EV Lac flares. For further quantitative modeling, we have selected six spectra from those obtained in EV Lac's active state and described by Abranin *et al.* [28]: Nos. 4 and 6 of 1994 at blue to green wavelengths, associated with medium-amplitude flares; No. 15 of 1994, associated with the slow decay of a prolonged active state; and Nos. 9, 10, and 11 of 1995 at red wavelengths, associated with the decay phase of an intense flare (the numeration of the flares corresponds to Figs. 9 and 13 in [28]). Figure 2 presents *U*-band light curves for all these flares and H_α and H_β equivalent widths determined at the times marked by the horizontal intervals. Table 1 presents the parameters for these events from the study of Abranin *et al.* [28] and brightnesses of the star averaged over spectral exposures calculated by I.Yu. Alekseev from his simultaneous *UBVRI* observations carried out with the AZT-11 telescope. Table 1 also presents the equivalent widths and total widths at half- and quarter-maximum of the emission lines in the flare spectra.

When the algorithm for calculating the parameters of emission lines in quiescent chromospheres described by Baranovskiĭ *et al.* [17] is applied to flare spectra, an important unknown supplementary parameter must be introduced into the calculations: the area of the flare. Therefore, we carried out the calculations according to the following scheme. We adopted as a basic model for EV Lac the model calculated by Baranovskiĭ *et al.* [17], in which one-third of the stellar surface is covered by active regions and the remaining two-thirds does not contribute to the emission. To this we add the flare radiation, which occupies some fraction of the active-region surface area (determined as part of the calculations). The combined profile and equivalent widths are matched to the observed values using a trial-and-error method.

We first considered the H_α profiles detected during the flare of September 4, 1995. Assuming that the temperature plateau (known to exist in the solar chromosphere and detected by us [17] in the quiescent chromosphere of EV Lac) can form only in a sufficiently steady-state medium, we initially performed our flare model calculations without including this plateau. However, these calculations were not successful: when matching the H_α profile, the intensity of the flare continuum was too low (we could enhance the continuum by increasing the temperature, but, in this case, the line would have become too broad). In addition, such models overestimate the ratio $\Delta U/\Delta B$ due to the large Balmer jump. Therefore, we concluded that one of the necessary conditions for successful reproduction of the observations is incorporating an extended temperature plateau in the flare model. Note that a temperature plateau is also included in gas-dynamical flare models [29].

Thus, we specified a temperature plateau in the range 5000–8000 K followed by a rapid temperature increase. We specified the density variation with height according to the condition of hydrostatic equilibrium. We varied the extent of the plateau (by varying its lower boundary from $\log m = -3.5$ to $\log m = -0.5$; here and below, m is in g/cm^2), the temperature gradient across the

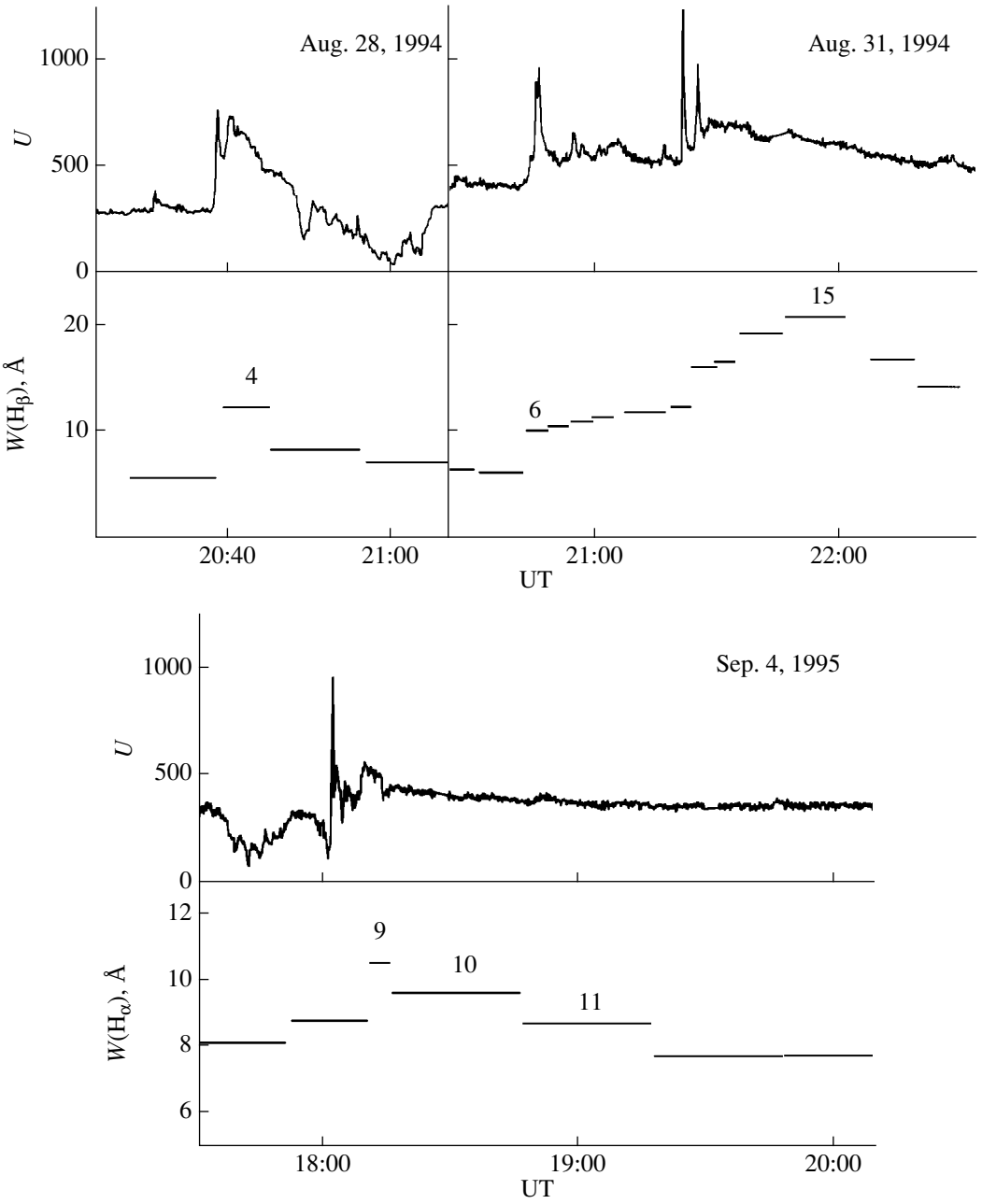

Fig. 2. Light curves of the EV Lac flare in the *U* band and H_α and H_β equivalent widths measured within the times marked by the horizontal intervals.

plateau, and the total density in the region of the plateau (from 10^{11} to 2×10^{16} cm^{-3}). The temperature gradient across the plateau should be very small, since its increase leads to an increase in $\Delta U/\Delta B$; attempts to decrease this ratio by raising the upper boundary of the plateau result in unacceptably small intensities for the He lines.

Models with a fixed extent for the plateau were calculated for various densities; the temperature within the plateau was chosen to best match the calculated and observed profiles and equivalent widths, both at the line center and in the wings (such matching can occur only for a certain degree of filling of the active region by the flare). In this way, for a given fixed plateau extent and density, its temperature and filling factor are determined unambiguously in the course of matching the calculated and observed H_α profiles and equivalent widths. As in the model calculations for the quiescent chromosphere, we assumed that neither emission nor absorption in H_α is present outside of active regions on the stellar disk.

We derived a collection of models closely fitting the H_α profiles and equivalent widths, but differing in the

Table 1. Parameters of the spectrum of the active state of EV Lac

Flares of August 29 and 31, 1994

flare number	times of beginning and end of exposure, UT	amplitude			W_λ, Å		FWHM, Å		FWQM, Å	
		ΔU	ΔB	ΔV	β	γ	β	γ	β	γ
4	$20^h39^m38^s$–$20^h45^m10^s$ August 29	$0\overset{m}{.}80$	$0\overset{m}{.}20$	$0\overset{m}{.}09$	14.0	–	6.5	8.1	11.6	16.2
6	$20^h43^m06^s$–$20^h48^m19^s$ August 31	0.58	0.13	0.06	10.2	18.6	4.4	6.9	10.1	11.0
15	$21^h46^m47^s$–$22^h01^m08^s$ August 31	0.43	0.13	0.05	20.9	26.6	3.5	4.5	5.7	6.4

flare of September 4, 1995

flare number	times of beginning and end of exposure, UT	amplitude			W_{H_α}, Å	FWHM, Å	FWQM, Å
		ΔU	ΔB	ΔV			
9	$18^h11^m11^s$–$18^h15^m54^s$	$0\overset{m}{.}31$	$0\overset{m}{.}11$	$0\overset{m}{.}03$	10.6	1.47	1.95
10	$18^h16^m31^s$–$18^h46^m31^s$	0.14	0.06	0.01	9.6	1.50	2.01
11	$18^h47^m16^s$–$19^h17^m16^s$	0.07	0.03	0.01	8.7	1.47	1.94

calculated Δm_{UBV}, Balmer decrement, and filling factor. In addition, it became clear that models with shallow plateaus ($\log m < -1.6$) do not yield sufficient continuum emission, and, as the plateau rises, the size of the flare approaches the total size of the active regions, which is not realistic. Models with a deeper lower boundary for the plateau yield the ratios $\Delta U : \Delta B : \Delta V$ that are closer to the observed values than those obtained for a shallower plateau. The calculated Balmer decrements depend primarily on the temperature gradient adjacent to the upper part of the plateau, and also on the temperature and density in the plateau. No information on the other Balmer lines is available for the 1995 flares. Taking into account, however, that the ratio of the H_β and H_γ intensities during the 1994 flares was roughly 0.93 and that the observations of the December 11, 1965 flare of EV Lac [30] indicate that this value was about 0.9, we attempted to obtain similar values for this ratio in the course of our model selection. Taking into account all the above factors, for spectra Nos. 9, 10, and 11, we chose models with a lower plateau boundary $\log m > -1.1$, where m exceeds the corresponding value in our model for the unperturbed chromosphere by approximately an order of magnitude, and with the logarithm of the total density in the plateau varying from 13.0 to 15.0.

Thus, taking into consideration the H_α line profiles and equivalent widths during the flare, as well as the *UBV* brightnesses of EV Lac, suggests the presence, as in the quiescent chromosphere, of an appreciable temperature plateau (the characteristic optical depth at the line center is 10^2–10^3, and the characteristic electron density is 10^{12}–10^{13} cm^{-3}).

In 1994, we observed EV Lac at short wavelengths with lower spectral resolution, and the broad instrumental profile essentially rules out the possibility of studying the line wings. Therefore, our matching of the models to the observations was based on the H_β and H_γ equivalent widths and the values for ΔU, ΔB and ΔV. As for 1995 flare, models without a temperature plateau or with a plateau at a small depth proved unacceptable, since they overestimated ΔU and the filling factors. The calculations demonstrated that the restrictions imposed on the lower plateau boundary ($\log m > -1.1$) and the logarithm of the total density (>13.6) remain valid for the 1994 flares. We varied the temperature and density in the region of the plateau and the position of its lower boundary to match the calculated and observed I_{H_β}/I_{H_γ} ratios and the relations between the *UBV* amplitudes. We left the low turbulent velocity in the region of formation of Balmer lines (2 km/s) derived from the widths of the H_α profiles in the 1995 EV Lac flare. However, we were not able to explain the broad wings of the H_β and H_γ lines, even with a substantial increase in the density in the plateau region to 10^{16} cm^{-3}. As noted above, Sobolev and Grinin [9] were able to fit the wings of the H_β line profile for the intense flare of EV Lac of September 1, 1992 observed with the CrAO Shain Telescope in the framework of a Stark broadening theory. However, they fit only the far wings ($|\Delta\lambda| > 8$ Å) rather than the entire line profile and absolute intensity.

The intensity of the He I λ4471 Å line depends on that part of the model where $T > 10\,000$ K. We fitted the calculated and observed profiles for all observation times by varying the temperature dependence with height in this region, which leaves the Balmer line profiles virtually unaffected.

Figure 3 presents emission-line profiles calculated using the models. Table 2 presents the parameters for all of our models of EV Lac flares; note that the filling factors ff in the ninth column refer to the entire surface of the star, and the three last columns present ranges for values in the temperature plateau. The fit of our models

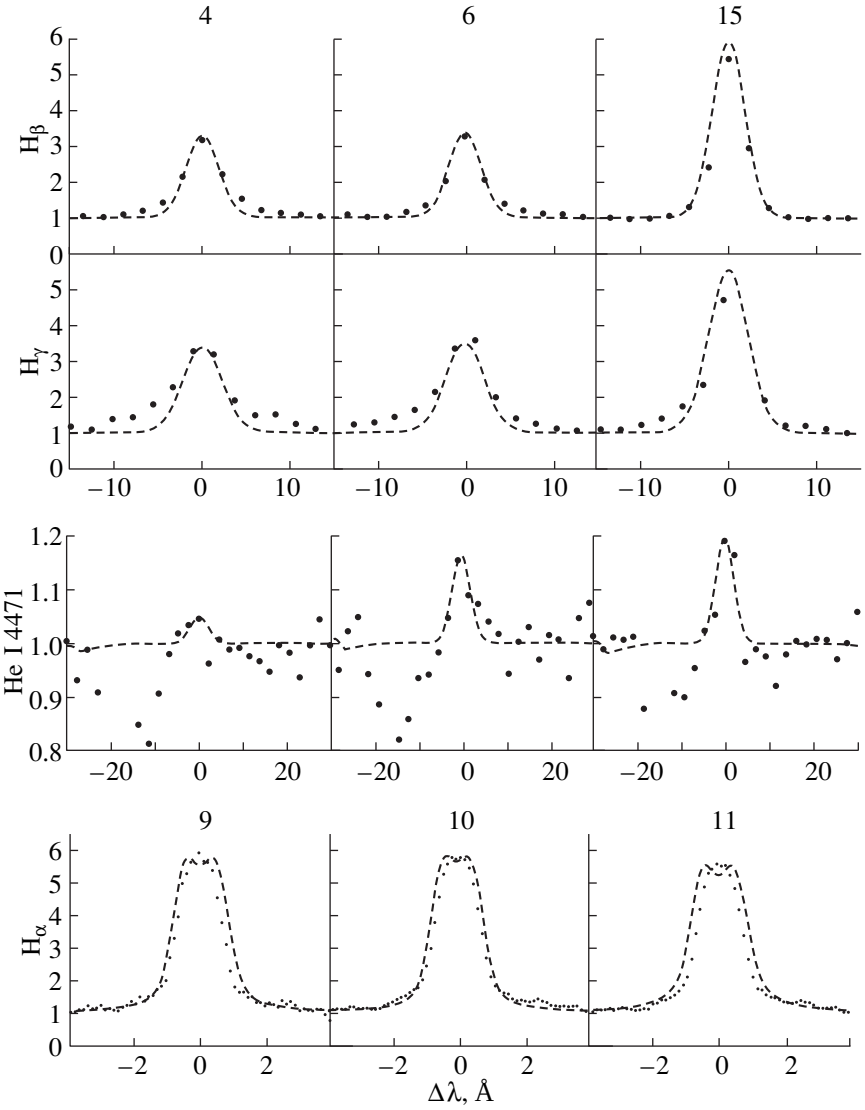

Fig. 3. Profiles of emission lines for individual flares (circles) and the fitted semi-empirical models (dashed lines).

to the observations can be characterized as follows: the equivalent widths of the H_α and H_β lines are matched to within 25 to 1.4%, the FWHMs for the same lines are matched to within 22 to 6%; and the values in Tables 1 and 2 for ΔU differ by from 0.00 to 0.10, for ΔB from 0.00 to 0.01, and for ΔV from 0.00 to 0.02. Figure 4 presents our models for all the flares listed in Table 1, and also the model for active regions occupying one-third of the stellar surface [17] (curve EV3). We can see from Fig. 4 that the main difference between the models for the quiescent chromosphere and flares of EV Lac is the depth of the temperature plateau and the increase of the electron density in the layers responsible for the Balmer line emission (by approximately an order of magnitude).

Let us compare our results with previous estimates of flare parameters for UV Ceti stars. Analysis of the emission Balmer decrements carried out for a number of such flares based on the concept of moving envelopes yielded $n_e \sim 10^{12}$–10^{14} cm^{-3} for $\tau_{L_\alpha} = 10^4$–10^5. Applying Balmer decrement theory for a fixed medium to several flares of EV Lac and other red dwarfs, Katsova [31] estimated the flare electron density near maximum brightness to be 10^{14} cm^{-3}, and noted that the transition to steeper decrements in the course of the flare decay could be due to a decrease in n_e (in her models, $\tau_{L_\alpha} = (2\text{–}3) \times 10^6$). The flares we have studied do not include any with large amplitudes, so that the estimates n_e can be considered consistent.

Recently, Mauas and Falchi [32] constructed a semi-empirical hydrostatic model for two times during the intense April 12, 1985 flare of AD Leo, described by Hawley and Pettersen [33]. They considered the fluxes

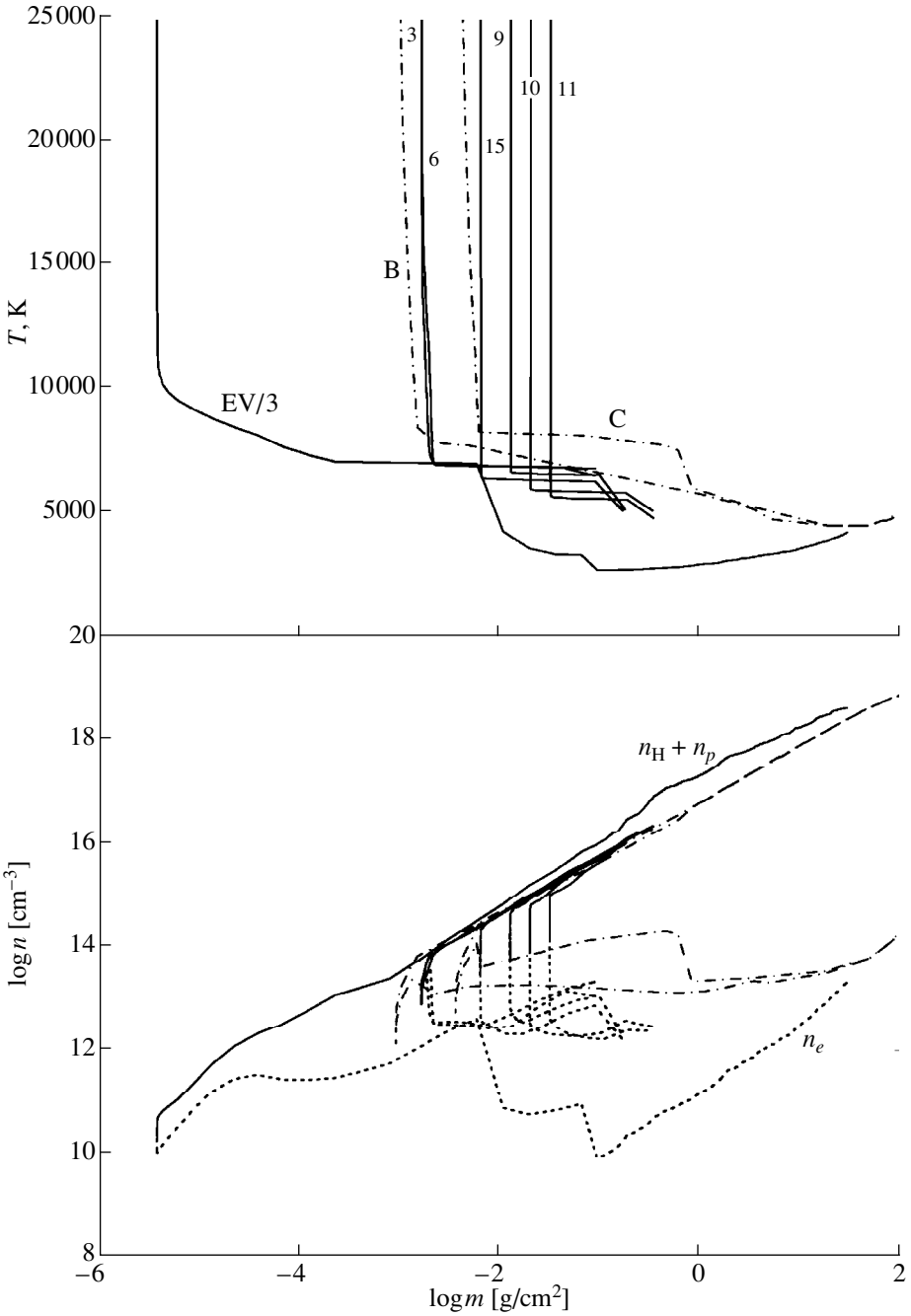

Fig. 4. Semi-empirical models for the EV Lac flare. Numeration for the models corresponds to that of the flares in Table 1. Curve EV3 corresponds to the model of active regions on EV Lac calculated by Baranovskiĭ *et al.* [17], and curves B and C to the models of Mauas and Falchi [32] calculated to reproduce the decay phase of an intense flare of AD Leo.

in the *UBVR* bands and in the H_β, H_γ, H_δ, H_8, Ca I λ4227 Å, and K Ca II lines 15 and 20 min after the onset of the flare. Calculations were carried out for independently chosen filling factors. The models of Mauas and Falchi [32] are also presented in Fig. 4: curves B and C correspond to filling factors of 5 and 1%. The model with the flare occupying 5% of the stellar surface gives the best fit to the spectral features originating in the upper chromospheric layers, whereas the model with the flare occupying 1% of the stellar surface better fits features originating at larger depths. In this latter model, a temperature plateau near 8200 K extending from $\log m = -1.1$ to –2.3 can clearly be seen. Precisely this model provided the best consistency between the observed and calculated flare continuum. Observations made 20 min after the onset of the flare, when the continuum had appreciably decayed, were fit by a model with even smaller area. Comparing the models in Fig. 4 and the numerical

Table 2. Flare model parameters

Flare number	ΔU	ΔB	ΔV	$\log\tau_{L_\alpha}$	τ_{H_α}	τ_{H_β}	τ_{H_γ}	ff, %	$\log m$ [g/cm^2]	$\log(n_H + n_P)$ [cm^{-3}]	$\log n_e$ [cm^{-3}]	T, K
4	$0\overset{m}{.}70$	$0\overset{m}{.}19$	$0\overset{m}{.}08$	9.43	2400	340	120	3.1	–1.0	13.9–15.7	12.5–13.3	6770–6910
6	0.61	0.13	0.06	9.43	2150	300	100	2.5	–1.0	13.9–15.7	12.4–13.1	6500–6900
15	0.46	0.13	0.06	9.43	880	120	42	4.4	–0.9	14.3–15.7	12.3–12.9	6200–6500
9	0.30	0.11	0.05	9.73	1700	240	80	2.5	–0.8	14.6–16.0	12.6–13.1	6500–6800
10	0.14	0.06	0.03	9.73	420	60	20	2.0	–0.7	14.7–16.1	12.3–12.6	5800–6000
11	0.11	0.03	0.015	9.8	190	27	9	1.3	–0.7	14.9–16.1	12.2–13.1	5500–5800

results of Mauas and Falchi [32] with the data of Table 2, we can see a significant divergence in the lower chromosphere, since Mauas and Falchi [32] considered an intense flare with the perturbation reaching the upper layers of the photosphere. Note the unexpected resemblance between our models and those of [32] with regard to the characteristic size of the flares and the presence of a temperature plateau and its depth, in spite of the fact that the two studies considered flares in different stars, using different initial data and independent computation codes.

4. CONCLUSIONS

Hydrostatic models for the 1994 flare of EV Lac based on the equivalent widths of the H_β, H_γ, and He I λ4471 lines and *UBV* brightnesses, and also models for three phases of a 1995 flare based on the H_α profiles and equivalent widths and $\log m \sim -1$ brightnesses, indicate that a temperature plateau occurs both in the structure of the flares and in the quiescent chromosphere. Its lower boundary is at a depth of $\log m$ –1, whereas the upper boundary varies from $\log m$ –3 to –2 for different flares. The temperatures in the plateau region are close to 6000–7000 K, the total density is 10^{14}–10^{16} cm^{-3}, and the electron density is 3×10^{12}–2×10^{13} cm^{-3}. Thus, the structures responsible for the flare hydrogen emission lines are formed deeper than the temperature plateau of the quiescent chromosphere and are less extended in depth, but have larger electron and total densities; the upper boundary of the flare temperature plateau is at a height of 200–300 km, whereas the height in the quiescent chromosphere is 700 km, and in the solar chromosphere is 1800 km. The flares studied occupy 1–4% of the surface area, whereas H_α flares on the Sun cover 0.1–0.2% of its area; however, taking into account the fact that the Sun is a factor of three larger in size than the other stars studied, the characteristic linear sizes of the various flares prove to be similar.

ACKNOWLEDGMENTS

We are deeply grateful to I.Yu. Alekseev, who kindly presented us with photometric data on the flares of EV Lac, Dr. A. Falchi for computer-readable data on the temperature structure of the models for the AD Leo flares, and Drs. M.A. Livshitz and M.M. Katsova for useful comments. The acquisition of the observations used in our study was partially supported by the International Science Foundation (projects R2Q000 and U1C000) and the C&EE ESO Program (project A-05-067).

REFERENCES

1. M. S. Giampapa, in *IAU Colloquium 71: Activity in Red-dwarf Stars*, Ed. by P. B. Byrne and M. Rodonó (Reidel, Dordrecht, 1983), p. 223.
2. P. P. Petrov, P. F. Chugaĭnov, and A. G. Shcherbakov, Izv. Krym. Astrofiz. Obs. **69**, 3 (1984).
3. J. G. Doyle and P. B. Byrne, in *Proceedings of the 5th Cambridge Workshop on Cool Stars, Stellar Systems, and the Sun*, Ed. by J. L. Linsky and R. E. Stencel; Lect. Notes Phys. **291**, 173 (1987).
4. J. G. Doyle, C. J. Butler, P. B. Byrne, and G. H. J. van den Oord, Astron. Astrophys. **193**, 229 (1988).
5. R. D. Robinson, in *IAU Colloquium 104: Solar and Stellar Flares*, Ed. by B. M. Haisch and M. Rodonó (Kluwer, Dordrecht, 1989), p. 83.
6. E. R. Houdebine, B. H. Foing, and M. Rodonó, Astron. Astrophys. **238**, 249 (1990).
7. A. G. Gunn, J. G. Doyle, M. Mathioudakis, and S. Avgoloupis, Astron. Astrophys. **285**, 157 (1994).
8. A. G. Gunn, J. G. Doyle, M. Mathioudakis, *et al.*, Astron. Astrophys. **285**, 489 (1994).
9. V. V. Sobolev and V. P. Grinin, Astrofizika **38**, 33 (1995).
10. R. E. Gershberg and N. I. Shakhovskaya, Astron. Zh. **48**, 934 (1971) [Sov. Astron. **15**, 737 (1972)].
11. A. N. Kulapova and N. I. Shakhovskaya, Izv. Krym. Astrofiz. Obs. **48**, 31 (1973).
12. E. L. Eason, M. S. Giampapa, R. R. Radick, *et al.*, Astron. J. **104**, 1161 (1992).
13. P. B. Byrne, Sol. Phys. **121**, 61 (1989).
14. E. R. Houdebine, Ir. Astron. J. **20**, 213 (1992).
15. H. Abdul-Aziz, E. P. Abranin, I. Yu. Alekseev, *et al.*, Astron. Astrophys., Suppl. Ser. **114**, 509 (1995).
16. C. R. Vidal, J. Cooper, and E. W. Smith, Astrophys. J., Suppl. Ser. **25**, 37 (1973).
17. É. A. Baranovskiĭ, R. E. Gershberg, and D. N. Shakhovskoĭ, Astron. Zh. **78**, 78 (2001) [Astron. Rep. (in press)].

18. B. E. Woodgate, R. D. Robinson, K. G. Carpenter, *et al.*, Astrophys. J. Lett. **397**, L95 (1992).
19. M. E. Machado, E. H. Avrett, J. E. Vernazza, and R. W. Noyes, Astrophys. J. **242**, 336 (1980).
20. J. E. Vernazza, E. H. Avrett, and R. Loeser, Astrophys. J. **184**, 605 (1973).
21. J. E. Vernazza, E. H. Avrett, and R. Loeser, Astrophys. J., Suppl. Ser. **30**, 1 (1976).
22. J. E. Vernazza, E. H. Avrett, and R. Loeser, Astrophys. J., Suppl. Ser. **45**, 635 (1981).
23. C. Fang, J. C. Henoux, Hu Ju, *et al.*, Sol. Phys. **157**, 271 (1995).
24. N. D. Kostyuk and S. B. Pikel'ner, Astron. Zh. **51**, 1002 (1974) [Sov. Astron. **18**, 590 (1974)].
25. M. A. Livshits, O. G. Badalian, A. G. Kosovichev, and M. M. Katsova, Sol. Phys. **73**, 269 (1981).
26. M. M. Katsova, A. Y. Boiko, and M. A. Livshits, Astron. Astrophys. **321**, 549 (1997).
27. M. M. Katsova, S. L. Hawley, W. P. Abbett, and M. A. Livshits, Preprint No. 4 (1120), IZMIRAN (Institute of Terrestrial Magnetism, the Ionosphere, and Radio Wave Propagation, Russian Academy of Sciences, Moscow, 1999).
28. E. P. Abranin, I. Yu. Alekseev, S. Avgoloupis, *et al.*, Astron. Astrophys. Trans. **17**, 221 (1998).
29. W. P. Abbett and S. L. Hawley, Astrophys. J. **521**, 906 (1999).
30. W. E. Kunkel, Astrophys. J. **161**, 503 (1970).
31. M. M. Katsova, Astron. Zh. **67**, 1219 (1990) [Sov. Astron. **34**, 614 (1990)].
32. P. J. D. Mauas and A. Falchi, Astron. Astrophys. **310**, 245 (1996).
33. S. L. Hawley and B. P. Pettersen, Astrophys. J. **378**, 725 (1991).

Translated by K. Maslennikov

Astronomy Reports, Vol. 45, No. 4, 2001, pp. 319–320. Translated from Astronomicheskiĭ Zhurnal, Vol. 78, No. 4, 2001, pp. 370–372.

Asymptotic Distribution Functions for Electrons in an External Magnetic Field at Large Times

G. S. Bisnovatyĭ-Kogan and O. V. Shorokhov

Space Research Institute, Russian Academy of Sciences, ul. Profsoyuznaya 84/32, Moscow, 117810 Russia

Received April 14, 2000

Abstract—A formula describing the asymptotic electron distribution function as $t \longrightarrow \infty$ is obtained by selecting phase variables, taking into account the conservation of the longitudinal component of the electron velocity in a uniform, external magnetic field. Several initial distributions are considered. It is shown that there is no universal asymptotic distribution for an arbitrary initial isotropic distribution. © *2001 MAIK "Nauka/Interperiodica".*

1. INTRODUCTION

The magnetic bremsstrahlung origin of the radio emission of extragalactic sources has been verified by numerous observations [1]. For extended objects, where the magnetic field is large-scale and electron heating is not important, the electron momentum distribution becomes strongly anisotropic as the time approaches infinity. For a uniform magnetic field, the limiting distribution becomes one-dimensional with the momentum directed along the magnetic field, since the transverse momentum is completely dissipated via magnetic bremsstrahlung. Similar longitudinal distributions were studied in [2, 3], though for a very narrow class of electron functions. Here, we find a general expression for longitudinal distributions starting from arbitrary initial electron distribution functions, including the commonly used power-law distributions [1, 4].

2. DERIVATION OF A GENERAL EXPRESSION FOR THE ASYMPTOTIC FUNCTIONS

Let us consider electrons evolving in a uniform, external magnetic field taking into account radiation friction. Let $n(\mathbf{r})$ be the number of particles per unit volume. We assume that the spatial distribution is uniform with $\frac{\partial n}{\partial \mathbf{r}} = 0$, and take n in the form

$$n = \int N_p(\mathbf{p}, t) d^3 p, \tag{1}$$

where $N(\mathbf{p}, t)$ is the "density" in phase space. We introduce the spherical coordinates (p, θ, φ) in momentum space, with the z axis directed along the magnetic field $\mathbf{H}$:

$$n = \int N_p(p, \theta, \varphi, t) p^2 \sin\theta dp d\theta d\varphi. \tag{2}$$

The moving electron has an integral of motion: its velocity parallel to the magnetic field is conserved; i.e., $v_\parallel = \text{const}$ (see, for example, [5]). In this case, the electron momentum p asymptotically tends to $p_\infty = \frac{m v_\parallel}{\sqrt{1 - v_\parallel^2}}$ as $t \longrightarrow \infty$ tends to infinity. (Here and below we assume $c = 1$.) It is convenient to take $u(v_\parallel)$ as a variable, with u being an arbitrary function. Let us transform the coordinates from (p, θ, φ) to (p, u, φ), with the function $u(v_\parallel)$ taking the form [6]

$$u = \frac{v_\parallel}{\sqrt{1 - v_\parallel^2}}. \tag{3}$$

Then

$$n = \int N_p(p, u, \varphi, t) \frac{p\sqrt{p^2 + m^2}}{(1 + u^2)^{\frac{3}{2}}} dp du d\varphi, \tag{4}$$

where the integration domain is $\{0 < \varphi < 2\pi, |p| > m|u|, pu > 0\}$. Further, we consider axially symmetric distributions satisfying the condition

$$\frac{\partial N_p}{\partial \varphi} = 0. \tag{5}$$

Integrating over $d\varphi$ in (4), we obtain

$$n = 2\pi \int \frac{p\sqrt{p^2 + m^2}}{(1 + u^2)^{\frac{3}{2}}} N_p(p, u, t) dp du. \tag{6}$$

We introduce the function N_u

$$n = \int_{-\infty}^{+\infty} N_u du, \tag{7}$$

where, using (6),

$$N_u(u,t) = \frac{2\pi}{(1+u^2)^{\frac{3}{2}}} \times \int\limits_{\{pu>0,\,|p|>m|u|\}} N_p(p,u,t)\sqrt{p^2+m^2}\,pdp. \quad (8)$$

$\dot{N}_u = 0$, since $\dot{u} = 0$, so that we can substitute $N_p(p, u, t)$ for an arbitrary time in (8); in particular, for $t = 0$:

$$N_u = \frac{2\pi}{(1+u^2)^{\frac{3}{2}}} \times \int\limits_{\{pu>0,\,|p|>m|u|\}} N_p^0(p,u)\sqrt{p^2+m^2}\,pdp, \quad (9)$$

where $N_p^0(p, u)$ is the initial electron distribution. As $t \longrightarrow \infty$ $p \longrightarrow mu$, so that N_u is the asymptotic distribution as $t \longrightarrow \infty$. If the initial distribution is isotropic, we can write (9) in the form

$$N_u = \frac{2\pi}{(1+u^2)^{\frac{3}{2}}} \int\limits_{m|u|}^{\infty} N_p^0(p)\sqrt{p^2+m^2}\,pdp. \quad (10)$$

3. PARTICULAR CASES

Let us substitute several initial distributions into (10).

(A) For the initial distribution

$$N_p^0 = K\frac{(p^2+m^2)^{-\frac{\alpha+1}{2}}}{p}, \quad \alpha > 1,$$

which corresponds to the initial isotropic, power-law energy distribution $N_E = KE^{-\alpha}$, $n = 4\pi\int_m^\infty N_E(E)dE$ [4], we obtain

$$N_u = \frac{2\pi K}{\alpha-1}\frac{(mu)^{-(\alpha-1)}}{(1+u^2)^{\frac{3}{2}}}\,{}_2F_1\left(\frac{\alpha-1}{2}, \frac{\alpha}{2}, \frac{\alpha+1}{2}, -\frac{1}{u^2}\right). \quad (11)$$

When $|u| \gg 1$, this takes the form

$$N_u \approx \frac{2\pi K}{\alpha-1}\frac{(mu)^{-(\alpha-1)}}{(1+u^2)^{\frac{3}{2}}}. \quad (12)$$

(B) For the initial distribution

$$N_p^0 = \begin{cases} \frac{3}{4\pi}\frac{n}{p_m^3} & \text{for} \quad um < p_m \\ 0 \quad \text{for} \quad um > p_m \end{cases}$$

we obtain

$$N_u = \begin{cases} \frac{n}{2p_m^3}\frac{1}{(1+u^2)^{\frac{3}{2}}}\left\{(p_m^2+m^2)^{\frac{3}{2}} - (m^2(1+u^2))^{\frac{3}{2}}\right\} \\ \text{for} \quad um < p_m \\ 0 \quad \text{for} \quad um > p_m. \end{cases} \quad (13)$$

When $p_m \longrightarrow \infty$, this takes the form

$$N_u \longrightarrow \frac{n}{2}\frac{1}{(1+u^2)^{\frac{3}{2}}}. \quad (14)$$

(C) For the initial distribution

$$N_p^0 = \frac{n}{4\pi m^3}\frac{e^{-\frac{\sqrt{p^2+m^2}}{xT}}}{\left(\frac{xT}{m}\right)K_2\left(\frac{m}{xT}\right)}$$

we obtain

$$N_u = \frac{N}{2m}\frac{e^{-\frac{\sqrt{p^2+m^2}}{xT}}}{K_2\left(\frac{m}{xT}\right)}\frac{1}{\sqrt{1+u^2}} \times \left[1 + 2\frac{xT}{m}\frac{1}{\sqrt{1+u^2}} + 2\left(\frac{xT}{m}\right)^2\frac{1}{1+u^2}\right]. \quad (15)$$

As $x \longrightarrow \infty$, the distribution (C) tends to the same limit (14) as does distribution (B) when $p_m \longrightarrow \infty$, since the distributions (13) and (15) coincide when $x \longrightarrow \infty$ and $p_m \longrightarrow \infty$, tending to a limit with zero phase density. However, the conclusion drawn in [2] about the universality of this distribution for arbitrary initial isotropic, ultra-relativistic distributions is erroneous [see, for example, formula (12)].

REFERENCES

1. A. Pacholczyk, *Radio Astrophysics* (Freeman, San Francisco, 1970; Mir, Moscow, 1973).
2. E. V. Suvorov and Yu. V. Chugunov, Astrophys. Space Sci. **23**, 189 (1973).
3. V. V. Zheleznyakov, *Radiation in Astrophysical Plasma* [in Russian] (Yanus-K, Moscow, 1997).
4. N. S. Kardashev, Astron. Zh. **39**, 393 (1962) [Sov. Astron. **6**, 317 (1962)].
5. V. L. Ginzburg, *Theoretical Physics and Astrophysics (Additional Chapters)* [in Russian] (Nauka, Moscow, 1988).
6. G. S. Bisnovatyĭ-Kogan and O. V. Shorokhov, Astron. Zh. **77**, 703 (2000) [Astron. Rep. **44**, 624 (2000)].

Translated by V. Badin

Astronomy Reports, Vol. 45, No. 4, 2001, pp. 321–329. Translated from Astronomicheskiĭ Zhurnal, Vol. 78, No. 4, 2001, pp. 373–382.

Polarization of the Solar Corona in the Green Line: Contradiction Between Theory and Observations

O. G. Badalyan[1], I. L. Beigman[2], and M. A. Livshits[1]

[1]*Institute of Terrestrial Magnetism, Ionosphere, and Radio Propagation, Russian Academy of Sciences, Troitsk, Moscow oblast, 142190 Russia*

[2]*Lebedev Physical Institute, Russian Academy of Sciences, Leninskiĭ pr. 53, Moscow, 117924 Russia*

Received April 14, 2000

Abstract—The main results of polarization observations in the 530.3-nm line and their role in studying the physical conditions, structure, and magnetic field in the solar corona are discussed. A serious discrepancy between the observations and widely-accepted theoretical concepts was revealed: the theory predicts that the orientation of the polarization electric vector should be nearly radial, in contradiction with the observational results. In particular, the polarization vectors for both the green line and white-light corona in high-latitude streamers were tangential during the eclipse of July 11, 1991. The dependence of the degree of polarization on the angle between the radial direction and the magnetic-field vector was calculated without any *a priori* assumptions about the configuration of coronal fields. This theoretical analysis of the polarization-vector orientation for magnetic-dipole emission in the green line are in agreement with results obtained previously in other studies. Some ways to resolve the observed discrepancies are discussed. © *2001 MAIK "Nauka/Interperiodica".*

1. INTRODUCTION

Considerable progress in studying the loop structure of the inner corona has been achieved in recent years. First and foremost, this is associated with the operation of the *Yohkoh*, *SoHO*, and *TRACE* spacecraft [1–3]. The most important results in coronal investigations have been obtained from images in various allowed lines of ions at $T = 1–2 \times 10^6$ K (outside of flares), usually with very high spatial resolution, as well as ultraviolet and X-ray spectra above the limb. These have enabled detailed studies of the physical conditions inside particular loops and of the distributions of loops in various structures of the inner corona. In addition, satellite limb observations and studies of the conditions in the background corona (i.e., between and above loops and in coronal holes) were begun.

Observations of the solar corona in the green line have been made for over 60 years, both during eclipses and using Lyot coronographs. The temporal behavior of the intensity of this line in the inner corona at various phases of the solar cycle has been studied in detail (see, for example, [4]). The corresponding data contain information on structures associated with both local and large-scale magnetic fields in the corona, the evolution of these fields in the activity cycle, and their complex interaction.

Additional information about coronal magnetic fields can also be derived from polarization observations of emission lines. In principle, such data contain information on the influence of the magnetic field on the formation of scattered polarized emission in the lines. The development of techniques for measuring magnetic fields directly in the corona is very promising. Such attempts have been undertaken in the radio for the strong fields of active regions [5]. There is hope that studies of forbidden coronal lines will enable quite accurate measurements of not only strong but also weak magnetic fields.

The difficulty of polarization observations of the corona in emission lines is illustrated by the sparseness of reliable observational results. Observations in the 530.3-nm line conducted by J. Sýkora (Astronomical Institute of the Slovak Academy of Sciences) during the eclipse of July 11, 1991, near the solar-activity maximum, were analyzed in detail in [6]. Filtergrams of the entire corona were obtained using a narrow-band interference filter for four positions of a polaroid. In addition, polarization images of the white-light corona were obtained using the same instrumentation in the second half of the total eclipse. As distinct from all previous polarization investigations during eclipses, these data can be used to study the inner corona at all position angles in the green line and white light simultaneously [7–9]. Several new and interesting features were revealed in the behavior of the polarization characteristics of various structural objects, corresponding to different configurations of the coronal magnetic fields. These results supplement the extensive material obtained recently from observations by the *Yohkoh* and *SoHO* satellites.

We discuss here the results of polarization observations in the green line. A serious contradiction between the widely-accepted theory and the polarization obser-

1063-7729/01/4504-0321$21.00

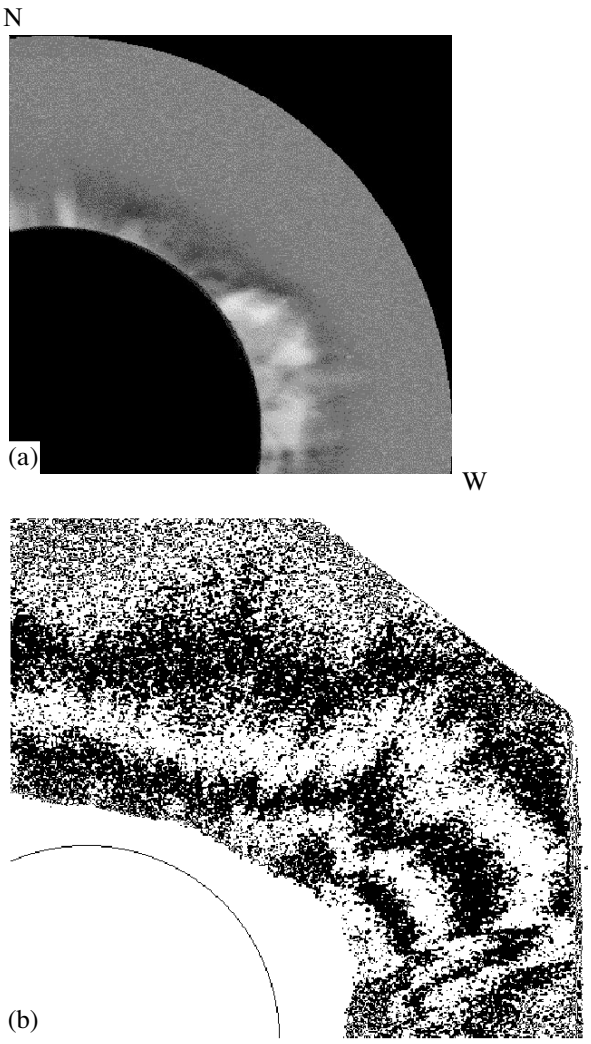

Fig. 1. The northwest region of the corona on July 11, 1991, (a) in the λ530.3-nm line and (b) in white light.

vations in this line was unexpectedly discovered. In this connection, the available observational data and some results are briefly reviewed. Next, we carry out a special theoretical analysis needed for the interpretation of the observations. The essence of the discrepancy is formulated, and several possible ways to remove it are considered. We also discuss the possibility of using line-polarization observations as diagnostics of the coronal plasma, including coronal magnetic fields, as well as of less dense regions outside centers of activity and large collections of loops.

2. MAIN RESULTS OF STUDYING POLARIZATION IN THE GREEN LINE

The most important feature of the corona on July 11, 1991 (i.e., at the phase of solar maximum) was that the dipole of the large-scale magnetic field was substantially tilted, so that its poles were near the equator. As a result, there were two systems of giant streamers near the north and south poles, making the shape of the white-light corona during this eclipse elongated, in contrast to the round corona usually observed in periods of maximum activity. Coronal condensations at latitudes ±20° were weak and spatially separated from the streamers.

The polarization characteristics of the coronal emission were derived from high-quality photographs in the 530.3-nm line obtained using a filter with a FWHM of 0.17 nm and a polaroid, on which the diameter of the solar image was 2 cm. Three sets of white-light photographs were also obtained with the same polaroid, but without the filter. After photometric measurements and careful computer superposition of the individual frames, we derived the polarization matrices for the white-light and green coronas for the corresponding polaroid positions, with a pixel size of 4.5″. We took into account the contribution of white light passing through the narrow-band filter by assuming that nearly all the emission over the northern polar hole corresponds to the white-light corona. We subtracted this contribution separately for each polaroid position. Computations showed that the degree of polarization in the green line changes only slightly after this subtraction of the white-light component. The data reduction and procedure for accounting for the white light is described in detail in [7, 8].

Figure 1a presents the northwestern part of the coronal image in the green line (the entire image can be found in [8]). This photograph shows a polar coronal hole and equatorial regions with their typical structure. A cluster of fine elements (primarily thin, straight rays over an arch-shaped structure) was observed in the white light at greater heights. Such structures are clearly visible in the white-light polarization distribution (Fig. 1b). A general correspondence between the coronal structures can be seen in Fig. 1. Note that such identification of structures in data on the white corona and green line requires high-quality photographs and superposition of the images to within one pixel.

Measurements of the degree of polarization p in the green line that can be used to study the behavior of p in coronal structures within some range of distance ρ from the disk center are quite limited. For example, Hyder *et al.* [10] found the degree of polarization to vary from 2 to 25% from the solar limb to $\rho = 1.5R_\odot$. It was also found that the degree of polarization increased with height, and p was appreciably higher in streamers than in coronal condensations. Later, Picat *et al.* [11] obtained larger values of p and confirmed the conclusions of [10]. Our results yield p values close to those in [11] (see Fig. 6 in [8]). Low degrees of polarization were obtained by Arnaud [12, 13] during observations out of eclipse.

Studies of the behavior of p at a fixed distance from the limb showed that the general tendency for p to decrease is preserved in the transition from weak to bright structures in the green line. At the same time, two

branches in the anti-correlation dependence in the p–$\log I_\lambda$ diagram can be identified (where I_λ is the green-line intensity at a given point in the corona). The upper branch corresponds to high-latitude streamers, while the lower branch corresponds to equatorial coronal condensations with various brightnesses. The two branches are most clearly defined at $\rho = 1.2R_\odot$, where a zone without points between the branches is clearly visible [14]. Each of the two branches is made up of several clumps of points (clusters) that correspond to isolated structures in the corona.

The character of the anti-correlation dependence can be seen in Fig. 2, which presents p and I_λ at $\rho = 1.25R_\odot$ for a ring with width $0.03R_\odot$. Compared to the corresponding figure for $\rho = 1.2R_\odot$ [15], the degrees of polarization increase and the intensities decrease, in agreement with the well-known dependence of these quantities on height. A decrease in the degree of polarization with increasing intensity can be traced. This means that the fraction of scattering in the line increases with distance from the disk center.

The anti-correlation dependence is primarily due to the fact that the role of electron collisions in exciting the green line increases in bright coronal structures. Excitation by electron collisions dominates in dense coronal condensations, which simultaneously increases the intensity and considerably decreases the degree of polarization. The high polarization of streamers points toward a leading role for photo-excitation, as opposed to electron collisional excitation. Therefore, the green-line polarization data testify that the contribution of scattering to the total emission in the line is substantial even at distances $\rho = 1.2R_\odot$ [8]; i.e., considerably lower than derived previously based on the "knee" in the height dependence of the line intensity.

We encountered some difficulties in our determination of the third characteristic of the green-line polarization—its direction—which will be discussed in the next section. Note that we define the direction of the polarization as the direction of preferential oscillations of the electric vector of the light wave propagating toward the observer.

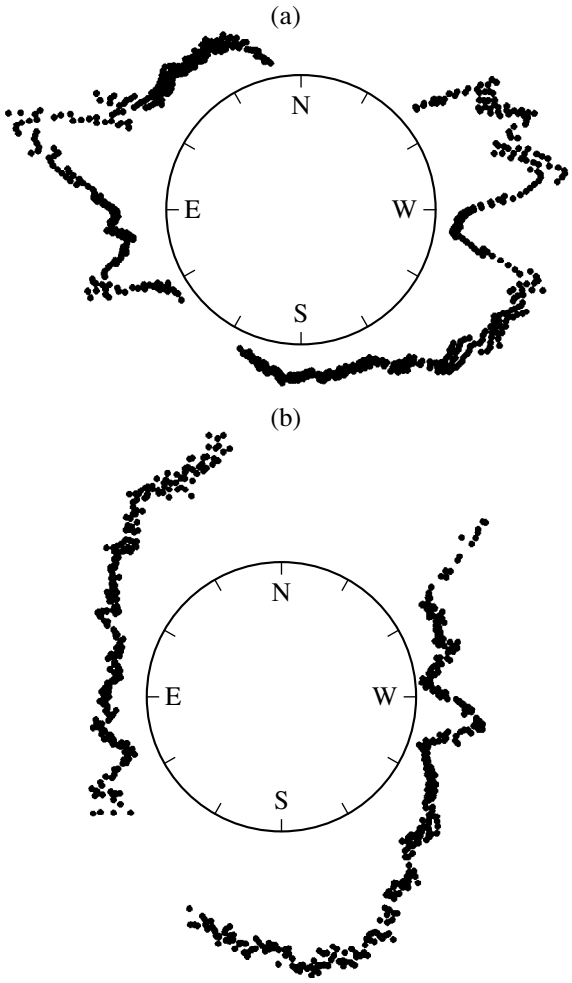

Fig. 2. Distribution of (a) intensity and (b) polarization in the green line a distance $1.25R_\odot$ from the disk center. The distance from the limb to a given point of the contour is proportional to the corresponding values of I_λ and p. The intensity is given in arbitrary units. The radius of the circle in (b) corresponds to 30% polarization.

3. DIRECTION OF POLARIZATION IN THE GREEN LINE

The polarization direction was already determined in our first work on the eclipse on July 11, 1991 (Fig. 5 in [7]). This question was studied in more detail in [16, 17]. The direction of the polarization in high-latitude streamers was almost tangential, with deviations from the tangential direction increasing in active low-latitude regions and reaching 40°–45° in some points of the corona. This result was surprising, since it is in contradiction with the widespread concept that the dominant direction of the polarization should be radial. This expectation was based primarily on theoretical calculations of the polarization characteristics of coronal lines assuming radial and dipolar magnetic fields (see [18] and references therein). It was also commonly believed that available observations were in agreement with this prediction of the theory.

Finding this discrepancy necessitated a new analysis of previously published results on the polarization direction. However, we will first make several preliminary remarks.

Unfortunately, there is some confusion in the definition of the "polarization direction" and the "plane of polarization" in the literature. This confusion originated in the 19th century, when two definitions were accepted: the plane of oscillations of the electric vector and the plane perpendicular to this (i.e., the direction of the magnetic vector). This confusion occurs not only in heliophysics, but also in other branches of science.

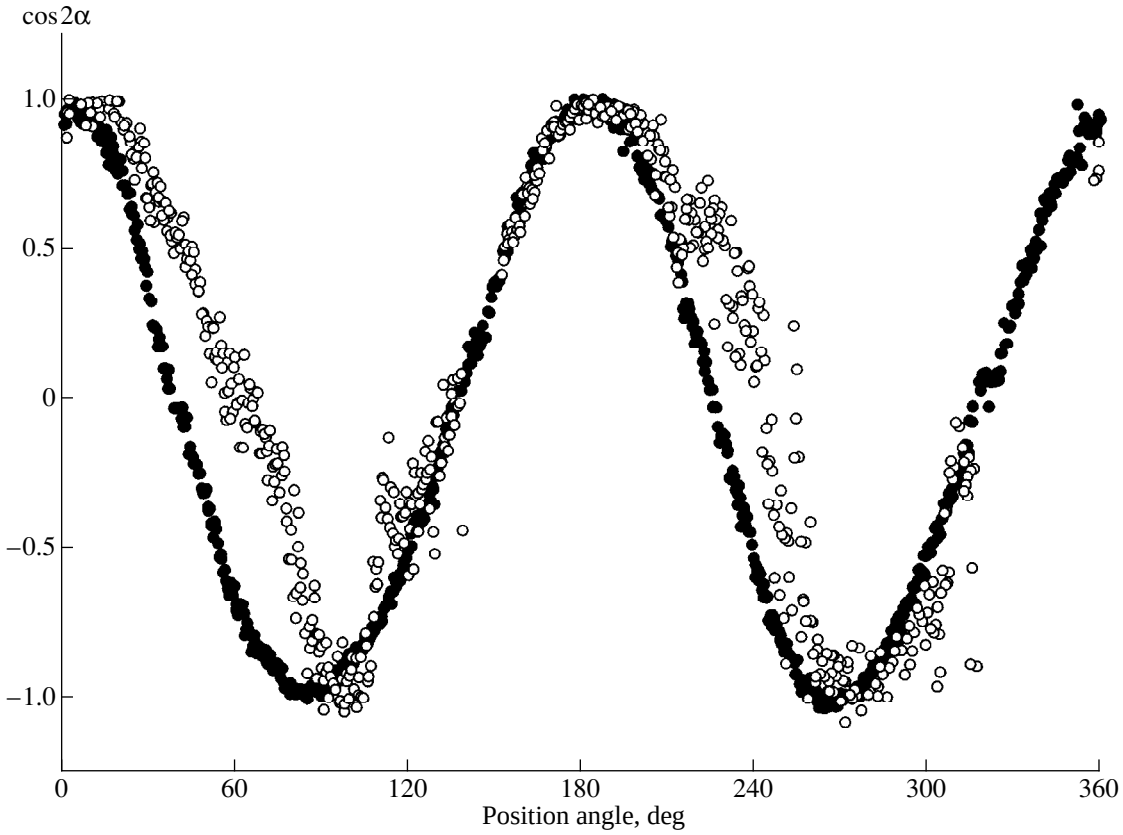

Fig. 3. Dependence of cos2α on the position angle for the white light (black circles) and the green line (white circles). Here, α is the angle between the direction of the first polaroid towards the north pole and the direction of the magnetic vector in the polarized emission.

In studies of the polarization of the white-light corona, the question of which vector (magnetic or electric) is considered usually doesn't arise. However, in fact, all relations for deriving polarization angles from observations give the direction of the magnetic vector [19–21]. This does not result in any confusion in the case of the white-light corona, since it is well known that the electric vector generated by Thomson scattering should be tangential. For example, in Fig. 1 from [22] on observations of the white-light corona, a radial direction is indicated, but it clearly refers to the magnetic vector. A tangential electric vector corresponds to the condition $K_t > K_r$, where K_t and K_r are the emission components with tangential and radial polarizations, respectively.

Let us consider the results of [10–12, 23] from this point of view. The well known paper [11] uses formulas that can be reduced to those in [19] (p. 96), and give the direction of the magnetic vector, as is traditional in other papers as well. However, Picat *et al.* [11] write that the angle calculated defines the direction of the electric vector. Therefore, despite the conclusions presented in [11], we believe that the radial direction in Fig. 4 in [11] reflects the magnetic vector, in agreement with the results of our analysis [7]. Note that the general techniques used to reduce the observational data and account for the contribution of white light in [11] and in our work were approximately the same.

Unfortunately, we cannot analyze the method of [10] in the same detail. Nevertheless, we note that the polarization direction in the "uncorrected 1965 green-line CELP observations" (see Fig. 9 in [10]) remains nearly constant when we intersect the solid line and go to higher regions, where the contribution of the white-light corona considerably increases and should affect the polarization direction, gradually making it tangential in the total (line plus continuum) emission.

There have been a number of measurements of the degrees of polarization in forbidden coronal lines out of eclipse [12, 13, 23]. Small values of p and nearly radial polarization were obtained for the green line. The transition from tangential to radial polarization is associated with a change in the sign of the second Stokes parameter Q. In filter observations with a Stokes polarimeter, this parameter for the line is calculated as $Q_\lambda = Q - Q_{wl}$, where Q refers to the total emission passing through the narrow-band filter in the line and continuum, whereas Q_λ and Q_{wl} refer to the line and continuum emission separately. We can see that the contribution of white light to the total emission must be taken into account carefully to determine the sign of Q_λ accurately. This requires accurate analysis of the filter pass-

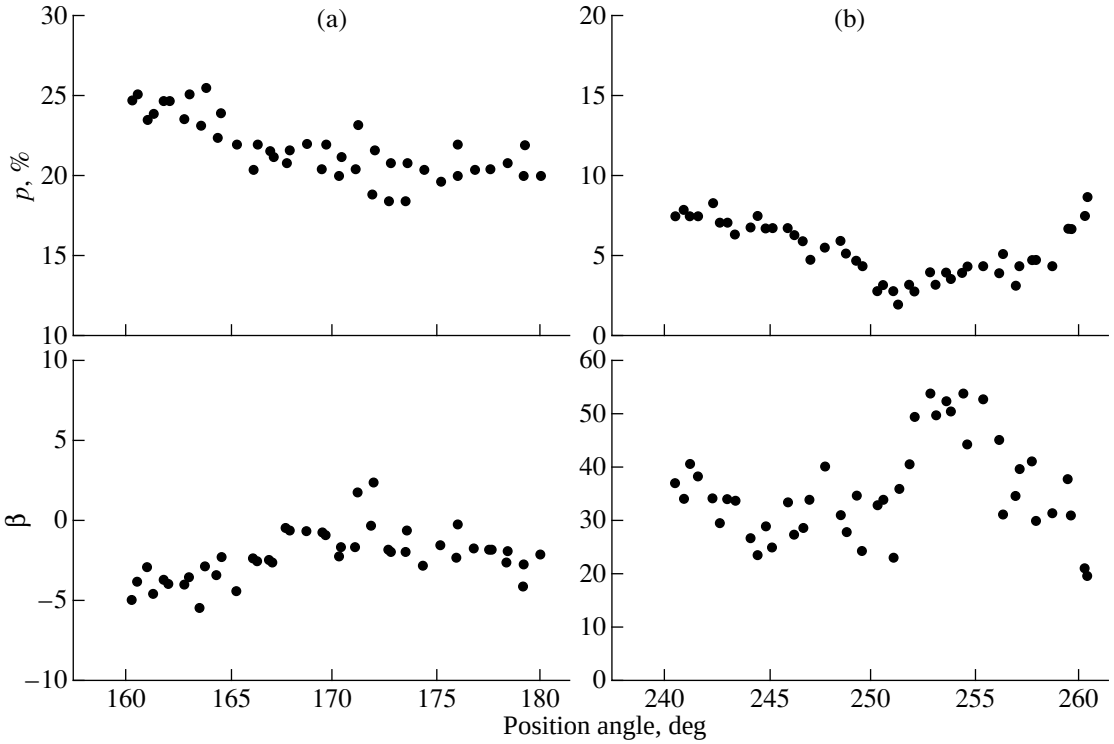

Fig. 4. Degree of polarization p and angle of deviation of the magnetic vector from the radial direction β in (a) the southern streamer and (b) in the coronal condensation at the west limb. A minus sign for β corresponds to a deviation toward the equator, and a plus sign to a deviation toward the nearest (in this case, south) pole.

band. Unfortunately, none of the papers cited above contains information on the total passbands of the filters (i.e., more than their half-widths). Therefore, we cannot draw any conclusions about the accuracy of the sign of Q_λ. Note also that observations conducted out of eclipse correspond to the brightest regions of the corona, where we expect substantial deviations of the polarization direction from that for pure scattering (see the discussion below).

The largest advantage of the observations used in our analysis for the eclipse of July 11, 1991 is that the images of the corona in the green line and white light were obtained using the same instrument. The degree and direction of the white-light polarization were measured reliably and are in agreement with well known results. These are illustrated in Fig. 3, which presents values of $\cos 2\alpha$ at $\rho = 1.2R_\odot$. Here, α is the angle between the direction of the magnetic vector and the N–S direction of the first polaroid (see, for example, p. 98 in [19]). In the case of the white-light corona, α is the position angle of a given coronal point.

Figure 3 also presents values of $\cos 2\alpha$ in the green coronal line calculated using the same formulas for the same coronal points after subtraction of the white-light contribution. There are no data for coronal holes near the north pole or for position angle ~150°, since there was no green-line emission there. We can see in Fig. 3 that the direction of the line polarization is similar to that for the white light. It is also evident that the difference between the directions of these polarizations substantially increases in bright equatorial regions. If, in accordance with theoretical predictions, the directions of the polarization in the line and white light were perpendicular (i.e., the difference in α was 90°), then the curve for the spectral line in Fig. 3 would be a mirror image of the white-light curve (i.e., the phase difference would be 180°). Since this effect is not evident, we conclude that these observations deviate considerably from the theoretical predictions.

Let us briefly discuss some other results that follow from the observations of the eclipse of July 11, 1991, which demonstrate that the polarization characteristics are very sensitive to large-scale structures and the configuration of the coronal magnetic fields. As noted above, clumps of points corresponding to individual streamers, coronal condensations, and, probably, the neighborhoods of two coronal holes can be identified in the p–$\log I_\lambda$ anti-correlation diagrams [14]. The same clustering can clearly be traced in all diagrams comparing the three polarization characteristics (intensity, degree, and direction of polarization), as well as the intensity of the magnetic field and its components [17]. Consequently, the observational data discussed here do, in fact, contain information about differences in physical conditions (in particular, about the magnetic field) in large-scale coronal structures.

As an example, Fig. 4 shows degrees of polarization and angles β, which describe the deviation of the elec-

tric vector from the tangential direction (or equivalently, the deviation of the magnetic vector from the radial direction), for the south-polar streamer at position angles 160°–180° and the coronal condensation at 240°–260°. The degrees of polarization in the streamer reach large values, and the angles β are small; i.e., the direction of polarization in the line is approximately the same as in the white-light corona. On the other hand, their behavior in the condensation is opposite: the degrees of polarization are small (due to the large fraction of unpolarized emission in these dense structures), whereas the deviation of the electric vector from the tangential direction increases appreciably. This increase is due to the complex influence of the magnetic fields on the formation of the polarized line emission. Note also that the scattering in β considerably increases in the equatorial region of the NW quadrant (see Fig. 1 in [15]), where a cluster of thin, straight rays was observed in the white light (Fig. 1b).

This, in fact, argues for the trustworthiness of our analysis of the polarization observations during the eclipse of July 11, 1991. First, we studied the polarization of the white-light corona and green line using a single set of observations. Thus, the polarization direction for the white-light corona was used to test the measurements, and the confusion described above was completely excluded. Second, our green-line polarization characteristics show quite reasonable dependences on type of coronal structure, position angle, and height.

Summarizing the above discussion, we concluded that, at the present time, there is no reliable observational evidence supporting the theoretical concept that the directions of the polarization in the white-light corona and green line should be perpendicular. Thus, we have observational data that cannot be excluded, but there is no adequate theory to describe them. Therefore, we can only try to make some reasonable assumptions about the theoretical degree of polarization for the line emission that is associated with the scattering of photospheric radiation p_{ph}.

4. POLARIZATION OF THE 530.3-NM LINE IN A MAGNETIC FIELD

A theory for the polarization of forbidden coronal lies was developed by Sahal-Breshaud [24] and House *et al.* [18] (see also references therein). They considered a statistical equilibrium of the level populations, taking into account their splitting in a magnetic field. These calculations (in particular, for the green line) were carried out for two idealized cases—radial and dipole magnetic fields [18]. Many factors associated with the coronal density distribution, an ion model with 23 sublevels, and solar limb darkening were simultaneously taken into account. This makes it difficult to identify dependences of the required parameters on some particular factor in the general model that affects the calculated characteristics of the line polarization. The assumption of idealized configurations for the magnetic field, which are in most cases considerably different from real ones, is a large problem in comparing the theoretical results with observations. This is especially true in the interpretation of observed polarization directions.

Because of the unexpected discrepancy between the observed and theoretical directions of polarization in the green line, we performed a new theoretical analysis to determine the basic regularities expected for the polarization characteristics of this emission. The most important feature of our approach is that we consider separately the influences of various factors, in particular, of the direction of the magnetic-field vector.

Let us neglect for the moment various depolarization factors and average over the line of sight. We shall consider the scattering of a photospheric photon by an Fe XIV ion located in the plane of the sky and assume that the coronal magnetic field lies at an arbitrary angle with respect to the radius vector specifying the motion of the photospheric photon.

The 530.3-nm line corresponds to the magnetic dipole transition $3p^2P_{1/2} - 3p^2P_{3/2}$ in the Fe XIV ion. The probability of the radiative transition is $A = 60\ \mathrm{s}^{-1}$. Obviously, the characteristic Zeeman splitting considerably exceeds the natural width of the line for magnetic fields typical of the solar corona ($\mu_0 B/\hbar \gg A$ even for a quite weak field $B > 3 \times 10^{-5}$ G, where $\hbar = h/2\pi$ is the Planck constant, μ_0 the Bohr magneton, and A the probability of a radiative transition). Thus, there is no interference between magnetic sublevels; consequently, the excitation and decay of each Zeeman sublevel can be studied independently.

Let us consider scattering of a light wave due to the 0–1 magnetic dipole transition of the ion in a magnetic field **B** (see Fig. 5). The probability of such scattering is determined by the matrix elements for the interaction between the magnetic fields of the incident and scattered waves, on the one hand, and the magnetic moment of the ion, on the other:

$$\mathfrak{W} = \sum_{m, m_0, m_1 \lambda, \lambda'} \left|\langle j_0 m_0 | \mathfrak{W}_\lambda | j m\rangle\right|^2 \times |\mathbf{b}_\lambda|^2 |\mathbf{b}'_{\lambda'}|^2 \left|\langle j_0 m_0 | \mathfrak{W}_{\lambda'} | j_1 m_1\rangle\right|^2 \quad (1)$$

and is proportional to the quantity

$$W = \sum_{m, m_0, m_1 \lambda, \lambda'} \begin{pmatrix} j_0 & 1 & j \\ m_0 & \lambda & -m \end{pmatrix}^2 \times |\mathbf{b}_\lambda|^2 |\mathbf{b}'_{\lambda'}|^2 \begin{pmatrix} j & 1 & j_1 \\ -m & \lambda' & m_1 \end{pmatrix}^2, \quad (2)$$

(we have used the standard representation of the matrix elements in terms of 3*j* Wigner symbols); where **b** and **b**' are vectors specifying the directions of the magnetic

fields in the exciting and scattered waves; j and m are the quantum numbers for the total angular moment and its projection for the initial, excited, and final states; and $\mathfrak{W}_\lambda$ is the magnetic moment operator.

W can be expressed in terms of the angles between the vectors **B**, **b** and **B**, **b**':

$$x = \cos^2(\mathbf{Bb}), \quad y = \cos^2(\mathbf{Bb}'),$$

where **b** and **b**' are the magnetic vectors of the incident and scattered waves, so that

$$W(x, y) = \frac{1}{16}xy - \frac{1}{48}x - \frac{1}{48}y + \frac{5}{144} = \frac{9xy - 3x - 3y + 5}{144}.$$

Finally, the degree of polarization can be written

$$p = \frac{I_\perp - I_\parallel}{I_\perp + I_\parallel} = \frac{W(x_1, y_1) + W(x_2, y_1) - W(x_1, y_2) - W(x_2, y_2)}{W(x_1, y_1) + W(x_2, y_1) + W(x_1, y_2) + W(x_2, y_2)}, \quad (3)$$

where $I_\perp$ and $I_\parallel$ are the intensities in the perpendicular and parallel directions with respect to the coronal magnetic field. The subscripts 1 and 2 refer to the two polarizations of the exciting and scattered wave, respectively, so that 1 corresponds to the polarization for which the wave magnetic field is parallel to the projection of B onto the plane of the sky; i.e., $p > 0$ implies that the electric vector for the dominant polarization should be perpendicular to the coronal magnetic field.

Now, let us make note of certain special cases.

(a) The magnetic field **B** is directed toward the observer: $y_1 = y_2 = 0$. There is no preferred direction in this case, and we obtain the identity $p = 0$.

(b) The magnetic field is directed along the solar radius: $x_1 = 0, x_2 = 0, y_1 = 1, y_2 = 0, p = -\frac{3}{7}$; i.e., the electric vector for the dominant polarization is radial.

(c) The magnetic field is perpendicular to the solar radius: $x_1 = 0, x_2 = 1, y_1 = 1, y_2 = 0, p = \frac{3}{17}$; i.e., the electric vector for the dominant polarization is again radial.

In general, if θ is the angle between **B** and the radius vector and δ is the angle between **B** and the plane of the sky, then the degree of polarization p is given by the formula

$$p = \frac{W(0, \nu) + W(u, \nu) - W(0, 0) - W(u, 0)}{W(0, \nu) + W(u, \nu) + W(0, 0) + W(u, 0)} = 3\nu\frac{-2 + 3u}{20 - 6\nu + 9u\nu - 6u}, \quad (4)$$

where $u = \cos^2\theta$ and $\nu = \cos^2\delta$.

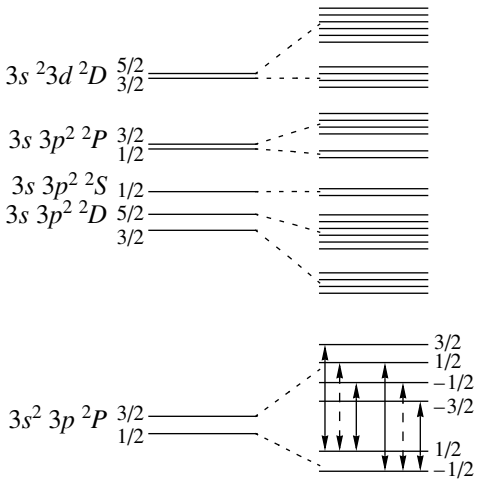

Fig. 5. Scheme of levels for the Fe XIV ion. The solid and dashed lines refer to the σ and π components, respectively.

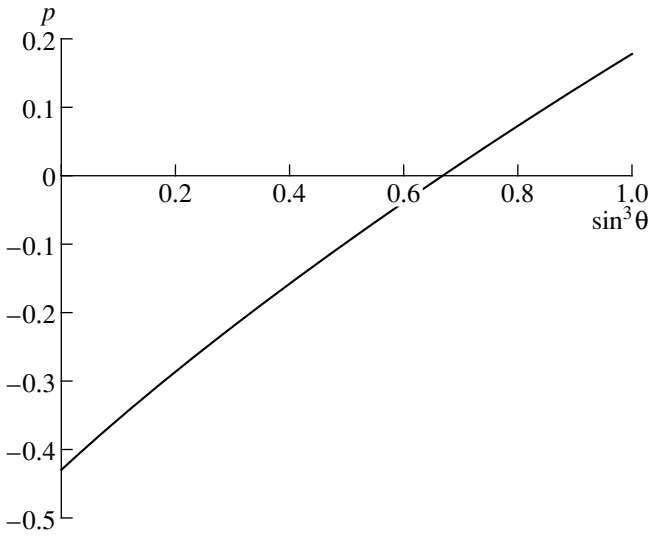

Fig. 6. Dependence of the degree of line polarization on the angle between a magnetic-field vector B in to the plane of sky and the radius. The coordinate system is associated with the magnetic field. The degree of polarization is positive if the electric vector of the scattered light is perpendicular to the magnetic field.

The dependence of p on θ when the magnetic-field vector is in the plane of the sky (i.e., $\delta = 0$) is given in Fig. 6. We can see that the maximum polarization for scattering in the plane of the sky can be as large as 43%, and p becomes zero at some angle (which is equal, as usual, to the Van Vleck angle).

Thus, the conclusion that the dominant direction of the electric vector of the scattered wave should be radial turns out to be associated with the magnetic-dipole character of the scattering in the forbidden line in the so-called strong-field approximation (see discussion above). Since $B = 1$ G is typical for the lower layers of the corona, this approximation is satisfied for the

green line, with a margin of 4–5 orders of magnitude. Most importantly, the largest theoretical polarizations are realized only in the case of radial coronal magnetic field, when the direction of the electric vector should be radial. On the other hand, under some conditions, small polarizations can be associated with appreciable deviations of the polarization direction from the radial direction.

Our analysis is in agreement with the results of House *et al.* [18] for their two idealized magnetic-field configurations. If we allow for some deviation of the coronal magnetic-field vector from the plane of the sky (i.e., $\delta \neq 0$) in our calculations, then, as follows from (4), the absolute value of p will decrease. This should also decrease the absolute value of p averaged over the line of sight. The main factors decreasing the observed polarization are likewise collisions with electrons and protons. These effects were studied in detail by Sahal-Breshaud [24], and turned out to be most important for dense structures; i.e., the coronal equatorial regions under consideration. The effects of depolarization and averaging over the line of sight become considerably smaller as the distance from the limb increases. However, it is not possible to obtain high polarizations in streamers and a rotation of the wave electric vector through 90°, so that the theory would be in agreement with the observations.

5. DISCUSSION

Our work with maps of the green-line polarization shows that the polarization characteristics are sensitive to the structure of the emitting regions, as well as the intensity and components of the magnetic field. There is no doubt that such maps contain information about the vector coronal magnetic field, and the problem of extracting this information is of paramount importance. Calculations of the magnetic fields in the outer atmosphere of the Sun based on photospheric measurements have been performed. It would be very desirable to confirm such calculations using direct observations, and to elucidate the nature of electric currents flowing in the corona and the characteristics of coronal MHD configurations.

The main contradiction revealed in our study is that the directions of the high polarizations observed in streamers are tangential, rather than radial, as predicted by the theory. The distribution of deviations of the electric-vector direction from tangential (or the magnetic-vector direction from radial) found in [16, 17] is almost the same as in [11]. We emphasize that our white-light images of the corona were obtained in the course of the same observations and processed using the same method, avoiding any confusion in the determination of the polarization angles.

The detection of scattered radiation at short distances from the limb leads to new possibilities for diagnostics of the background corona; i.e., the corona between loops and above loop systems. Of course, p_{ph} must be known to carry out such diagnostics, making it desirable to find an explanation for the revealed contradiction. Nevertheless, studies of streamers (especially, of differences associated with levels of activity in their lowest regions) can already be carried out using line-polarization data, even through this discrepancy is not yet understood.

From the theoretical point of view, one way to overcome these difficulties is to allow for the fact that, under the real conditions of the solar corona, the strongly forbidden transition $3p_{1/2} - 3p_{3/2}$ has an electric-dipole rather than a magnetic-dipole character. Since the probability of the allowed transition $3s^23p$–$3s3p^2$ is of the order of 10^{10} s^{-1}, an "admixture" to the ground state of a $3s3p^2$ state with an amplitude of the order of 10^{-4} is sufficient to make the electric-dipole transition dominant, so that the polarization pattern rotates through 90°. This partial removal of the forbidden nature of the transition is equivalent to increasing the probability of the radiative transition, resulting in an enhancement of the intensity of the scattered radiation and a simultaneous rotation of the polarization vector. Unfortunately, our preliminary estimates of the influence of plasma electric fields on the Fe XIV ion and interactions with the resonance radiation field associated with the $3s^23p - 3s3p^2$ (33.2 nm) transitions indicate that these mechanisms are not sufficiently efficient.

An alternative is based on excitation of the $3s3p^2$ configuration followed by radiative decay to the $3P_{3/2}$ level. Our preliminary estimates do not exclude this possibility.

We believe that the discrepancy we have detected could be resolved in the following two ways. There currently exist techniques for obtaining line-polarization observations over the entire corona. Such data will make it possible to confirm (or reject) the interesting observational results derived from the data for the eclipse of July 11, 1991. In addition, a heuristic approach to a theoretical analysis of the problem at hand could help clarify certain issues in spectroscopy and atomic physics.

ACKNOWLEDGMENTS

We are grateful to J. Sýkora and V.N. Obridko for their help during this study. This work was supported by the Russian Foundation for Basic Research (project codes 99-02-18346 and 00-02-17825).

REFERENCES

1. Y. Uchida, in *Physics of Solar and Stellar Coronae*, Ed. by J. F. Linsky and S. Serio (Kluwer, Dordrecht, 1993), p. 131.

2. *Proceedings of the 8th SoHO Workshop on Plasma Dynamics and Diagnostics in the Solar Transition Region and Corona*, ESA SP-446 (1999).
3. A. Title and the TRACE TEAM, in *Proceedings of the 11th Cambridge Workshop on Cool Stars, Stellar Systems and the Sun, Tenerife* (1999).
4. M. Storini and J. Sýkora, Sol. Phys. **176**, 717 (1997).
5. G. B. Gelfreikh, N. A. Pilyeva, and B. I. Ryabov, Sol. Phys. **170**, 253 (1997).
6. V. Rušin, L. Klocok, P. Zimmermann, *et al.*, Contrib. Astron. Obs. Skalnaté Pleso **22**, 117 (1992).
7. O. G. Badalyan and J. Sýkora, Astron. Astrophys. **319**, 664 (1997).
8. O. G. Badalyan, M. A. Livshits, and Yu. Sýkora, Astron. Zh. **74**, 767 (1997) [Astron. Rep. **41**, 682 (1997)].
9. O. G. Badalyan, M. A. Livshits, and J. Sýkora, Sol. Phys. **173**, 67 (1997).
10. C. L. Hyder, H. A. Mauter, and R. L. Shutt, Astrophys. J. **154**, 1039 (1968).
11. J. P. Picat, P. Felenbok, B. Fort, *et al.*, Astron. Astrophys. **75**, 176 (1979).
12. J. Arnaud, Rep. Obs. Lund **12**, 137 (1977).
13. J. Arnaud, Astron. Astrophys. **112**, 350 (1982).
14. O. G. Badalyan, M. A. Livshits, and J. Sýkora, Astron. Astrophys. **349**, 295 (1999).
15. O. G. Badalyan, M. A. Livshits, V. N. Obridko, and J. Sýkora, Izv. Ross. Akad. Nauk, Ser. Fiz. **63**, 2196 (1999).
16. O. G. Badalyan, V. N. Obridko, and J. Sýkora, in *Solar Polarization*, Ed. by K. N. Nagendra and J. O. Stenflo (Kluwer, Dordrecht, 1999), p. 373.
17. O. G. Badalyan, V. N. Obridko, and J. Sýkora, Astron. Zh. **76**, 869 (1999) [Astron. Rep. **43**, 767 (1999)].
18. L. L. House, C. W. Querfeld, and D. E. Rees, Astrophys. J. **255**, 753 (1982).
19. D. E. Billings, *A Guide to the Solar Corona* (Academic, New York, 1966).
20. K. Saito and J. Yamashita, Ann. Tokyo Astron. Obs. **7**, 163 (1962).
21. V. G. Fessenkoff, Astron. Zh. **12**, 309 (1935).
22. V. Kulidzhanishvili, A. Mayer, V. Mayer, and S. Danik, in *Solar Coronal Structures (IAU Colloquium 144)*, Ed. by V. Rušin, P. Heinzel, and J.-C. Vial (VEDA, Tatranska Lomnica, 1994), p. 529.
23. Ch. W. Querfeld, Rep. Obs. Lund **12**, 109 (1977).
24. S. Sahal-Breshaud, Astron. Astrophys. **36**, 355 (1974).

Translated by Yu. Dumin